

MOLECULAR DYNAMICS METHOD DEVELOPMENT AND SIMULATIONS OF
MOLECULE-POLYMER INTERACTIONS

By

TRAVIS W. KEMPER

A DISSERTATION PRESENTED TO THE GRADUATE SCHOOL
OF THE UNIVERSITY OF FLORIDA IN PARTIAL FULFILLMENT
OF THE REQUIREMENTS FOR THE DEGREE OF
DOCTOR OF PHILOSOPHY

UNIVERSITY OF FLORIDA

2011

© 2011 Travis W. Kemper

To my mother and father

ACKNOWLEDGMENTS

First, I would like to thank the Sinnott and Phillpot group members for their support and assistance. In particular Dr. Alex Chernatynskiy, Dr. Tao Liang and Dr. Bryce Divne provided invaluable guidance and intelligent criticism. Also, working with Eric Bucholz, Dr. Donghyun Kim and Dr. Ray Shan has been a great pleasure and working with Dr. Rakesh Behera was always entertaining. Also, Dr. Phillpot and his words of wisdom have been priceless. Lastly, I would like to especially thank Prof. Sinnott for her constant advice and encouragement has kept me on task and driven throughout my graduate career.

TABLE OF CONTENTS

	<u>page</u>
ACKNOWLEDGMENTS.....	4
LIST OF TABLES.....	7
LIST OF FIGURES.....	9
ABSTRACT	11
CHAPTER	
1 INTRODUCTION	13
2 METHODS.....	16
2.1 Molecular Dynamics.....	16
2.2 Classical Atomic-Scale Modeling of Materials	18
2.2 Empirical Potentials	18
2.3 Quantum Mechanical Modeling of Materials	28
2.1.1 Molecular Orbital Theory	29
2.1.1.1 Slater determinants.....	29
2.1.1.2 Basis sets.....	30
2.1.1.3 Self consistent field method	31
2.1.2 Density Functional Theory.....	33
2.1.2.1 Hohenberg-Kohn theorems.....	34
2.1.2.2 Kohn-Sham theorem.....	36
4.3 Post HF, Hybrid and Combinatorial Methods.....	37
2.4 Summary	38
3 POTENTIAL DEVELOPMENT	40
3.1 REBO Oxygen	40
3.1.1 Parameter Fitting Results.....	41
3.2 REBO Sulfur	42
3.2.1 Parameter Fitting.....	42
3.2.2 Validation and Testing.....	45
3.3 Summary	46
4 COMPARISON OF REBO AND DFT-MD DEPOSITION SIMULATIONS.....	62
4.1 CHF Deposition on Diamond	62
4.1.1 Methodology	62
4.1.2 Results	63
4.1.3 Discussion.....	65
4.2 Hydrocarbon Deposition on Polystyrene.....	67

4.2.1 Methodology	67
4.2.2 Results	68
4.2.3 Discussion	70
4.3 Summary	72
5 SURFACE POLYMERIZATION ION BEAM ASSISTED DEPOSITION	82
5.1 Methodology	85
5.2 Single trajectory deposition	86
5.2.1 Argon 100eV	87
5.2.2 Thiophene 100eV	88
5.2.3 50eV Depositions	90
5.2.4 Discussion	91
5.3 Ab-initio Reaction Calculations	92
5.3.1 Discussion	93
5.4 Summary	94
6 SURFACE MODIFICATION STUDIES	107
6.1 Amorphous Polymer Model	108
6.2 Methodology	112
6.3 Argon Deposition	113
6.3.1 Results	114
6.2.2 Discussion	118
6.2.3 Conclusions	119
6.3 Reactive Species	120
6.3.1 Results	121
6.3.1 Discussion	125
6.5 Summary	127
7 DEVELOPMENT OF <i>HfO₂</i> POTENTIALS	144
7.1 Density Functional Theory Data	145
7.2 Buckingham With Core Shell	145
7.3 Empirical Potential for HfO ₂	146
7.4 Structure and Phase order	146
7.4.1 Elastic Properties	147
7.5 Point Defect Energetics	148
7.6 Conclusions	151
8 CONCLUSIONS	156
REFERENCE LIST	159
BIOGRAPHICAL SKETCH	169

LIST OF TABLES

<u>Table</u>	<u>page</u>
3-1 <i>C-C</i> and <i>C-H</i> bond dissociation energies (D_O) and atomization energies (ΔH_a) in <i>eV</i>	48
3-2 <i>C-O</i> bond dissociation energies (D_O) and atomization energies (ΔH_a) in <i>eV</i>	49
3-3 <i>O-C</i> , <i>O-H</i> and <i>O-O</i> bond dissociation energies (D_O) and atomization energies (ΔH_a) in <i>eV</i>	50
3-4 Refit spline values for oxygen hydrocarbon interactions.....	50
3-5 Pair parameters	51
3-6 Angular parameters	51
3-7 Tricubic spline values for the coordination function P_{ij}	52
3-8 <i>C-C</i> bond dissociation energies (D_O) and atomization energies (ΔH_a) in <i>eV</i>	53
3-9 <i>C-H</i> bond dissociation energies (D_O) and atomization energies (ΔH_a) in <i>eV</i>	54
3-10 <i>C-S</i> bond dissociation energies (D_O) and atomization energies (ΔH_a) in <i>eV</i>	54
3-11 <i>C-S</i> bond dissociation energies (D_O) and atomization energies (ΔH_a) in <i>eV</i>	55
3-12 <i>C-S</i> , <i>S-H</i> and <i>S-S</i> bond dissociation energies (D_O) and atomization energies (ΔH_a) in <i>eV</i>	56
4-1 Reaction predicted by classical MD simulations using the REBO potential.....	73
4-2 DFT-MD predicted reactions.....	73
4-3 Reaction enthalpies calculated with the 22 atom carbon cluster	74
4-4 MD results of radicals deposited on PS.....	74
4-5 Hydrogen interaction with PS monomer	75
4-6 Reaction barriers for the interaction of C_2H^+ with the polystyrene monomer.	75
4-7 Reaction barriers for the interaction of CH_2 triplet radical with the polystyrene monomer C4 position.	75
4-8 Reaction barriers for the interaction of CH_2 singlet radical with the polystyrene monomer C4 position	75

6-1	Coordination analysis of <i>Ar</i> deposition on PE	128
6-2	Coordination analysis of <i>Ar</i> deposition on PP	128
6-3	Coordination analysis of <i>Ar</i> deposition on PS	129
6-4	Coordination analysis of atomic oxygen deposition on PE at 25eV	129
6-5	Coordination analysis of atomic oxygen deposition on PE at 50eV	130
6-6	Coordination analysis of atomic oxygen deposition on PE at 100eV	130
6-7	Coordination analysis of atomic oxygen deposition on PP at 25eV	131
6-8	Coordination analysis of atomic oxygen deposition on PP at 50eV	131
6-9	Coordination analysis of atomic oxygen deposition on PP at 100eV	132
6-10	Coordination analysis of atomic oxygen deposition on PS at 25eV	132
6-11	Coordination analysis of atomic oxygen deposition on PS at 50eV	133
6-12	Coordination analysis of atomic oxygen deposition on PS at 100eV	133
6-13	Comparison of probable modifications during argon and atomic oxygen bombardment at 100eV	134
7-1	Empirical potential parameters of the cubic and tetragonal phases of <i>HfO₂</i> , using the Buckingham formalism with shell model	152
7-2	Experimental and calculated lattice parameters of the monoclinic, tetragonal and cubic phases of <i>HfO₂</i>	152
7-3	Elastic constant tensor values for the tetragonal and cubic phases	153
7-4	Elastic moduli for the cubic and tetragonal phases of <i>HfO₂</i>	153
7-5	Defect formation energies from DFT and empirical potential calculations	154

LIST OF FIGURES

<u>Figure</u>	<u>page</u>
2-1 Periodic boundary conditions.....	39
3-1 Dissociation energies of oxygen dataset calculate with G3 plotted as function of values calculated with REBO.....	57
3-2 Bond stretching curves for <i>S -C</i> , <i>S -H</i> and <i>S - S</i> bonds.	58
3-3 Bond energy as a function of bond angle for fitted <i>Gθ</i> function	59
3-4 Dissociation energies of sulfur dataset calculate with G3 plotted as function of values calculated with REBO.....	60
3-5 Atomization energies of test set of molecules, energies boxed in red are included in fitting database	61
4-1 Systems used for reaction enthalpies: A) periodic slab of 128 atoms, B) carbon cluster of 22 atoms.	76
4-2 Site on diamond (111) surface.....	76
4-3 Transition state geometry of <i>CF2</i> radical on adamantane surface to produce <i>CF2</i> on the surface and an HF molecule.....	77
4-4 Crystalline polystyrene where the black and white atoms are thermostat region, and the blue and gray atoms are active.....	78
4-5 PS monomers where carbon is the darker (blue) atoms and hydrogen is the lighter (gray) atoms.....	78
4-6 Reaction profile of the interaction of H^+ with the polystyrene monomer.....	79
4-7 Reaction profile of the interaction of C_2H^+ with the polystyrene monomer. The barriers are presented in Table 4-6	80
4-8 Reaction pathways for CH_2 triplet radical on C4 the barriers are presented in Table 4-7.	81
4-9 Reaction pathway of <i>CH2</i> singlet radical on C4, the barriers are presented in Table 4-8.	81
5-1 Photoluminescence spectra of 3T and SPIAD films produced with Ar^+ and Thiophene (T^+) at $100eV$ and $200eV$ ³³	96
5-2 Mass spectra data ³³	97

5-3	Terthiophene unit cell ¹³⁵	98
5-4	Perpendicular and parallel configurations of the 3T films on a hydrogen terminated substrate.....	99
5-5	Yield at 100eV thiophene and Ar on the surface with 3T in the parallel configuration.....	100
5-6	Two step process of the removal of a single atom from one 3T (1) and donating it to the set of 3T molecules below it (2).....	101
5-7	Yield at 100eV thiophene and Ar on the surface with 3T in the perpendicular configuration.....	102
5-8	Molecular analysis of films resulting from 50eV argon and thiophene deposition on 3T in the parallel configuration	103
5-9	Molecular analysis of films resulting from 50eV argon and thiophene deposition on 3T in the perpendicular configuration	104
5-10	Reaction pathway of radical C ₂ H and C ₂ H ₂ interacting with a thiophene molecule with calculated transition state energies.....	105
5-11	C ₁₂ H ₉ S ₃ produced by 50eV thiophene on parallel 3T	106
6-1	Initial PE, PP, PMMA and PS substrates with each chain color coded.....	135
6-2	Pair distribution function for PE, PP and PS.....	136
6-3	Yield of sputtered carbon and hydrogen atoms for Ar at 25eV, 50eV and 100eV	137
6-4	Molecular mass analysis for Ar deposited at 50eV.....	138
6-5	Molecular mass analysis for Ar deposited at 100eV.....	139
6-6	Yields and concentrations of the three most probable groups formed during 100eV Ar deposition on PE, PP and PS.....	140
6-7	Yield of sputtered carbon and hydrogen for atomic oxygen at 25eV, 50eV and 100eV.	141
6-8	Molecular mass analysis of 50eV atomic oxygen.....	142
6-9	Oxygen bonding in PS for deposition energies at 25eV with C-(O)-C coordination in four possible environments	143
7-1	Three low pressure phases of HfO ₂ (a) monoclinic, (b) tetragonal, (c) cubic where oxygen is darkly shaded and hafnium is lightly shaded	155

Abstract of Dissertation Presented to the Graduate School
of the University of Florida in Partial Fulfillment of the
Requirements for the Degree of Doctor of Philosophy

MOLECULAR DYNAMICS METHOD DEVELOPMENT AND SIMULATIONS OF
MOLECULE-POLYMER INTERACTIONS

By

Travis W. Kemper

December 2011

Chair: Susan Sinnott
Major: Materials Science and Engineering

Modifying the surface of a material can alter its chemical resistance, frictional properties, biocompatibility, adhesive properties and electrical properties, while maintaining the bulk properties. Treatments utilizing ion beams and plasmas can be employed for a range of modifications from the creation of protective coatings on plastics to the production of complex electronics.

However, the complex interactions between gas molecules and surfaces are still not well understood. In order to investigate these interactions atomic scale molecular dynamics simulations using the second generation reactive empirical bond order (REBO) potential are conducted. First the second generation REBO potential is modified to improve the previously published oxygen hydrocarbon interactions. Further modification is done to add sulfur interactions with hydrocarbons. Studies of hyperthermal species interacting with surfaces relevant to polymer modification are conducted.

The performance of the REBO potential is evaluated by comparing deposition results involving CF_3 on diamond, and H , C_2H and CH_2 on polystyrene to results

obtained with quantum chemical methods. While the second generation REBO potential reproduced reaction enthalpies within reasonable limits, the main deficiency is found to be the short range nature of the potential and the lack of different charge states. However, the computational efficiency allows for a greater sampling of possible reactions, and there for is a good initial evaluation tool to allow for further analysis with more accurate quantum based methods.

Next the surface polymerization by ion assisted deposition (SPIAD) process is investigated. The SPIAD process involves the deposition of thermal neutrals and hyperthermal ions to produce oligomer films for use in organic molecule based electronics. In order to study this process thiophene molecules are deposited on thin films of terthiophene. During these simulations the differences in argon and thiophene depositions are examined.

In order to investigate the effects of reactivity of the deposited species, argon and atomic oxygen are deposited a set of prototypical polymers. These prototypical polymers, polyethylene, polypropylene and polystyrene, are generated using an amorphous polymer model. Statistical data on probable changes in substrate bonding is presented.

Thus, atomic-scale simulations are conducted to advance the plasma and ion-beam treatments of polymer surfaces. Probable modifications are identified using the second generation REBO potential. Sulfur and improved oxygen parameters are developed under the second generation REBO potential formalism. Probable modifications are further analyzed using quantum chemical analysis. To identify the mechanism in which ions modify polymer surfaces.

CHAPTER 1 INTRODUCTION

Numerous processing methods involve the modification of solid surfaces via exposure to energetic particles. These energetic particles can be photons, electrons, atoms, radicals, or ions produced by a variety of techniques. For example, lasers are used to melt surfaces for structural, tribological and corrosion resistance purposes¹. Chemical vapor deposition (CVD) is used to grow materials for a myriad of applications from diamond for electronics to silicon carbide for cutting tools². Ion beams can introduce small amounts of dopants to a solid surface thereby altering the mechanical, electrical, optical, magnetic or superconducting properties of the material³. Non-thermal plasmas have been used extensively in the semiconductor industry, primarily for etching photoresists⁴.

Plasmas⁵ and ion-beam⁶ treatments have been found to effectively modify polymer surfaces for barrier coatings⁷, improving adhesion^{5, 8-11}, functionalization^{12, 13}, sterilization¹⁴ and biocompatibility¹⁵. Plasmas and ion beams can modify surfaces without the need for solvents or catalysts, which are not only harmful to the environment¹⁶⁻¹⁸, but can also have negative effects for some applications due to the presence of residual chemicals¹⁹.

Low temperature, non-thermal plasmas are typically used for materials processing²⁰. Unlike plasmas used in fusion reactors, plasmas used for surface modification purposes are not in thermodynamic equilibrium, which allows them to exist at or near room temperature. These non-thermal low temperature plasmas can be generated in low pressure reactors or in air with an electric field. Direct current (DC) discharges or radio frequency (RF) discharges can be applied to a parallel plate

capacitor to generate the electric field necessary to accelerate electrons into the neutral gas species^{4, 20, 21}. The collision between free electrons and neutral gas species results in the ionization or excitation of the neutral gas species¹¹. This process and subsequent processes, such as the emission of photons due to excitation, creates the electrons, ions, photons and neutrals which comprise the complex system of the non-thermal plasma.

Low temperature plasmas have been widely used for etching²². A range of feeder gases have been used including fluorocarbons, *Ar*, *O₂*, *CO₂* and air. Fluorocarbon (FC) plasma treatments can not only be used for etching²³, but also to increase hydrophobicity²⁴ or dielectric constant^{25, 26}, and to create barrier coatings on polymer surfaces²⁷. Coatings of diamond like carbon (DLC) can also be grown from FC plasmas at lower temperature than hydrocarbon precursors²⁸. Oxygen containing plasmas and ion beams²⁹ can be used for numerous surface modifications, including etching²².

One method that combines plasma and ion-beam treatments to produce stable conducting organic films is surface polymerization by ion assisted deposition (SPIAD)³⁰⁻³³. This method employs the co-deposition of thermal α -terthiophene and hyperthermal thiophene cations to induce polymerization at the gas-solid interface³⁰. The production of conjugated higher molecular weight species during the polymerization process is beneficial for photovoltaic devices³⁰. In particular, the increase in the electron conjugation length produces a red shift in the UV/vis absorption spectra³¹, which allows for absorption of visible light at longer wavelengths.

One of the primary events of interest in plasma treatments is the collision of the accelerated ion with the substrate. Hyperthermal ions (1-500eV) have been found to be of particular interest for film growth^{34, 35}. However, the complex processes involved in the gas-surface interactions are still not well understood for the polymer systems. Molecular dynamics (MD) simulations offer a unique opportunity to study these complex interactions. Atomistic MD simulations using reactive empirical potentials can capture events at the ps to ns time scale³⁶.

In particular, these simulations offer a way to model multifaceted chemical reactions due to a single species, while precisely monitoring atomic and molecular compositions. In this work the second generation reactive empirical bond (REBO) potential primarily used, due to its ability to capture bond dissociation and formation by dynamically evaluating the bonding of atomic pairs depending on the immediate environment^{37, 38}. The second generation REBO potential for hydrocarbons has been successfully applied to the study of the mechanical properties of graphene³⁹, tribology⁴⁰,⁴¹ and ion-beam modification of polymers⁴²⁻⁴⁶.

CHAPTER 2 METHODS

The primary motivation of this work is to decouple the effects of relevant ions at various energies interacting with a surface during ion beam and plasma treatments. Experimentally, decoupling different factors occurring during treatment is difficult as films are primarily characterized post treatment⁴⁷. Computer simulations offer complete control over environmental conditions, and the ability to limit the interaction of the surface to a single type of particle. The primary focus of this work is the use of molecular dynamics (MD) simulations to evaluate dynamical processes related to the modification of polymer and oligomer surfaces by energetic atomic and polyatomic species.

2.1 Molecular Dynamics

MD describes the evolution of a “material system” with atomic scale resolution. Considering the nuclei of the atoms are at least 2000 times heavier than the electrons orbiting them; therefore, the Born-Oppenheimer approximation is usually employed. This allows the electrons to be considered to have instantly relaxed to their ground state, in the constant external field created by the nuclei, and to produce quantum-mechanical forces that act on the latter. Motion of the nuclei is, in turn, controlled by classical Newtonian physics.

Newtonian equations of motion are differential equations that describe the evolution of atomic trajectories over time. The methods used here to solve the resulting system of differential equations are known as integrators. Various forms with a range of complexity and accuracy exist⁴⁸. In this work the Gear third order predictor corrector is

primarily used^{49, 50}. To find the position of the atom at time $t + \Delta t$ a Taylor expansion out to the third order about t is used:

$$\begin{aligned}
 \mathbf{r}^p(t + \Delta t) &= \mathbf{r}(t) + \Delta t \mathbf{v}(t) + \frac{1}{2} \Delta t^2 \mathbf{a}(t) + \frac{1}{3!} \Delta t^3 \mathbf{b}(t) + \dots \\
 \mathbf{v}^p(t + \Delta t) &= \mathbf{v}(t) + \Delta t \mathbf{a}(t) + \frac{1}{2} \Delta t^2 \mathbf{b}(t) + \dots \\
 \mathbf{a}^p(t + \Delta t) &= \mathbf{a}(t) + \Delta t \mathbf{b}(t) + \dots \\
 \mathbf{b}^p(t + \Delta t) &= \mathbf{b}(t).
 \end{aligned}
 \tag{2-1}$$

At the predicted position the forces are calculated at time $(t + \Delta t)$, giving the correct acceleration $\mathbf{a}^c(t + \Delta t)$ for an atom at position $\mathbf{r}^p(t + \Delta t)$. The error in the prediction step is then be estimated by:

$$\Delta \mathbf{a}(t + \Delta t) = \mathbf{a}^c(t + \Delta t) - \mathbf{a}^p(t + \Delta t).
 \tag{2-2}$$

The estimated error can then be used to correct the predicted values:

$$\begin{aligned}
 \mathbf{r}^c(t + \Delta t) &= \mathbf{r}^p(t + \Delta t) + c_0 \Delta \mathbf{a}(t + \Delta t) \\
 \mathbf{v}^c(t + \Delta t) &= \mathbf{v}^p(t + \Delta t) + c_1 \Delta \mathbf{a}(t + \Delta t) \\
 \mathbf{a}^c(t + \Delta t) &= \mathbf{a}^p(t + \Delta t) + c_2 \Delta \mathbf{a}(t + \Delta t) \\
 \mathbf{b}^c(t + \Delta t) &= \mathbf{b}^p(t + \Delta t) + c_3 \Delta \mathbf{a}(t + \Delta t).
 \end{aligned}
 \tag{2-3}$$

The coefficients c_0 , c_1 , c_2 and c_3 are $1/6$, $5/6$, 1 and $1/3$, respectively. The value of Δt is known as the time step, and has to be on the order of the thermal vibrations of the system.

Due to computational limitations, most atomic simulation cells are on the order of nanometers in size. This is rarely representative of a real system; therefore, periodic boundary conditions are used to artificially extend the simulation cell to make the simulation more realistic, as shown in Figure 2-1. Periodic boundary conditions can be conceptualized as replicating the simulation cell in an infinite period lattice. The results

are that for each particle moving along a trajectory in the simulation cell, an image particle is moving along the same trajectory in each infinite reproduction. Therefore, if a particle exits through one boundary of the simulation cell an image will enter through another creating an artificially infinite medium.

In order to control temperature the velocity of the particles is manipulated through the use of thermostats. In this work the Langevin method is used⁵¹. The force on an atom under thermostat conditions is then governed by the Langevin equation:

$$ma = F - \beta v + F'. \quad (2-4)$$

Here, F is the force felt by the atom, v is the velocity of the atom, β is friction constant and F' is a stochastic force chosen in a way to satisfy dissipation-fluctuation theorem⁵². The friction constant is determined based on the Debye temperature of the system, and the stochastic force is dependent on β , the temperature and the time step.

2.2 Classical Atomic-Scale Modeling of Materials

In order to conduct an MD simulation a description of the inter-atomic forces is required. The formulation of the physics that governs particles at nanometer scales is quantum mechanics. Unfortunately, solving Schrödinger's equation with most approximations is too computationally expensive, or time consuming with regards to CPU time, to evaluate the interaction between atoms in dynamical systems on the ps to ns time regimes. Therefore, empirical potentials are often employed to describe the interactions between particles in a more efficient manner.

2.2 Empirical Potentials

Empirical potentials are functions used to represent the quantum mechanical potential energy between particles. This negates the need to solve for the electron wave-functions of the system, greatly increasing computational efficiency. For a system

of N_{atoms} the potential energy can be divided into terms that are dependent on the number of atoms participating in an interaction,

$$E = \sum_i V_i(\mathbf{r}_i) + \sum_i \sum_{j>i} V_{ij}(\mathbf{r}_i, \mathbf{r}_j) + \sum_i \sum_{j>i} \sum_{k>j>i} V_{ijk}(\mathbf{r}_i, \mathbf{r}_j, \mathbf{r}_k) \dots \quad (2-5)$$

The first term V_i can be considered as the potential energy due to an external field; while, the subsequent terms are interatomic potential energy functions. The 2-body term V_{ij} is of primary importance for describing a system of atoms; in that, it can describe attraction and repulsion. One of the simplest 2-body, or pair, potentials is the Lennard-Jones (LJ) potential⁴⁸, which is often used to describe van der Waals forces acting between atoms or molecules,

$$V_{ij}^{LJ} = 4\varepsilon_{ij} \left[\left(\frac{\sigma_{ij}}{r_{ij}} \right)^{12} - \left(\frac{\sigma_{ij}}{r_{ij}} \right)^6 \right] \quad (2-6)$$

This has met with wide success in the simulation of noble gas interactions where dispersion forces dominate, in particular liquid argon⁵³. This pair potential is dependent on the interatomic distance $r_{ij} = |\mathbf{r}_i - \mathbf{r}_j|$. The parameters ε_{ij} and σ_{ij} are dependent on the element type of atoms i and j , and are fit to a dataset of experimental or quantum mechanical data. Furthermore, the LJ potential is divided into two parts: repulsion r^{-12} and attraction r^{-6} . The attraction term represents the decrease in potential energy two atoms experience when coming into bonding proximity of one another. Conversely, the repulsion term captures the increase in potential energy the two atoms impose on each other if too much electron cloud overlap occurs. The summation of these terms describes the interatomic potential well between atoms i and j . The features of this well

contain information essential to describing the system such as, bond length, bond energy and thermal expansion.

In order to capture the ionic bonding in ceramics, particularly oxides, the Buckingham potential has been widely implemented⁵⁴,

$$V_{ij} = A_{ij}e^{(-r_{ij}/\rho_{ij})} - \frac{C_{ij}}{r_{ij}^6} + \frac{1}{4\pi\epsilon_0} \frac{q_i q_j}{r_{ij}}. \quad (2-7)$$

This pair potential can be seen as a modification of the LJ potential; in that, the r^{-12} term is replaced by an exponential term. The last term is the Coulombic term to take into account the fixed charge of each particle q_i and q_j .

Furthermore, a shell model can be used to capture atomic polarizability by considering the atom to be composed of a core and shell, with different charges summing to the total charge of the atom. The core and shell are considered to be connected by a spring with a spring constant k_α and displaced from equilibrium by a distance d :

$$V_{spring}(d) = \frac{1}{2} k_\alpha d^2. \quad (2-8)$$

Covalent bonding presents a particular problem in that it has varying bond orders depending on the local environment. To address this, Tersoff⁵⁵ proposed the use of a bond order term to augment a set of repulsive and attractive terms, based on the work of Abell⁵⁶:

$$V_{ij} = f_c(r_{ij})[V^R(r_{ij}) + b_{ij}V^A(r_{ij})]. \quad (2-9)$$

Here the repulsive term is:

$$V^R(r_{ij}) = Ae^{(-\alpha r_{ij})} \quad (2-10)$$

and the attractive term is:

$$V^A(r_{ij}) = Be^{(-\beta r_{ij})}. \quad (2-11)$$

The cutoff function:

$$f_C(r_{ij}) = \begin{cases} 1 & r_{ij} < R^{min} \\ \frac{1}{2} \left[1 + \sin \left(\frac{\pi (2r_{ij} - (R^{min} + R^{max}))}{R^{max} - R^{min}} \right) \right] & R^{min} < r_{ij} < R^{max}, \\ 0 & r_{ij} > R^{max} \end{cases} \quad (2-12)$$

smoothly reduces the potential to zero between R^{min} and R^{max} . The bond order term:

$$b_{ij} = \left[1 + B^n \sum_{k \neq i,j} f_C(r_{ik}) g(\theta_{kij}) e^{[\lambda^3 (r_{ij} - r_{ik})^3]} \right]^{-1/2n}, \quad (2-13)$$

contains all the multibody components. The angular function is:

$$g(\theta) = 1 + \frac{c^2}{d^2} - \frac{c^2}{[d^2 + (h - \cos\theta)^2]}. \quad (2-14)$$

Tersoff successfully parameterized this potential to model the covalent nature of silicon and diamond^{55, 57}.

This concept of augmenting the pair terms of a potential with a bond order term has spawned a series of empirical potentials that includes the reactive empirical bond order (REBO) potential for hydrocarbons³⁷. The major modifications made to the Tersoff potential within REBO potential formalism are the additions of coordination and conjugation terms to the bond order term. The details of the first generation REBO potential will not be presented; instead we will skip to the second generation REBO³⁸ potential, which is a major focus of this work. However, it should be mentioned that the

first generation of REBO potential was successfully applied to CVD growth of diamond³⁷, frictional properties of diamond surfaces⁵⁸, and the mechanical properties of fullerenes⁵⁹.

In the second generation REBO formalism, the pair potential shown in Equation (2-9) remains unchanged. The attractive and repulsive terms V^R and V^A are slightly modified to:

$$V^R(r_{ij}) = \left(1 - \frac{Q}{r}\right) A e^{(-\alpha r_{ij})} \quad (2-15)$$

and

$$V^A(r_{ij}) = \sum_{n=1,3} B_n e^{(-\beta_n r_{ij})}. \quad (2-16)$$

The cutoff function is modified to:

$$f_C(r_{ij}) = \begin{cases} 1 & r_{ij} < R^{min} \\ \frac{1}{2} \left[1 + \cos\left(\frac{r_{ij} - R^{min}}{R^{max} - R^{min}}\right) \right] & R^{min} < r_{ij} < R^{max}. \\ 0 & r_{ij} > R^{max} \end{cases} \quad (2-17)$$

As mentioned previously, the first generation REBO potential added terms to capture the coordination and the conjugation. The second generation REBO potential kept these modifications and added torsion. The second generation REBO bond order term has the form:

$$b_{ij} = \frac{1}{2} [b_{ij}^{\sigma-\pi} + b_{ji}^{\sigma-\pi}] + b_{ij}^{DH} + \Pi^{RC}. \quad (2-18)$$

Where $b_{ij}^{\sigma-\pi}$ captures angular and coordination dependence:

$$b_{ij}^{\sigma-\pi} = \left[1 + \sum_{k \neq i,j} f_C(r_{ik}) G(\theta_{kij}) e^{\left[\lambda_{jik} \left[(r_{ij} - R_{ij}^{\epsilon}) - (r_{ik} - R_{ik}^{\epsilon}) \right] \right]} + P_{ij}(N_i^C, N_i^H) \right]^{-1/2}. \quad (2-19)$$

Here the coordination function P_{ij} is a bicubic spline dependent on the number of carbon and hydrogen neighbors as defined as:

$$N_i^{elm} = \sum_{k \neq i,j} f_C(r_{ik}). \quad (2-20)$$

The angular term for carbon is a sixth order polynomial,

$$G_{ij}(\theta) = \sum_{n=1,7} a_n \cos^{n-1} \theta. \quad (2-21)$$

Separate sets of coefficients are fit for each region: $0 < 109.47^\circ$, $109.47^\circ < 120^\circ$ and $120^\circ < 180^\circ$. For the region $0 < 109.47^\circ$, under and over coordinated structures are captured by the revised angular function:

$$g_C = G_C(\cos \theta) + Q(N_i^t) [\gamma_C(\cos \theta) - G_C(\cos \theta)]. \quad (2-22)$$

Here γ_C is another sixth order polynomial. While:

$$Q(N_i^t) = \begin{cases} 1 & N_i^t < 3.2 \\ \frac{1}{2} [1 + \cos(2\pi(N_i^t - 3.2))] & 3.2 < N_i^t < 3.7, \\ 0 & N_i^t > 3.7 \end{cases} \quad (2-23)$$

where N_i^t is the total number of neighbors:

$$N_i^t = \sum_{elm} N_i^{elm}. \quad (2-24)$$

The term that captures radicals and conjugation is a tricubic spline:

$$\Pi^{RC} = F_{ij}(N_i^t, N_j^t, N_{ij}^{conj}), \quad (2-25)$$

which is dependent on the total number of neighbors of atom i and j , and the number of conjugate neighbors N_{ij}^{conj} . The number of conjugate neighbors (N_{ij}^{conj}) is dependent on the number of carbon neighbors of atom i and j ,

$$N_{ij}^{conj} = 1 + [\sum_{k \neq i, j}^{carbon} f_C(r_{ik})F(X_{ik})]^2 + [\sum_{l \neq i, j}^{carbon} f_C(r_{jl})F(X_{jl})]^2. \quad (2-26)$$

Here the function $F(x_{ik})$ is:

$$F(x_{ik}) = \begin{cases} 1 & x_{ik} < 2 \\ \frac{1}{2} [1 + \cos(2\pi(x_{ik} - 2))] & 3 < x_{ik} < 3, \\ 0 & x_{ik} > 3 \end{cases}, \quad (2-27)$$

and the function x_{ik} is:

$$x_{ik} = N_i^t - f_C(r_{ik}). \quad (2-28)$$

To capture the rotation of groups around a carbon-carbon bonds a dihedral function is used with the form:

$$b_{ij}^{DH} = T_{ij}(N_i^t, N_j^t, N_{ij}^{conj}) [\sum_{k \neq l, j}^{carbon} \sum_{l \neq i, j}^{carbon} (1 - \cos^2 \Theta_{kijl}) f_C(r_{jl}) f_C(r_{ik})]. \quad (2-29)$$

where Θ_{kijl} is the torsional angle between atoms k, i, j and l , $f_C(r_{ik})$ is the cutoff function and T_{ij} is a tricubic spline. The $\cos \Theta_{kijl}$ function is found using the vectors \mathbf{r}_{ik} , \mathbf{r}_{ij} and \mathbf{r}_{jl} in the following way:

$$\cos \Theta_{kijl} = \left[\frac{(\mathbf{r}_{ik} \times \mathbf{r}_{ij}) \cdot (\mathbf{r}_{ij} \times \mathbf{r}_{jl})}{r_{ik} r_{jl} r_{ij}^2 \sin \theta_{jik} \sin \theta_{ijl}} \right]. \quad (2-30)$$

The second generation REBO potential has successfully modeled mechanical and thermal properties of carbon nanostructures⁶⁰⁻⁶³, as well as ion beam modification of polymers and nano-materials, including carbon nanotubes (CNTs)^{42, 64-66}.

While the second generation REBO potential is usually only applied to first nearest neighbors, long range interactions are crucial in many systems including polymers and graphite. There have been multiple efforts to extend the REBO formalism beyond the maximum cutoff R^{max} . First, and the most straightforward, is to couple the REBO potential with a LJ potential, to produce a new potential function:

$$E = E^{REBO} + E^{LJ}. \quad (2-31)$$

Here, E^{REBO} is the pair potential summation of Equation (2-9), and E^{LJ} is the pair potential summation in Equation (2-6). Interpolating between the two functions is done using a cubic spline. Cubic spline coefficients are generated to form a continuous transition from the REBO potential to the LJ potential between the maximum REBO potential cutoff R^{max} and $0.95\sigma_{ij}$. The LJ potential cutoff is set at $2.5\sigma_{ij}$. The parameters ϵ_{ij} and σ_{ij} are calculated based on the element dependent parameters using mixing rules, where:

$$\epsilon_{ij} = \sqrt{\epsilon_i \epsilon_j} \quad (2-32)$$

and

$$\sigma_{ij} = \frac{1}{2}(\sigma_i + \sigma_j). \quad (2-33)$$

Stuart et al. coupled the first generation REBO potential to a Lennard-Jones (LJ) potential⁴⁸ using a switching function to create the adaptive intermolecular REBO

(AIREBO) potential⁶⁷. The switching function is added as a term to the LJ potential in Equation (2-31) and makes the LJ energy component into:

$$E_{ij}^{LJ} = S(t_r(r_{ij}))S(t_b(b_{ij}^*))C_{ij}V_{ij}^{LJ} + [1 - S(t_r(r_{ij}))]C_{ij}V_{ij}^{LJ}. \quad (2-34)$$

Here $S(t)$ is a universal switching function:

$$S(t) = \theta(-t) + \theta(t)\theta(1-t)[1 - t^2(3 - 2t)], \quad (2-35)$$

and $\theta(t)$ is the Heaviside step function. The function $t_r(r_{ij})$ allows for switching to depend on the distance between the pair. The function $t_b(b_{ij}^*)$ creates a dependence on a hypothetical bond order term b_{ij}^* , and C_{ij} depends on the number of neighbors of atom i and j . AIREBO has been shown to more accurately capture the graphite to diamond transition than the original REBO potential⁶⁷. Also the AIREBO potential has been used to model sputtering of molecular solids^{44, 68}.

Recently Pastewka et al.⁶⁹ implemented a screening function into the REBO potential in order to efficiently extend the bond dissociation and formation to longer distances. The function used is based on the screening function used in the modified embedded atom method (MEAM) potential⁷⁰. Rather than extending the potential by coupling the REBO potential to a LJ potential, atoms beyond the short range cutoff R^{max} are included using a modified cutoff function:

$$f_c(r_{ij}) = f_c^{12}(r_{ij}) + [1 - f_c^{12}(r_{ij})]f_c^{34}(r_{ij})S_{ij}. \quad (2-36)$$

Here $f_c^{12}(r_{ij})$ is the same as the second generation REBO potential cutoff function Equation (2-17), $f_c^{34}(r_{ij})$ is the same cutoff function applied the edge of the screening

region, and S_{ij} is the screening function. The formalism of $f_C^{34}(r_{ij})$ remains the same as $f_C^{12}(r_{ij})$, except the values of R^{min} and R^{max} for the screening region are given dependencies on the terms in which they appear. In particular, different cutoff regions are used for the cutoff functions in the pair term, angular term and neighbor terms. This modifies $f_C(r_{ij})$ in Equation (2-9), Equation (2-19) and Equation (2-20) into separate cutoff functions: $f_C^{pr}(r_{ij})$, $f_C^{ang}(r_{ij})$ and $f_C^{nb}(r_{ij})$, respectively. Where each of the new cutoff functions has the form of Equation (2-36), except with different cutoff regions R_{pair}^{min} , R_{pair}^{max} , R_{angle}^{min} , R_{angle}^{max} , R_{neigh}^{min} and R_{neigh}^{max} .

The screening region is similar to the LJ region, in that it extends atomic interactions beyond the first nearest neighbor shell. Including atoms in this region is not only computationally inefficient, but also inappropriate for functions dependent on the number of neighbors N_i^{elm} , in Equation (2-20). In order to maintain efficiency and the correct number of neighbors, atoms in the screening region can be effectively screened out based on the evaluation of the function:

$$S_{ij} = \prod_{k, C_{ijk} < C_{max}} \exp \left[- \left(\frac{C_{max} - C_{ijk}}{C_{ijk} - C_{min}} \right)^2 \right]. \quad (2-37)$$

Here C_{ijk} is an ellipsoidal function that is dependent on the ratios of r_{ik} and r_{jk} to that of r_{ij} . The new parameters in the screening function C_{min} and C_{max} , and in the cutoff function of the screening region R_{pair}^{min} , R_{pair}^{max} , R_{angle}^{min} , R_{angle}^{max} , R_{neigh}^{min} and R_{neigh}^{max} are fit to the interlayer spacing of graphite. This has improved modeling of crack propagation in diamond and the fracture of CNTs⁶⁹.

Another method is the long-range carbon bond order potential II (LCBOPII)⁷¹, which includes the long range term as modified Morse potential⁷². The primary motivation for the development of these complex long range interactions is the proper description of the graphite to diamond transition barrier that is ill defined with the first generation REBO potential. However, these complex modifications come with added computational costs. For example, the AIREBO potential was found to be an order of magnitude slower than the first generation REBO potential⁷³.

2.3 Quantum Mechanical Modeling of Materials

The particles governing most interatomic interactions in materials are electrons. To determine the behavior of a single electron i in an external field, V , one must find its wavefunction Ψ_i by solving the single particle time-dependent Schrödinger equation⁷⁴:

$$-\frac{\hbar^2}{2m_e} \nabla^2 \Psi_i + V\Psi_i = i\hbar \frac{\partial \Psi_i}{\partial t}. \quad (2-38)$$

Here m_e is the mass of the electron, ∇^2 is the Laplacian operator, and \hbar is Planck's constant divided by 2π . By using separation of variables, the time independent Schrödinger equation can be found to be:

$$-\frac{\hbar^2}{2m_e} \nabla^2 \psi_i + V\psi_i = E_i \psi_i, \quad (2-39)$$

where E_i is the energy related to time independent wavefunction ψ_i . This can be written more compactly using the Hamiltonian operator \hat{H} ,

$$\hat{H}\psi_i = E\psi_i. \quad (2-40)$$

The Hamiltonian operator acting on the eigenfunction ψ_i produces an eigenvalue that is the associated to the energy of the quantum particle.

2.1.1 Molecular Orbital Theory

Systems of interest to materials science have multiple electrons interacting with multiple positive nuclei. For these systems the Hamiltonian is a bit more complex:

$$\hat{H} = -\sum_i^{N_e} \frac{\hbar}{2m_e} \nabla_i^2 - \sum_k^{N_n} \frac{\hbar}{2m_k} \nabla_k^2 - \sum_i^{N_e} \sum_k^{N_n} \frac{e^2 Z_k}{r_{ik}} + \sum_{i<j}^{N_e} \frac{e^2}{r_{ij}} + \sum_{k<l}^{N_n} \frac{e^2 Z_k Z_l}{r_{kl}}. \quad (2-41)$$

In this equation, N_e and N_n are the number of electrons and nuclei in the system, m_k is the mass of nuclei k and r_{ij} is the scalar distance from particle i to particle j ⁷⁵. The first and second terms are the kinetic energies of the electrons and nuclei, the third, fourth and fifth terms are electron and nuclei, inter electron and inter nuclei Coulombic interactions. Unfortunately, there is no analytical solution to the multi-body quantum mechanical system. Consequently approximations must be used.

The most obvious and powerful is the Born-Oppenheimer approximation, which allows the nuclei to be treated as classical particles whose motion is negligible with respect to that of the electrons⁷⁶. This removes the second and fifth terms from Equation (2-41) to create the following all-electron Hamiltonian:

$$\hat{H}_{el} = \hat{T}_{el} + \hat{V}_{el} + \hat{V}_{ext}. \quad (2-42)$$

Here, \hat{T}_{el} is the kinetic energy of the electrons, \hat{V}_{el} is potential of the electrons interacting with themselves (known as correlation) and \hat{V}_{ext} is the potential of the electrons and the surrounding environment. This external potential is a generalization of the third term in Equation (2-41).

2.1.1.1 Slater determinants

Now that the N_{el} electron Hamiltonian (Equation (2-42)) has been constructed, the form of the wavefunction needs to be addressed. This can be done by using a spin dependent wavefunction of N_{el} electrons, $\Phi(\mathbf{r}_1 s_1, \mathbf{r}_2 s_2, \dots, \mathbf{r}_{N_{el}} s_{N_{el}})$, where \mathbf{r}_i is the

position and s_i is the spin state of electron i . A simple way to construct such a function is as the product of N_{el} single electron functions (Fock approximation):

$$\Phi = \prod_{i=1}^{N_{el}} \psi_i . \quad (2-43)$$

Since electrons are fermions the Pauli exclusion principle applies, which states that the wavefunction of two fermions is:

$$\Phi(r_1s_1, r_2s_2) = \psi_1(r_1s_1)\psi_2(r_2s_2) - \psi_1(r_2s_2)\psi_2(r_1s_1). \quad (2-44)$$

This stipulates that two electrons cannot have the same state⁷⁴. To capture this, the product in Equation (2-43) can be replaced by a linear combination of products (Hartree-Fock approximation), with alternating positive and negative terms over each permutation of r_i and r_j . This is conveniently expressed as the determinate of a $N_{el} \times N_{el}$ matrix known as a Slater determinant:

$$\Phi(r_1s_1, r_2s_2, \dots, r_{N_{el}}s_{N_{el}}) = \frac{1}{\sqrt{N_{el}!}} \begin{bmatrix} \psi_1(r_1s_1) & \dots & \psi_1(r_{N_{el}}s_{N_{el}}) \\ \vdots & \ddots & \vdots \\ \psi_{N_{el}}(r_1s_1) & \dots & \psi_{N_{el}}(r_{N_{el}}s_{N_{el}}) \end{bmatrix}. \quad (2-45)$$

2.1.1.2 Basis sets

While the Slater determinate provides a form to properly capture the Pauli exclusion principle, it does not provide a form for the individual wavefunctions ψ_i . One approach is to generate molecular wavefunctions as linear combinations of atomic wavefunctions φ_l :

$$\psi_i = \sum_{l=1}^n c_l \varphi_l. \quad (2-46)$$

This is referred to as the linear combination of atomic orbitals (LCAO) basis set.

Modern basis sets employ linear combinations of localized functions such as Gaussians, or periodic functions such as plane waves. Localized basis sets used in this work include the 6-31G* basis set, which employs 6 primitive Gaussians and a double-zeta polarized basis set for the valence electrons.

2.1.1.3 Self consistent field method

Now that the nature of the electron wavefunction has been established a method to solve for it needs to be determined. The key to this is the variational principle, which states that for any set of wavefunctions Φ :

$$\frac{\int \Phi \hat{H} \Phi d\mathbf{r}}{\int \Phi^2 d\mathbf{r}} \geq E_0, \quad (2-47)$$

where E_0 is the ground state energy of the system. This gives the criterion that the lower energy a set of wavefunctions predicts; the more accurately it describes the ground state of the system.

The Hartree-Fock Hamiltonian⁷⁷ for a single electron in a multi electron system is:

$$f_i = -\frac{1}{2}\nabla^2 + \sum_k^{N_n} \frac{Z_k}{r_{ik}} + 2(\varphi_m \varphi_n | \varphi_a \varphi_b) - (\varphi_m \varphi_a | \varphi_n \varphi_b). \quad (2-48)$$

Here the integrals $(\varphi_m \varphi_n | \varphi_a \varphi_b)$ and $(\varphi_m \varphi_a | \varphi_n \varphi_b)$ are:

$$(\varphi_m \varphi_n | \varphi_a \varphi_b) = \int \int \varphi_m(r_1 s_1) \varphi_n(r_1 s_1) \frac{1}{r_{12}} \varphi_a(r_2 s_2) \varphi_b(r_2 s_2) d\mathbf{r}_1 d\mathbf{r}_2 \quad (2-49)$$

and:

$$(\varphi_m \varphi_a | \varphi_n \varphi_b) = \int \int \varphi_m(r_1 s_1) \varphi_a(r_1 s_1) \frac{1}{r_{12}} \varphi_n(r_2 s_2) \varphi_b(r_2 s_2) d\mathbf{r}_1 d\mathbf{r}_2 \quad (2-50)$$

These integrals are a result of implementing the Slater determinant wavefunction, and applying it to the electron-electron interactions⁷⁷. Applying the variational principle to the electron Hamiltonian and the Slater determinate composed of a given basis set yields the following energy expression:

$$E = \frac{\int (\sum_i c_i \varphi_i) \hat{F} (\sum_j c_j \varphi_j) d\mathbf{r}}{\int (\sum_i c_i \varphi_i) (\sum_j c_j \varphi_j) d\mathbf{r}}, \quad (2-51)$$

where the coefficient summations can be removed from the integrals to produce:

$$E = \frac{\sum_{ij} c_i c_j \int \varphi_i \hat{F} \varphi_j d\mathbf{r}}{\sum_{ij} c_i c_j \int \varphi_i \varphi_j d\mathbf{r}}. \quad (2-52)$$

The integrals in Equation (2-52) can be denoted as F_{ij} and S_{ij} , for the numerator and denominator, respectively. As the minimization of this function is the criterion for the ground state energy, setting the first derivative to zero allows one to solve for the coefficients via the secular equation,

$$\begin{bmatrix} F_{11} - ES_{11} & \cdots & F_{1n} - ES_{1n} \\ \vdots & \ddots & \vdots \\ F_{n1} - ES_{n1} & \cdots & F_{nn} - ES_{nn} \end{bmatrix} = 0. \quad (2-53)$$

Explicitly the element F_{mn} is :

$$F_{mn} = \left\langle \varphi_m \left| -\frac{1}{2} \nabla^2 \right| \varphi_n \right\rangle + \sum_k^{N_n} Z_k \left\langle \varphi_m \left| \frac{1}{r_k} \right| \varphi_n \right\rangle + \sum_{ab} P_{ab} \left[(\varphi_m \varphi_n | \varphi_a \varphi_b) + 12 \varphi_m \varphi_a \varphi_n \varphi_b \right]. \quad (2-54)$$

Here P_{ab} is the electron density matrix defined by:

$$P_{ab} = 2 \sum_i^{\text{occupied}} c_{ai} c_{bi}. \quad (2-55)$$

To determine the Hamiltonian's dependence on the wavefunction in the form of the electron density in this equation seems unsolvable. Fortunately, Hartree proposed a solution to this dilemma in 1928 in the form of iteration. In particular, an initial set of wavefunctions are guessed and used to calculate the predicted energy and iterated wavefunctions. The iterated wavefunctions are used to solve for a new set of wavefunctions. This process is repeated until the difference in energy predicted by sequential wavefunctions falls below a predetermined criterion. This process is known as the self consistent field (SCF) method⁷⁸. It should be noted that the first computer was not created until 11 years after this method was proposed. Thus, initial SCF methods were calculated manually, which limited its application to relatively simple systems.

2.1.2 Density Functional Theory

As is shown in Hartree-Fock theory, the electron Hamiltonian (Equation (2-48)) of a multi-body system consisting of N_{el} electrons is dependent on the wave equations of the entire system. These wavefunctions can be expressed in terms of the electron density $\rho(\mathbf{r})$. Considering this, in 1927 Thomas⁷⁹ and Fermi⁸⁰ developed an expression for the energy of the system that was a functional of the electron density, thus establishing the foundation of density functional theory (DFT). It can be seen that the electron nuclei and the electron Coulombic terms Equation (2-41) can be expressed in terms of electron density⁷⁵ as follows:

$$V_{ext}[\rho(\mathbf{r})] = \sum_k^{N_n} \int \frac{Z_k}{|\mathbf{r} - \mathbf{r}_k|} \rho(\mathbf{r}) d\mathbf{r} \quad (2-56)$$

and

$$V_{el}[\rho(\mathbf{r})] = \frac{1}{2} \iint \frac{\rho(\mathbf{r}_1)\rho(\mathbf{r}_2)}{|\mathbf{r}_1 - \mathbf{r}_2|} d\mathbf{r}_1 d\mathbf{r}_2. \quad (2-57)$$

Here, \mathbf{r}_1 and \mathbf{r}_2 are dummy variables running over all space. While this established the concept of a potential as a functional of a charge density distribution, it was not until many years later that the DFT was established for practical purposes.

2.1.2.1 Hohenberg-Kohn theorems

In 1964 Hohenberg and Kohn established two theorems which helped form modern DFT⁸¹. The first theorem is known as the existence theorem and states that the electron's interaction with an external potential V_{ext} is determined by the ground state density $\rho_0(r)$ ⁸¹. Therefore, the ground state density determines the Hamiltonian, which determines the ground state wavefunctions, and all excited states of the wavefunctions.

Suppose there are two different external potentials V_{ext}^a and V_{ext}^b , which lead to two different Hamiltonians, \hat{H}^a and \hat{H}^b , and wavefunctions, Φ^a and Φ^b . If it is assumed that each external potential has the same ground state density $\rho_0(r)$, but Φ^b is not the lowest energy state of \hat{H}^a then:

$$E^a = \langle \Phi^a | \hat{H}^a | \Phi^a \rangle < \langle \Phi^b | \hat{H}^a | \Phi^b \rangle, \quad (2-58)$$

where:

$$\begin{aligned} \langle \Phi^b | \hat{H}^a | \Phi^b \rangle &= \langle \Phi^b | \hat{H}^b | \Phi^b \rangle + \langle \Phi^b | \hat{H}^a - \hat{H}^b | \Phi^b \rangle \\ &= E^b + \int d^3r [V_{ext}^a - V_{ext}^b] \rho(r). \end{aligned} \quad (2-59)$$

Consequently:

$$E^a < E^b + \int d^3r [V_{ext}^a - V_{ext}^b] \rho(r). \quad (2-60)$$

However, if the same argument is recast interchanging the labels of a and b it can be shown that:

$$E^b < E^a + \int d^3r [V_{ext}^b - V_{ext}^a] \rho(r). \quad (2-61)$$

Via *reductio ad absurdum*, Equation (2-61) shows that there cannot be two different external potentials with the same ground state density. Therefore, the density uniquely determines the external potential.

The second theorem shows that the density also obeys a variational principle Equation (2-47). In particular, as theorem I states, the density determines the external potential, which can be used to calculate the system energy. Thus, for a set of densities, the one which has the lowest energy is the ground state.

Considering a ground state density ρ^a , with a Hamiltonian \hat{H}^a , and a wavefunction Φ^a evaluating for the energy:

$$E^a = E[\rho^a] = \langle \Phi^a | \hat{H}^a | \Phi^a \rangle. \quad (2-62)$$

If another density ρ^b is considered with a wavefunction Φ^b , it follows that E^b must be greater than E^a since:

$$E^a = \langle \Phi^a | \hat{H}^a | \Phi^a \rangle < \langle \Phi^b | \hat{H}^a | \Phi^b \rangle = E^b, \quad (2-63)$$

thus giving a function of the total energy in the form of:

$$E_{HK} = T[\rho(r)] + E_{el}[\rho(r)] + \int d^3r V_{ext}(r) \rho(r). \quad (2-64)$$

Energy E_{HK} can be minimized by varying the electron density. This establishes the ground state density.

2.1.2.2 Kohn-Sham theorem

The theorems of Hohenberg and Kohn established DFT as a valid theory. However, this is no better than Hartree-Fock (HF) theory presented in the previous section. Since, all that has been done is replacing the iterative minimization of the energy with respect to a wavefunction, with an iterative minimization with respect to a charge density. The key to establishing DFT as an efficient tool was developed by Kohn and Sham⁸² in 1965. Their ansatz was “to replace the original many-body problem by an auxiliary independent particle problem.” This rests on two assumptions.

First is the “non-interacting-V-representability” which states that the exact ground state of the electron density can be represented by the ground state density of an auxiliary system of non-interaction particles. The second assumption is to create an auxiliary Hamiltonian of a single non-interacting electron with a kinetic energy term and an effective local potential V_{eff} ,

$$\hat{H}_{aux} = -\frac{1}{2}\nabla^2 + V_{eff}(\mathbf{r}, s). \quad (2-65)$$

The energy of the Kohn-Sham auxiliary system is:

$$E_{KS}(\chi_i) = \sum_i^N \left(\left\langle \chi_i \left| -\frac{1}{2}\nabla_i^2 \right| \chi_i \right\rangle - \left\langle \chi_i \left| \sum_k^{N_{nuc}} \frac{Z_k}{|\mathbf{r}_{ik}|} \right| \chi_i \right\rangle \right) + \sum_i^{N_{el}} \left\langle \chi_i \left| \frac{1}{2} \int \frac{\rho(\mathbf{r}')}{|\mathbf{r}_i - \mathbf{r}'|} d\mathbf{r}' \right| \chi_i \right\rangle + E_{XC}[\rho(\mathbf{r})], \quad (2-66)$$

where the last term $E_{XC}[\rho(\mathbf{r})]$ contains all the approximations involved in evaluating the energy of the system. Various approximations have been made and improved upon.

First is the local density approximation (LDA). This specifies that the values of E_{XC} at a particular position \vec{r} are approximated by the charge density at that point. Later improvements such as the generalized gradient approximation (GGA) were made that take the gradient of the charge density into account in the E_{XC} term.

4.3 Post HF, Hybrid and Combinatorial Methods

Hartree Fock (HF) theory and density functional theory (DFT) are the basis for many of the more complex methods currently being used in the computational materials science community; in that, many adaptations are made to improve the accuracy of these methods. HF theory is often used in conjunction with a post Hartree-Fock analysis. Post HF methods include configuration interaction (CI). CI takes correlation into account by creating a new wavefunction based on the results of a HF calculation. The new CI wavefunction is a linear combination of the HF wavefunction and sets of excited configurations, in which the occupancy of an occupied orbital is changed to unoccupied (virtual) orbital and a virtual orbital is changed to occupied. An analogous method used in this work is coupled cluster (CC) theory, where the sets of CI wavefunctions are considered. And the theory is noted accordingly CIS – singles, CISD – singles and doubles etc.

Hybrid methods use combinations of HF theory and DFT to calculate the electron wavefunctions of a system. This is done to take advantage of HF's ability to capture exchange and DFT's ability to capture correlation. A popular implementation of a hybrid method is B3LYP⁸³.

Combinatorial methods give accurate predictions of thermodynamically data. This is done by using a set of predefined calculations with different methods, and a large

basis set. These calculations are used to give chemical accurate ($\pm 1 \text{ kcal/mol}$) enthalpies of formation of molecular systems. Improved variations of these methods have been made and are designated by the suffix number of the G, in the G2⁸⁴ and G3⁸⁵ methods.

2.4 Summary

In this work the primary focus is on MD simulations using empirical potentials, and empirical potential development. Empirical potentials are a way to bypass explicitly calculating the electronic structure of a system to determine the system's properties. These potentials have developed over the decades to become more complex and accurate. The potential formalism focused on in this work is the second generation reactive empirical bond order (REBO) potential. This potential is well established for use in modeling hydrocarbon systems, and allows for bond breaking and formation.

Furthermore, quantum mechanical based methods are used for calculating datasets for fitting potential parameters, and by collaborators to calculate reaction enthalpies and transition states. In these calculations hybrid methods and combinatorial methods are often employed. Hybrid methods such as B3LYP⁸³ use combinations of HF based theory and DFT to calculate the electron wavefunctions a system. Combinatorial methods like the G3⁸⁵ method use multiple thermodynamically calculations to achieve accurate predictions of molecular enthalpies.

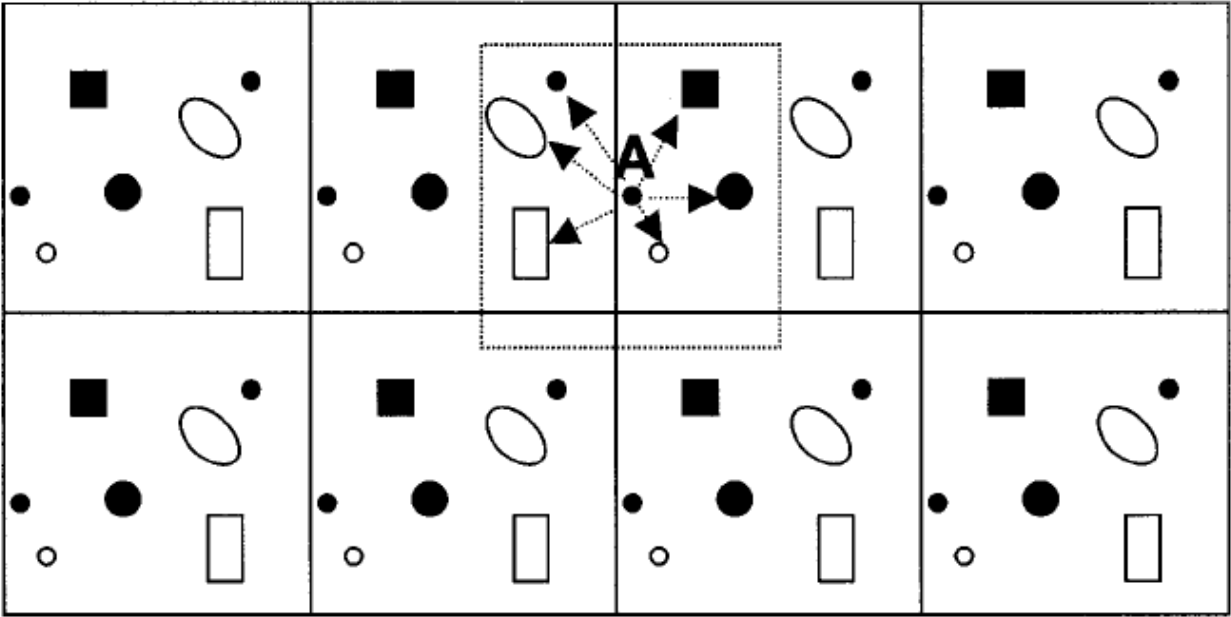


Figure 2-1. Periodic boundary conditions

CHAPTER 3 POTENTIAL DEVELOPMENT

3.1 REBO Oxygen

The second generation REBO potential was parameterized to include oxygen interactions with hydrocarbons by Ni et al. in 2004⁸⁶. There have been some issues with the energetics of this potential, and some modifications to the coordination function have been made post publication. Changes include the adjustment of $P_{OC}(0,0)$ from the published value of 0.0 to -0.39 to properly capture the atomization energy of the O_2 molecule. While this and other corrections were made to address some issues with the potential, the effects on other bonding situations were not fully accounted for.

Considering the current issues with the implemented form of the second generation REBO potential including oxygen (REBO CHO), the coordination function has been refit. The coordination function used in the REBO CHO potential is modified from Equation (2-19), for bonds containing oxygen or oxygen neighbors, to the function $P_{ij}(N_i^{C+H}, N_i^O)$, where N_i^{C+H} is the summation of carbon and hydrogen neighbors. In order to refit the values of this function a dataset of small molecules similar to that used by Ni et al. is considered. Specifically, molecules containing the bonds types: C_i-C_j , C_i-H_j , C_i-O_j , O_i-C_j , O_i-O_j and O_i-H_j with each possible coordination of atom i is used to find appropriate values of the function $P_{ij}(N_i^{C+H}, N_i^O)$. While the original dataset used a single molecule to determine each integer value of the coordination function, the new dataset includes molecules with each possible value of carbon neighbors (N_i^C) and hydrogen neighbors (N_i^H) for the considered bond types. In particular, the dataset includes 64 molecules with all bond types and number of nearest neighbors that satisfy the coordination criterion:

$$N_i^C + N_i^H + N_i^O \leq N_i^{full}. \quad (3-1)$$

Here, N_i^{full} represents the number of neighbors needed to achieve full coordination of a bonded atom i in one of the $i - j$ bonds included in the fitting dataset. N_i^C , N_i^H and N_i^O are the number of carbons, hydrogen and oxygen neighbors of atom i , respectively. This is done to find the best value of the coordination function that describes all possible bonding environments. Dissociation energies of each bond type along with the atomization energies are used in the refit of the coordination function and these are listed in Table 3-1, Table 3-2 and Table 3-3.

3.1.1 Parameter Fitting Results

Atomization energies and bond dissociation energies for each of the 64 molecules in the dataset are calculated using the GAUSSIAN03⁸⁷ package. Initial structures are relaxed at the B3LYP⁸³/6-31G* level. Energies of the subsequent relaxed molecules are calculated using the G3 approach⁸⁵. Zero point energy corrections are not used in calculating energies, in order to be consistent with the previous fitting done by Ni et al.⁸⁶. The values of the coordination function are fitted at each point for each bond type using the least squared fitting routine in MATLAB⁸⁸. Values of the pair and angular terms are determined based on geometries relaxed at the B3LYP/6-31G* level. Weights on the dissociation and atomization energies are adjusted to give the lowest error.

The currently implemented coordination values give dissociation energies that differ from energies calculated with the G3 method⁸⁵, by 25.8% on average, with crucial bonds energies being too low, see Table 3-1, Table 3-2 and Table 3-3. In particular, the hydroxyl carbon bond is too weak by 55.0%. The refit values reduce the average error

in dissociation energy to 16.7%. Furthermore, the hydroxyl dissociation error is improved to be within 23.0% of G3 energies. The refit coordination function values are given in Table 3-4, and the refit bond dissociation energies and atomization energies are in Table 3-1, Table 3-2 and Table 3-3. In Figure 3-1 the predicted dissociation energies from the updated REBO CHO potential are plotted as a function of energies calculated using the G3 method in order to show relative deviations for each bond type.

3.2 REBO Sulfur

Sulfur interactions with hydrocarbons play a crucial role in processes including the vulcanization of rubber⁸⁹ and its reclamation⁹⁰, oil processing, gas sensors^{91, 92}, and batteries^{93, 94}. Additionally, thiophene-based molecules and polymers are widely used in organic electronics⁹⁵⁻⁹⁷. Therefore, the second generation REBO potential is extended to include sulfur. This work thus builds on previous efforts to extend the potential to include fluorine⁴³, oxygen⁸⁶ and molybdenum disulfide⁹⁸. The parameter fitting of the sulfur hydrocarbon interactions is conducted in an analogous approach to that of oxygen⁸⁶.

3.2.1 Parameter Fitting

The dataset for the sulfur-hydrocarbon interactions consists of the properties of solid and molecular systems. The properties of the solid systems are determined using density functional theory (DFT) within the Vienna Ab-initio Simulation Package (VASP) software package^{99, 100}. The electron wavefunctions are calculated using projected augmented wave (PAW) pseudopotentials¹⁰¹. Systems are relaxed with the GGA^{102, 103} (PBE)¹⁰⁴ method, with an energy cutoff of $600eV$. A k-point mesh of $6x6x6$, and a force convergence criterion of $0.05eV/\text{\AA}$ is also used. The properties of the molecular

systems are calculated with GAUSSIAN03⁸⁷. Molecular geometries are optimized, and bond stretching and bending curves are determined at the B3LYP/6-31G* level⁸³, while atomization and dissociation energies are calculated with the G3 method⁸⁵. The changes in energy due to bond stretching and bending that are calculated with B3LYP are shifted in energy to have minima that correspond to G3 values.

The two-body related parameters, Equation (2-15) and (2-16), for the sulfur-carbon, sulfur-hydrogen and sulfur-sulfur interactions are fit prior to the multi-body parameters. In particular, the pair parameters are fit to molecular bond stretching curves and solid strain curves, which are illustrated in Figure 3-2. During the fitting of the pair-terms the multi-body term b_{ij} is left as a fitted parameter and given a range of 0.0 to 1.0. This establishes a set of pair parameters capable of capturing a range of values of the bond order term b_{ij} . Molecular species are weighted heavier than solid phases, due to the largely molecular nature of the sulfur hydro-carbon systems. The fitted pair parameters are given in Table 3-5. Potential cutoff distances R^{min} and R^{max} are chosen to be between first and second nearest neighbors within the molecular dataset. Once the minimum error for the dataset is established the angular term is then fit.

A sixth order polynomial, Equation (2-21), is used for the angular function $G(\theta)$ in congruency with the hydrocarbon angular function. This function also possesses the flexibility to capture the potential energy response to the change in angle, while maintaining reasonable values at angles less than 60°. Parameters for each sulfur centered angle type $X-S-H$, $X-S-C$ and $X-S-S$, where X is C , H or S , are fit to the bond bending curves of representative molecules, see Figure 3-3. For the $X-S-S$ parameters the S_3 molecule and the S_8 ring's bond bending curves are included in the fitting

dataset. The $X-S-C$ parameters are fit to thiobismethane, and the $X-S-H$ parameters are fit to hydrogen sulfide. Bond energies are fitted to $1eV$ at zero degrees for the sulfur-sulfur and sulfur-hydrogen terms, and $0.5eV$ for the sulfur-carbon term, to prevent the unphysical stabilization of over-coordinated structures. The resulting angular function parameters are displayed in Table 3-6.

The coordination function is fit in a similar manner as the refit of the REBO CHO coordination function. One exception is that a tricubic spline is used for the coordination function $P_{ij}(N_i^C, N_i^H, N_i^S)$ for each bond type: C_i-C_j , C_i-H_j , C_i-S_j , S_i-C_j and S_i-H_j , and the values are given in Table 3-7. The values of the C_i-H_j and C_i-C_j coordination function, where N_i^S is zero, are the same as the bicubic spline values for the second generation REBO potential, and are given in italics in Table 3-7. For hydrocarbon bonds with sulfur neighbors and sulfur hydrocarbon bonds, the coordination function values are fit to the dissociation and atomization energies of small molecules.

As with the refit of the REBO CHO coordination function, the criteria in Equation (3-1) is used in conjunction with considering possible bond order values to establish a dataset of molecules. Dissociation energies and atomization energies are calculated at the G3 level. Atomization energies are included to establish the magnitude of the total cohesive energy of the molecule, which ensures reasonable changes in energy while exploring the potential energy space of a system during a MD simulation. Dissociation energies are also included into the fitting database to ensure the best possible capturing of the change in energy during chemical reactions. The results of the fit to dissociation energies is shown in Figure 3-4; the average deviation from G3 values is 13.7%.

3.2.2 Validation and Testing

In order to test the performance of the potential under various bonding environments, atomization energies of a set of representative molecules are calculated with the modified second generation REBO potential for sulfur (REBO CHS) and compared to G3 values. Characteristic bonding environments include: elemental sulfur molecules, hydrocarbon molecules with S-S bonds, thials, thiols, sulfides and ring structures that include sulfurs. The test set includes 102 molecules, 60 of which are not included in the fitting dataset. The average error in the atomization energy is found to be 4.0% for the entire set, and 4.2% for species not included in the fitting dataset. The difference in atomization energy between the newly developed REBO CHS potential and atomization energies calculated with the G3 method for molecules containing characteristic bonds is shown in Figure 3-5.

The ground state of elemental sulfur is cyclooctasulfur, which is an eight membered crown-shaped ring¹⁰⁵. The bond length, bond angles and torsion angles of S₈ are predicted to within 1.0% of corresponding B3LYP geometries. The atomization energy of the S₈ ring is predicted within 5.0% of the G3 energy. Other purely sulfur compounds, including the sulfur dimer and S₃ and S₄ rings, are found to have an average deviation from G3 energies of 4.3%. However, these small sulfur molecules are included in the fitting dataset. Compounds not in the fitting dataset, including the S₅ and S₆ rings, are found to have atomization energies within 10% of G3 energies.

The potential captured the atomization energies of molecules containing thial and thiol groups well, with average errors of approximately 3.0% for each group. Bond lengths are also well captured. Considering, the prototypical molecules propanethione

and methanethiol have errors in $C-S$ bond lengths of 2.7% and 0.4% respectively, when compared to B3LYP geometries. The methanethiol $C-S-H$ bond angle is also predicted within 0.4% of the B3LYP geometry. For molecules containing multiple thiol groups, the hydrogen-hydrogen repulsion from the $X-H-H$ angular function from the second generation REBO potential³⁸, where X is S or C , is found to be too strong for the $S-H-H$ case. Specifically, it causes dissociation of the molecule during close contact between thiol groups. Therefore, the $S-H-H$ angular function is set to zero to mitigate this repulsion.

Sulfur bonded to two carbons is considered in the form of sulfide bonds and within ring bonds. Dimethylsulfide is fit to have a bond length within 5.0% of B3LYP, and a bond angle within 1.7%. The atomization energy for dimethylsulfide is within 2.7% of G3 values, while the average error of the test set is 4.2%. The ring molecules containing sulfur atoms are predicted with the least accuracy, with an average error in atomization energy of 5.5%. This is due to over binding of conjugate $C-C$ bonds, since the coordination function for this bonding environment is fit to $C-C$ double bonds.

3.3 Summary

The coordination function for the oxygen hydrocarbon second generation REBO potential is refit in order to improve bond dissociation energies. A more extensive dataset is created, including all possible sets of coordination of atom i for each bond type $i - j$. The average error in dissociation energy for each molecule in the fitting dataset is reduced from 23% to 16%. However the average error in atomization energies of the test set is increased from 3% to 4.2%. While undesirable, this error

remained under 5%, and is found to be unavoidable barring a complete refit of the potential.

A similar form of the second generation REBO potential is developed for the sulfur hydrocarbon system. The differences in formalism are the inclusion of a seventh order polynomial for the angular function, which is more consistent with the hydrocarbon second generation REBO potential. Also a tricubic spline is used in place of the bicubic spline used in the REBO CHO potential, as was done for the fluorocarbon REBO potential⁴³. This increase in flexibility allowed for the average error in dissociation energies to be 14% and the average error in atomization energy to be 3%.

Table 3-1. *C-C* and *C-H* bond dissociation energies (D_0) and atomization energies (ΔH_a) in eV

Molecule	Original		Refit		G3	
	D_0	ΔH_a	D_0	ΔH_a	D_0	ΔH_a
H ₃ C-COH	2.09	26.93	1.80	28.27	3.17	25.67
H ₂ C-C(OH) ₂	4.78	31.74	5.70	35.37	5.38	31.88
H ₃ C-C(OH)O	2.50	32.53	3.47	34.84	4.05	33.16
H ₃ C-C(OH) ₃	3.80	43.58	3.39	46.97	3.87	42.39
H ₂ C-C(OH)CH ₃	3.99	39.39	6.17	42.90	6.25	39.62
H ₃ C-C(CH ₃) ₂ O	2.00	40.44	3.39	41.87	3.54	40.19
H ₃ C-C(OH) ₂ H	3.26	38.76	3.28	41.51	3.68	37.50
H ₃ C-C(OH) ₂ CH ₃	3.67	51.52	3.41	54.80	3.79	49.90
H ₂ C-C(OH)H	5.26	26.96	6.22	29.69	6.49	27.39
H ₂ (HO)C-C(OH)H ₂	3.81	38.66	3.57	40.72	3.53	37.02
H ₃ C-C(OH)(H)CH ₃	4.32	47.57	3.53	48.75	3.66	45.17
H ₃ C-C(CH ₃) ₂ OH	4.71	60.40	3.37	61.83	3.65	57.39
H ₃ C-C(H)O	3.24	27.99	3.40	28.62	3.54	27.87
H-C(O)OH	3.54	20.19	3.67	21.67	4.29	20.82
H-C(OH) ₃	4.37	30.79	3.05	33.26	4.15	30.10
H-C(O)H	4.17	15.55	3.52	15.37	3.77	15.52
H-C(O)CH ₃	2.93	27.99	3.52	28.62	3.81	27.87
H-C(OH)CH ₂	3.75	26.96	5.24	29.69	4.62	27.39
H-C(OH) ₂ H	3.85	25.98	3.34	28.20	4.14	25.37
H-C(OH) ₂ CH ₃	4.28	38.76	3.49	41.51	4.11	37.64
H-C(OH)H ₂	4.46	21.88	3.75	22.33	4.11	20.86
H-C(OH)(H)CH ₃	4.84	34.72	3.69	35.54	4.06	32.99
H-C(CH ₃) ₂ OH	5.26	47.58	3.70	48.78	4.03	45.18

Table 3-2. C-O bond dissociation energies (D_O) and atomization energies (ΔH_a) in eV

Molecule	Original		Refit		G3	
	D_O	ΔH_a	D_O	ΔH_a	D_O	ΔH_a
C-O	10.14	10.14	10.17	10.17	11.12	11.12
(CH ₃ O) ₂ C-O	5.96	50.05	5.71	53.04	6.78	48.99
(HO) ₂ C-O	5.98	24.48	5.77	26.97	7.11	25.77
(HO)OC-OH	3.42	24.48	4.40	26.97	4.81	25.77
HCC-OH	4.83	20.81	5.56	21.69	5.25	20.79
HOCH-O	6.95	20.19	6.66	21.67	7.77	20.82
OCH-OH	4.40	20.19	5.25	21.67	4.63	20.82
HO(CH ₃)C-O	5.60	32.53	6.57	34.84	7.64	33.16
O(CH ₃)C-OCH ₃	0.35	45.32	3.91	47.88	4.35	44.77
HO(CH ₂)C-OH	4.10	31.73	6.35	35.37	4.79	31.99
O(CH ₃)C-OH	3.05	32.53	5.16	34.84	4.66	33.16
H(OH) ₂ C-OH	4.25	30.79	3.83	33.26	4.47	30.13
CH ₃ (OH) ₂ C-OH	4.70	43.58	4.38	46.97	4.44	42.39
H ₂ C-O	7.09	15.55	6.90	15.37	7.67	15.52
CH ₃ CH-O	3.61	27.99	4.24	28.62	4.80	27.87
CH ₂ CH-OH	3.22	26.96	5.79	29.69	4.60	27.39
(CH ₃) ₂ C-O	3.77	40.44	5.20	41.87	7.94	40.19
CH ₂ (CH ₃)C-OH	2.91	39.39	6.27	42.90	4.59	39.62
HOCH ₂ -OH	4.15	25.98	5.06	28.20	4.19	25.37
HO(CH ₃)CH-OH	4.47	38.76	5.09	41.51	4.27	37.64
HO(CH ₃) ₂ C-OH	4.79	51.52	5.15	54.80	4.32	49.90
CH ₃ OCH ₂ -OCH ₃	1.44	38.77	3.80	41.24	3.75	36.85
CH ₃ -OH	4.10	21.88	4.39	22.33	3.84	20.86
CH ₃ CH ₂ -OH	3.79	34.72	4.45	35.54	3.97	32.99
CH ₃ CH ₂ -OCH ₃	1.08	47.50	3.20	48.58	3.68	44.62
(CH ₃) ₂ CH-OH	3.78	47.58	4.82	48.78	4.07	45.18
(CH ₃) ₃ C-OH	3.75	60.40	5.02	61.83	4.13	57.39
CH ₂ C-O	6.02	21.36	5.96	21.29	7.32	22.27
HO-C(OH) ₃	3.85	34.68	4.06	38.84	4.49	34.86

Table 3-3. O-C, O-H and O-O bond dissociation energies (D_O) and atomization energies (ΔH_a) in eV

Molecule	Original		Refit		G3	
	D_O	ΔH_a	D_O	ΔH_a	D_O	ΔH_a
O-C	10.14	10.14	10.17	10.17	11.12	11.12
HOO-CH ₃	2.33	24.12	4.29	26.81	2.85	22.62
HO-CH ₃	4.10	21.88	4.39	22.33	3.84	20.86
CH ₃ O-CH ₃	1.38	34.65	3.13	35.36	3.53	32.48
O-H	4.41	4.41	4.57	4.57	4.43	4.43
HOO-H	3.20	11.61	4.34	13.48	3.71	10.89
HO-H	4.69	9.10	4.71	9.28	5.07	9.50
CH ₃ O-H	1.99	21.88	3.47	22.33	4.50	20.86
O-O	5.26	5.26	4.82	4.82	5.07	5.07
O-O ₂	0.31	5.57	1.11	5.93	1.06	6.13
HO-OH	2.79	11.61	4.35	13.48	2.02	10.89
CH ₃ O-OCH ₃	-3.18	36.61	2.39	40.11	1.65	34.36

Table 3-4. Refit spline values for oxygen hydrocarbon interactions

N^C+N^H	N^O	P_{CC}	P_{CH}	P_{CO}	P_{OC}	P_{OH}	P_{OO}
0	0	0.000	0.000	-0.500	-0.102	-0.025	-0.032
0	1	0.263	0.336	-0.138	0.057	-0.022	0.020
0	2	0.182	0.635	-0.120	0.000	0.000	0.000
0	3	-0.338	-0.507	-0.193	0.000	0.000	0.000
1	0	0.000	0.000	-0.207	0.374	-0.013	-0.003
1	1	0.007	0.191	-0.245	0.000	0.000	0.000
1	2	-0.146	-0.144	-0.075	0.000	0.000	0.000
2	0	0.000	0.000	-0.185	0.000	0.000	0.000
2	1	-0.188	-0.354	-0.209	0.000	0.000	0.000
3	0	0.000	0.000	0.585	0.000	0.000	0.000

Table 3-5. Pair parameters

	S-C	S-H	S-S
$A(eV)$	755.86	1033.73	4489.11
α	1.90	0.81	1.79
$Q(\text{\AA})$	0.95	0.09	0.16
$B1(eV)$	1423.74	1167.23	4906.07
β_1	1.94	0.85	1.78
$R^{\min}(\text{\AA})$	2.1	1.5	2.3
$R^{\max}(\text{\AA})$	2.4	1.8	2.6

Table 3-6. Angular parameters

	X-S-C	X-S-H	X-S-S
a_1	6.97E-02	2.95E-03	1.88E-02
a_2	5.80E-02	1.60E-03	6.86E-02
a_3	2.11E-01	1.83E-02	8.07E-02
a_4	1.38E-01	2.74E-02	-7.64E-02
a_5	-6.63E-02	1.14E-02	-5.44E-02
a_6	-1.31E-01	-1.98E-02	2.54E-02
a_7	-2.01E-03	-1.20E-02	1.48E-02

Table 3-7. Tricubic spline values for the coordination function P_{ij}

N^C	N^H	N^S	P_{CC}	P_{CH}	P_{CS}	P_{SC}	P_{SH}	P_{SS}
0	0	0	0.0	0.0	0.3412	-0.2315	-0.0018	0.0007
0	0	1	-0.0128	0.9398	0.4869	-0.2844	-0.0052	0.0141
0	0	2	0.1210	0.4464	0.4738	0.0	0.0	0.1089
0	0	3	-0.0168	-0.2290	0.3476	0.0	0.0	0.0
0	1	0	0.0	0.2093	0.3797	-0.2138	-0.0063	0.0111
0	1	1	0.0671	0.2899	0.4090	0.0	0.0	0.1028
0	1	2	-0.0770	-0.4419	0.3480	0.0	0.0	0.0
0	2	0	0.0079	-0.0644	0.3389	0.0	0.0	0.1054
0	2	1	0.0126	-0.2852	0.4293	0.0	0.0	0.0
0	3	0	0.0161	-0.3039	0.4405	0.0	0.0	0.0
1	0	0	0.0	0.0100	0.5200	-0.2765	-0.0107	0.0070
1	0	1	0.0950	0.4279	0.4288	0.0	0.0	0.1063
1	0	2	-0.1650	-0.3032	0.3394	0.0	0.0	0.0000
1	1	0	0.0030	-0.1251	0.3142	0.0	0.0	0.1051
1	1	1	-0.1282	-0.3864	0.3380	0.0	0.0	0.0
1	2	0	0.0063	-0.2989	0.4099	0.0	0.0	0.0
2	0	0	0.0	-0.1220	0.3175	0.0	0.0	0.0494
2	0	1	-0.0927	-0.2156	0.3848	0.0	0.0	0.0
2	1	0	0.0032	-0.3005	0.4000	0.0	0.0	0.0
3	0	0	0.0	-0.3076	0.3966	0.0	0.0	0.0

Table 3-8. C-C bond dissociation energies (D_0) and atomization energies (ΔH_a) in eV

Molecule	REBO		G3	
	D_0	ΔH_a	D_0	ΔH_a
H ₂ C-CS	4.82	20.13	5.04	20.81
H ₃ C-CS	3.42	23.63	2.04	22.85
HC-CSH	7.33	21.26	8.34	20.08
H ₂ C-C(SH) ₂	5.33	30.40	5.84	29.55
H ₃ C-C(SH)S	2.87	30.05	3.75	30.01
HC-C(SH) ₂	4.31	25.44	5.25	24.37
H ₂ C-C(SH) ₃	3.65	35.06	3.89	33.56
H ₃ C-C(SH) ₃	3.02	39.34	3.57	38.29
H ₂ C-CH(SH)	6.30	27.51	6.62	26.95
H ₂ C-CH(SH)	3.75	27.25	4.30	27.12
HC-CH(SH)	5.24	22.52	6.07	21.80
H ₂ C-C(SH)CH ₃	5.61	40.56	6.52	39.88
H ₃ C-C(CH ₃)S	3.33	40.34	3.91	40.10
HC-C(CH ₃)SH	4.59	35.60	5.92	34.67
H ₂ C-CH(SH) ₂	4.06	32.51	4.10	31.09
H ₃ C-CH(SH) ₂	3.47	36.83	3.75	35.78
H ₂ C-C(SH) ₂ CH ₃	4.01	45.42	4.11	43.98
H ₃ C-C(SH) ₂ CH ₃	3.33	49.64	3.78	48.69
H ₂ C-CH ₂ SH	4.22	29.36	4.20	28.55
(HS)CH ₂ -CH ₂ (SH)	3.13	36.49	3.60	35.71
H ₂ C-CH(SH)CH ₃	4.02	42.39	4.25	41.45
H ₃ C-CH(SH)CH ₃	3.36	46.64	3.89	46.13
H ₂ C-C(CH ₃) ₂ SH	3.71	55.21	4.24	54.33
H ₃ C-C(CH ₃) ₂ SH	3.02	59.43	3.88	59.01

Table 3-9. C-H bond dissociation energies (D_0) and atomization energies (ΔH_a) in eV

Molecule	REBO		G3	
	D_0	ΔH_a	D_0	ΔH_a
H-CS	3.29	10.13	2.31	9.78
H-CSH	3.34	12.75	4.05	12.10
H-C(S)SH	3.33	17.14	4.12	17.04
H-C(SH) ₃	3.45	26.39	3.98	25.36
H-CH(S)	3.89	14.02	4.33	14.12
H-CH(SH)	3.93	16.68	4.02	16.05
H-C(S)CH ₃	3.62	27.25	4.27	27.12
H-C(SH)CH ₂	4.53	27.51	4.83	26.95
H-C(SH) ₂ H	3.53	23.52	4.24	22.93
H-C(SH) ₂ CH ₃	3.89	36.83	4.22	35.79
H-CH ₂ (SH)	3.80	20.48	4.44	20.49
H-CH(SH)CH ₃	3.73	33.64	4.38	33.27
H-C(CH ₃) ₂ SH	3.62	46.66	4.34	46.13

Table 3-10. C-S bond dissociation energies (D_0) and atomization energies (ΔH_a) in eV

Molecule	REBO		G3	
	D_0	ΔH_a	D_0	ΔH_a
C-S	6.84	6.84	7.48	7.48
SC-S	4.17	11.02	4.70	12.18
HSC-SH	3.37	16.60	3.55	15.39
(CH ₃ S) ₂ C-S	3.08	47.33	4.43	45.56
(HS) ₂ C-S	3.37	19.97	4.38	19.80
(HS)SC-SH	2.32	19.97	3.09	19.80
(HS) ₃ C-S	3.24	26.19	2.57	23.95
(HS) ₃ C-SH	2.45	29.23	2.60	27.76
HC-S	5.61	10.13	5.79	9.48
HC-SH	4.39	12.75	4.62	12.10
CH ₂ C-S	4.79	20.13	5.23	20.81
HCC-SH	5.86	21.26	4.82	20.08
SHCH-S	4.40	17.14	5.01	17.04
SCH-SH	3.18	17.14	3.77	17.04
CH ₃ (SH)C-S	3.57	30.05	4.95	30.01
CH ₃ (S)C-SCH ₃	2.71	43.78	3.51	42.90
CH ₂ (SH)C-SH	3.57	30.38	3.62	29.52
CH ₃ (S)C-SH	2.58	30.05	3.38	30.01

Table 3-11. C-S bond dissociation energies (D_0) and atomization energies (ΔH_a) in eV

Molecule	REBO		G3	
	D_0	ΔH_a	D_0	ΔH_a
(SH) ₂ C-S	3.40	23.39	2.78	21.47
(SH) ₂ CH-SH	2.57	26.39	2.88	25.36
CH ₃ (SH) ₂ C-S	3.39	36.32	2.86	34.43
CH ₃ (SH) ₂ C-SH	2.57	39.34	2.93	38.29
CH ₂ C-S	5.56	14.02	5.82	14.12
CH ₃ CH-S	4.40	27.25	6.07	27.12
CH ₂ CH-SH	4.34	27.51	3.87	26.95
(CH ₃) ₂ C-S	3.67	40.34	5.87	40.10
CH ₂ (CH ₃)C-SH	4.67	40.56	3.80	39.88
HSCH ₂ -SH	3.75	20.43	2.94	18.99
HSCH ₂ -S	3.00	23.51	2.97	22.81
HS(CH ₃)C-S	4.02	33.93	3.01	31.89
HS(CH ₃)CH-SH	3.09	36.83	3.12	35.79
HS(CH ₃) ₂ CH-S	3.55	46.59	3.04	44.83
HS(CH ₃) ₂ CH-SH	2.77	49.64	3.11	48.69
HSCH ₂ -SH	2.97	37.10	3.05	35.64
CH ₃ -S	4.07	17.44	3.20	16.54
CH ₃ -SH	3.28	20.48	3.37	20.49
CH ₃ CH ₂ -S	4.10	30.62	3.20	29.33
CH ₃ CH ₂ -SH	3.28	33.64	3.36	33.27
CH ₃ CH ₂ -SCH ₃	3.31	47.28	3.33	46.00
(CH ₃) ₂ CH-S	4.24	43.64	3.18	42.15
(CH ₃) ₂ CH-SH	3.43	46.66	3.37	46.13
(CH ₃) ₃ C-S	4.17	56.41	3.15	55.02
(CH ₃) ₃ C-SH	3.35	59.43	3.35	59.01
H ₂ C-S	4.38	16.68	3.97	16.05

Table 3-12. C-S, S-H and S-S bond dissociation energies (D_0) and atomization energies (ΔH_a) in eV

Molecule	REBO		G3	
	D_0	ΔH_a	D_0	ΔH_a
(CH ₃)C-SSH	3.35	24.15	2.82	23.15
(CH ₃)C-SH	3.28	20.48	3.37	20.49
CH ₃ -SCH ₃	3.29	34.10	3.34	33.22
S-H	3.83	3.83	3.79	3.79
HSS-H	3.24	10.66	3.36	10.35
HS-H	4.12	7.95	4.10	7.89
CH ₃ S-H	3.04	20.48	3.95	20.49
S-S	4.26	4.26	4.37	4.37
S ₈	2.87	22.95	2.75	21.98
S ₃	2.77	7.03	2.70	7.07
HS-SH	2.99	10.66	2.78	10.35
CH ₃ S-SCH ₃	2.76	37.64	2.87	35.95

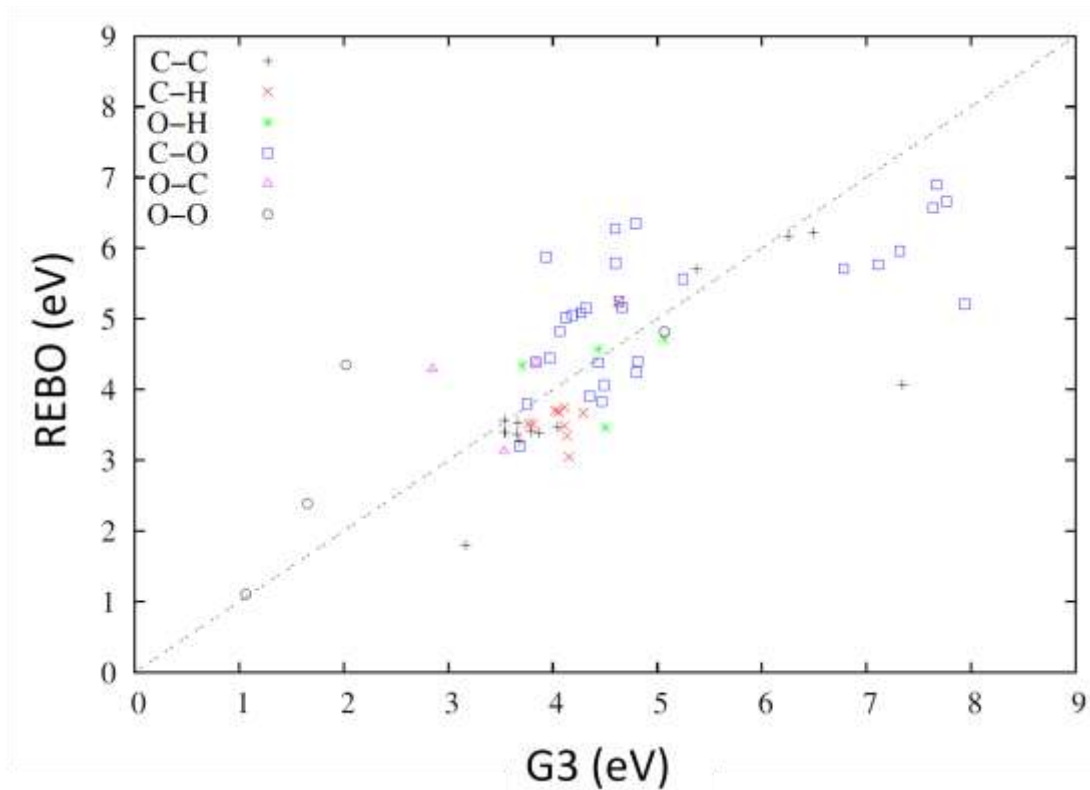


Figure 3-1. Dissociation energies of oxygen dataset calculate with G3 plotted as function of values calculated with REBO

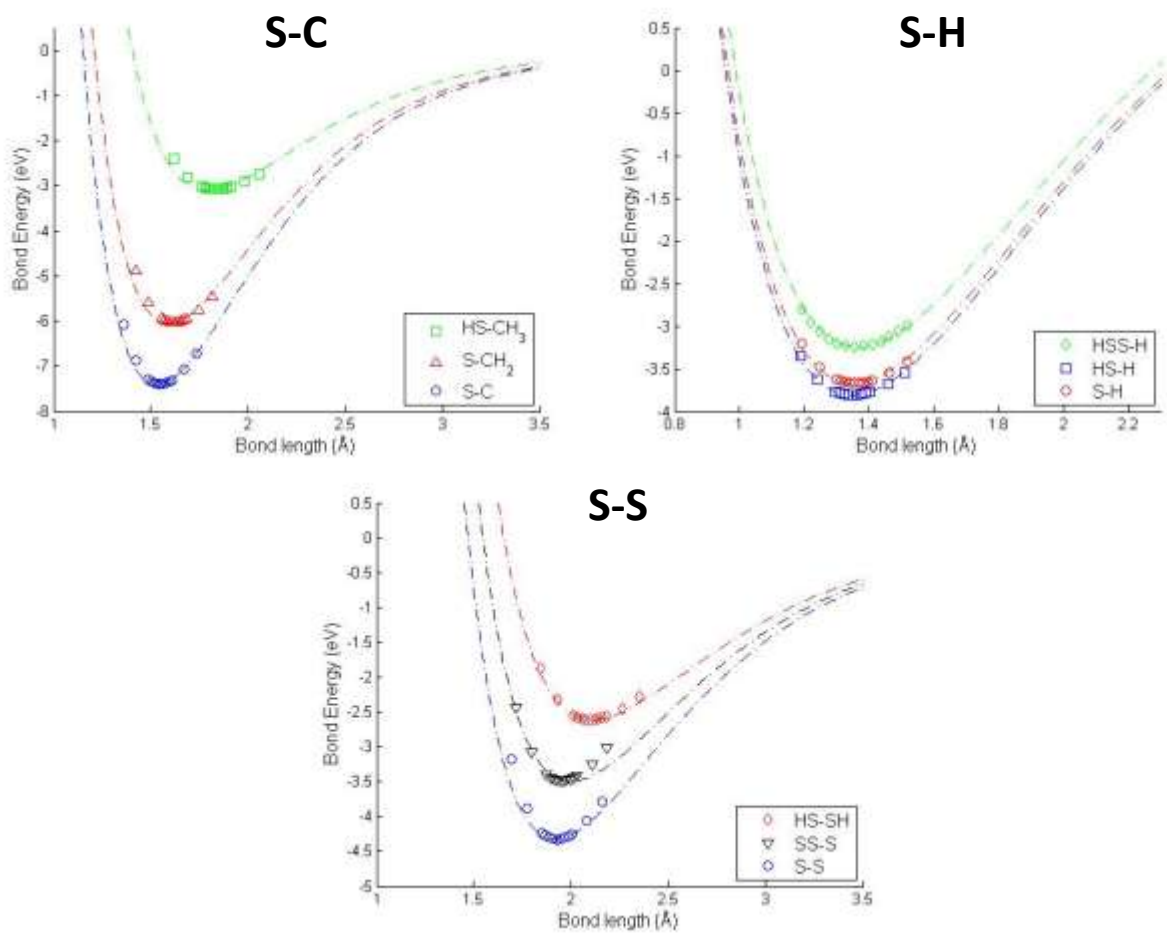


Figure 3-2. Bond stretching curves for *S*-*C*, *S*-*H* and *S*-*S* bonds.

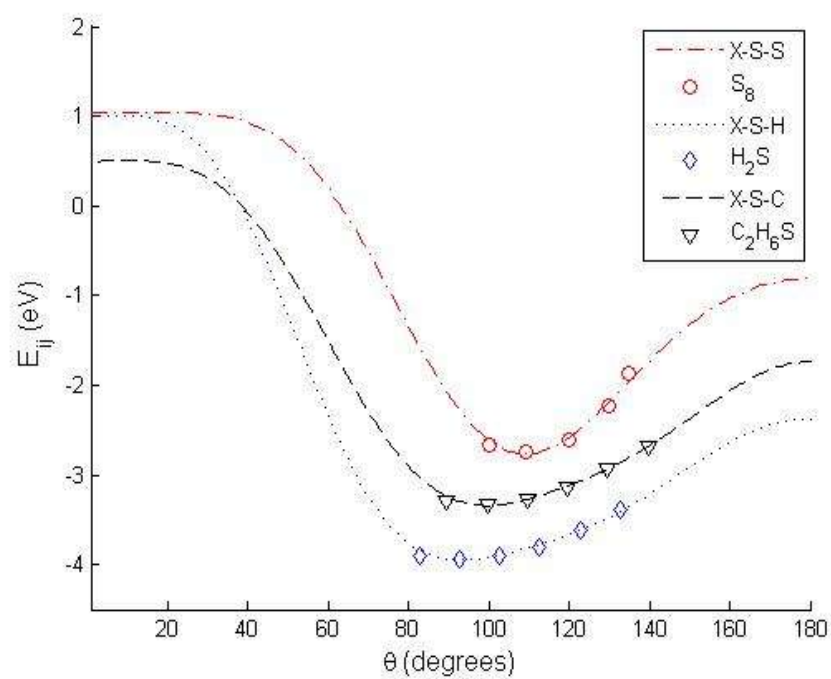


Figure 3-3. Bond energy as a function of bond angle for fitted $G(\theta)$ function

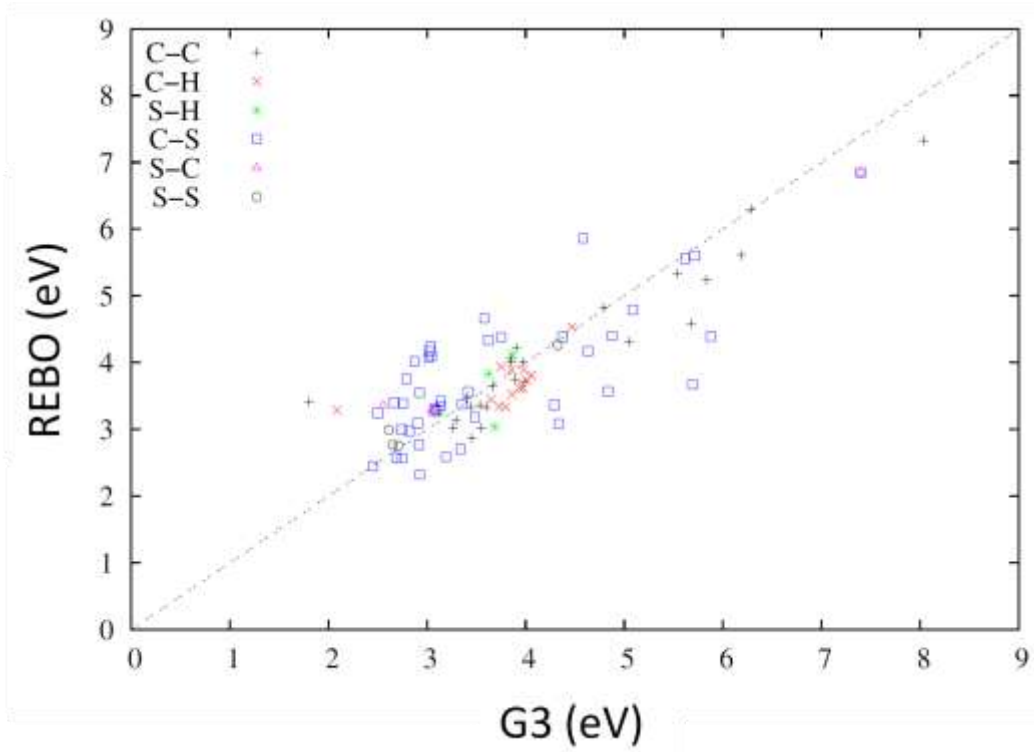


Figure 3-4. Dissociation energies of sulfur dataset calculate with G3 plotted as function of values calculated with REBO

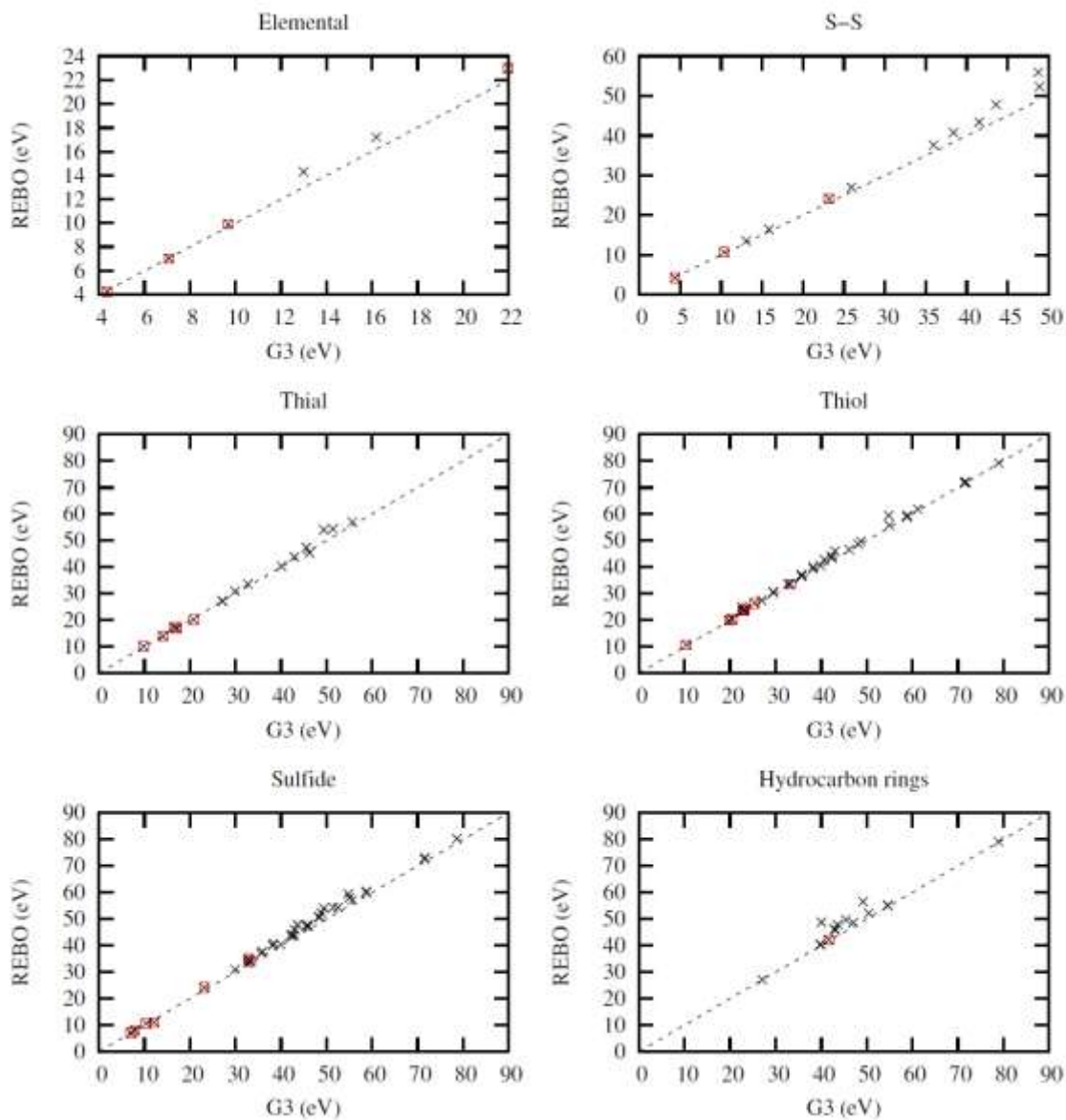


Figure 3-5. Atomization energies of test set of molecules, energies boxed in red are included in fitting database

CHAPTER 4 COMPARISON OF REBO AND DFT-MD DEPOSITION SIMULATIONS

4.1 CHF Deposition on Diamond

In order to better understand the complex processes that occur during the energetic fluorocarbon growth of diamond like carbon (DLC) films, a multilevel computational analysis is performed. The first involves MD simulation of 300 single trajectory depositions of CF_3 using with the second generation REBO potential³⁸. Further analysis was conducted by a colleague, Bryce Devine¹⁰⁶. For comparison, 10 complementary depositions are conducted with the linearly scaling DFT based MD method SIESTA¹⁰⁷. Based on the results of the MD simulations, reactions are further analyzed with hybrid DFT methods B3LYP¹⁰⁸, B98¹⁰⁹ and BMK¹¹⁰, and the multilevel G4MP2B3 method¹¹¹.

4.1.1 Methodology

Within the second generation REBO potential formalism electronic excitations and the charge of the atoms is not included. Consequently ions are not explicitly modeled. Rather carbon atoms with dangling bonds are represented by radicals. Therefore charge related effects, such as the deceleration of the deposited species due to charge accumulation in the substrate, are not accounted for.

For the empirical MD simulations, hydrogen terminated diamond (111) surfaces of 11520 atoms are used. PBC's are applied perpendicular to the surface. The temperature is controlled using the "heat bath method" where most of the substrate has a thermostat applied using the Langevin⁵¹ method, except for a small "active" cubic area of 128 atoms with a surface area of 100 \AA^2 , which is allowed to freely evolve. Molecules of randomly oriented CF_3 are deposited with kinetic energies of $50 eV$ on the active

region. Simulations are run for $20ps$ with a $0.2fs$ time step using the third order predictor corrector integrator^{49, 50}. The relatively small active region is used to allow for comparison to DFT-MD simulations with the SIESTA software¹⁰⁷.

For the DFT-MD simulations, a 10 \AA by 10 \AA by 13 \AA spurecell of 128 carbon atoms is used, as seen in Figure 4-1. Surfaces are hydrogen terminated and PBC's are applied in all three dimensions, leaving a 15 \AA vacuum between periodic slabs. Depositions of both CF_3 radicals and CF_3^+ cations are simulated. Temperatures are maintained at $300K$ with the Nose-Hoover method¹¹²⁻¹¹⁴. The Verlet algorithm is used as an integrator, and simulations are run for $2ps$ with a $0.1fs$ time step. This work was carried out by colleagues Bryce Devine and Inkook Jiang.

Higher level quantum chemical calculations are performed using the GASSIAN 03 software¹¹⁵. Further calculations using the hybrid methods are performed using a C_{22} cluster, Figure 4-1, which has been previously determined to be the minimum structure to accurately reproduce sp^3 hybridization¹¹⁶. This work was carried out by colleague Bryce Devine.

4.1.2 Results

Based on the MD simulations of 300 single trajectory depositions of CF_3 using the REBO potential, reactions are found to depend on the location of the impact and the orientation of the deposited molecule. Given the pyramidal structure of CF_3 , it can either land with carbon or fluorine participating in the initial impact. The simulations show that fragmentation of the CF_3 molecule is more likely if the fluorine atoms of the molecule initially impact the diamond surface, rather than the carbon atom.

The impact location is also found to affect the products formed during the deposition. In Figure 4-2, the three sites of the (111) diamond surface are shown. The top carbon atom is referred to as the atop site and is labeled (A), the recessed surface carbon is labeled (S) and the hollow site is labeled (H). A majority of deposited radicals (60%) interacted with the atop site, since it is the most exposed. The recessed site is more accessible than the hollow site, and is the primary interaction location of (28%) of the deposited radicals.

The atop site produced the most reactions; in particular, new products are formed 80% of the time when the incident radical impacts this site directly. Approximately half of these reactions involved the removal of a hydrogen atom from the surface, and 45% resulted in the CF_3 bonding to the surface. New products resulted in 39% of the depositions impacting the recessed carbon site (S), with 5.0% of the reactions leading to surface-bound CF_2 . The results of these depositions are summarized in Table 4-1.

Ten DFT-MD simulations are performed for each charge state, radical and cation, of the CF_3 molecule. The results of these depositions are summarized in Table 4-2. It can be seen that the CF_3 radical is more reactive according to DFT than second generation REBO potential, as a majority of the DFT-MD simulations result in reactions. Similar reactions are observed for the CF_3 radical and CF_3^+ cation, given that CF_2 is produced in 40% and 30% of the reactions for the radical and the cation respectively, in the DFT-MD simulations.

Reactions based on the CF_3 radical's interactions with a cluster of 22 carbon atoms are shown in Table 4-3. The BMK hybrid method is used for the comparison of first principles methods and the second generation REBO potential. The second

generation REBO potential does surprising well, for an empirical potential, at predicting the reaction enthalpies involving the radical CF_3 radical.

In order to explore the removal of H from the surface, the bonding of CF_2 and the formation of HF (reaction (3) Table 4-3) a transition state calculation is performed. The synchronous transit quasi Newton-Raphson algorithm¹¹⁷ is used with the B3LYP/6-31G(d) method to find the transition state shown in Figure 4-3. Various initial geometries are used as input structures; however, the same saddle point is found from all starting orientations. Based on the saddle point energy and the separate reactants the activation enthalpy is found to be $7.2eV$.

4.1.3 Discussion

The quantum chemical simulations show the differences between the interactions of the CF_3 radical and the cation. It can be seen from reaction (7) in Table 4-3 that the most energetically favorable reaction of the CF_3^+ cation is to remove a hydrogen from the surface, and produce CF_2 and HF . While reaction (3) shows that the second most energetically favorable reaction of the radical is to bond to the diamond substrate and produce atomic hydrogen. It can also be seen in Table 4-3 that all reactions that result in film growth involving the cation are energetically unfavorable, reaction (9) by $4.5eV$ and reaction (10) by $10eV$. Conversely, radical interactions that form complexes, as seen in reaction (1-3), are energetically favorable.

From the quantum chemical data it can be seen that formation of HF may be one of the drivers of the bonding of CF_3 to the substrate. However, HF is not seen in the second generation REBO results, due to the limit interaction range of the potential. The R^{max} and R^{min} cutoff values for the $H-F$ interactions are 1.8\AA and 2.2\AA , where the

transition state in Figure 4-3 is found to have an interaction length of 1.78Å. This accounts for the lack of *HF* during the MD depositions (see Table 4-1). While second generation REBO potential reasonably predicts the ground state energetics (Table 4-1), the short range of the potential and the lack of charge are the main draw backs.

During the DFT-MD simulations, Mullikin population analysis shows that the deposited CF_3^+ oxidizes the carbon substrate producing a radical molecule and a positively charged site on the substrate. This is in part due to an over estimate of the oxidation potential of CF_3^+ by SIESTS, Table 4-3 reaction (14). This leads to similar results between the second generation REBO and the DFT-MD simulations, since both are essentially radical molecules interacting with a surface.

However, the DFT-MD results using the SIESTA software (Table 4-2) show that reactions occur with 100% of the radicals and 80% of the cations, while the second generation REBO potential predicted that 60% of deposited species would react with the surface. While the second generation REBO potential did not accurately capture the formation of *HF* during the deposition reactions, the bond of a CF_2 to the diamond surface and the creation of atom *H* and *F* are found to be one the possible reactions. Therefore, the second generation REBO potential is able to identify the general form of the most pertinent reaction for the growth of DLC films. While, limit by short cutoff values and the lack of charge states the second generation REBO potential offers a computationally efficient means to guide further study using more accurate quantum chemical calculations.

4.2 Hydrocarbon Deposition on Polystyrene

4.2.1 Methodology

To isolate the most frequently formed products on the surface of polystyrene due to hyperthermal hydro-carbon modification, a series of MD simulations are performed using the second generation REBO potential depositing hydrocarbon molecules with kinetic energies of 4eV and 10eV on β " syndiotactic polystyrene, Figure 4-4. In each simulation, particles are randomly oriented and positioned within the surface plane. Depositions are conducted continuously with impacts every 1.5ps . Each beam contains 300 hundred particles corresponding to fluencies of $97.6 \times 10^{18} \text{ ions/cm}^2$. Following continuous deposition, the systems are evolved for an additional 25ps , until the fluctuations in the potential energy are less than 0.0033 eV/atom . The final surfaces are analyzed to determine the products of the deposition process.

Frequently observed products ($> 5\%$) are subsequently examined using higher order quantum chemical methods with molecules interacting with a PS monomer, Table 4-4. Minimum energy geometries, transition states and intermediates are found with the B3LYP¹⁰⁸ hybrid functional and the 6-31G(d,p)¹¹⁸ basis set using the GAUSSIAN 03 software package¹¹⁵. Frequency analysis is performed to confirm transition states and minima. Intrinsic reaction coordinate (IRC)¹¹⁹ calculations are performed to confirm that an identified transition state corresponds to the reactants and products of interest. The IRC calculations use the transition state as an input, and follow the minimum in the potential surface along the saddle by performing geometry optimizations of structures generated at symmetric steps along the negative frequency away from the transition state.

While the B3LYP method is known to produce accurate frequency spectra the magnitude of the energy barriers is less accurate. Therefore, to determine more precisely the energy barriers for the reaction pathways considered, single point couple cluster singles and doubles (CCSD)^{120, 121} calculations are performed on structures optimized at the B3LYP/6-31G(d,p) level. These calculations are performed by Michelle Morton and Joseph Barron of Department of Chemistry, Georgia Southwestern State University under the guidance of Nedialka Jordanova¹²².

4.2.2 Results

For the 300 *H* atoms deposited at 10eV: 9% bond to the backbone carbons, 14.7% remain in atomic form and 24% bond to the styrene carbons, Table 4-4. In contrast, for the *H* atoms deposited at 4eV, 75% percent did not penetrate the substrate. Of the 25% that did penetrate the substrate, a majority or 14% bonded to the styrene carbons, while only 1% bonded to the backbone.

The reaction profile determined using B3LYP and CCSD methods is shown in Figure 4-6. The energies for this profile are in Table 4-5. When H^+ is in the vicinity of the PS monomer, the H^+ attaches directly to one of the carbon atoms of the styrene ring forming a positively charged non-aromatic product. The product can isomerize to by a migration of the protons to another carbon atom via triangular shaped transition state, see Figure 4-6.

MD simulations of C_2H molecule deposited onto a PS surface result in a majority of the deposited molecules bonding to the C2, C3 and C4 positions of the styrene ring. In particular, 17% and 25% of the deposited molecules, at 4eV and 10eV respectively bonded to these carbons, Table 4-4. The primary product formed during the C_2H

deposition is the bonding of the C_2H to a styrene carbon, while leaving the carbon hydrogen bond intact, Table 4-4. The addition of C_2H to a C2, C3 or C4 carbon occurs during 68% and 55% of the bonding reactions of C_2H with PS, for 4eV and 10eV deposition energies respectively. Therefore the reaction mechanisms of the addition of C_2H to the C2, C3 or C4 carbons of the PS monomer are further studied with quantum chemical methods.

Optimized configurations and transition states calculated using B3LYP for the C_2H^+ cation are shown in Figure 4-7. The reactions show that the interaction leads to various product minima, where the C_2H^+ particle is attached to one of the styrene carbon atoms. The minima are connected via transition states corresponding to bridged structures where the C_2H^+ particle is interacting with two neighboring carbon atoms of the styrene ring. The reactant species and each minimum are directly connected since the bonding between the C_2H^+ and the ring is shown to be barrier less, Table 4-6. The reaction profile shows the single point CCSD calculations as well. The latter are in accordance with the B3LYP calculations and give consistent relative energies between the minima and transition states.

As with the deposition of C_2H , the MD simulations using the second generation REBO potential of CH_2 show the C2, C3 and C4 position on the styrene ring to be more probable than the C5 and C6 positions, as indicated in Table 4-4. Further, the products are a combination of three reactions. The first reaction (i) is the attachment of the CH_2 particle on one of the styrene ring carbon atoms and the breaking of the aromaticity of the ring. The second is the attachment of the CH_2 particle to one of the styrene ring carbon atoms and subsequent transfer of the hydrogen atom from the styrene ring to

the CH_2 particle to form a methyl group, restoring the aromatic structure of the ring is further identified as reaction (ii). And the third reaction (iii) is the bonding of the CH_2 to two of the styrene ring carbons creating a non aromatic ring.

The interaction of the CH_2 radical with the C2, C3 and C4 position on the styrene ring are investigated by quantum chemical calculations. Considering the CH_2 radical ground state is a triplet electronic configuration, both the triplet and singlet states are evaluated. For the triplet configuration the first two bonding configurations, (i) and (ii), are found to be stable. The two states are considered within one reaction process, in Figure 4-8. The reaction pathways resulting from the CH_2 triplet radical deposition and the corresponding barriers are given in Table 4-7.

While the initial electron configuration of the CH_2 radical is a triplet, the ground state of the methyl added to the styrene ring is a singlet. In order to clarify the reaction pathway, of the singlet state is considered separately from the triplet state, see Figure 4-9. It is determined that a concerted mechanism is more preferable for the formation of a methyl product on the C3, C4, and C5 positions. The energy barriers for the reaction with the C4 position using the B3LYP and CCSD methods are summarized in Table 4-8.

4.2.3 Discussion

MD simulations of hydrogen deposited on a PS surface resulted in the non-preferential bond of atomic H to the ring of PS. However, subtle differences are seen in the quantum chemical calculations, Table 4-5. According to these results, the ortho- and para-products are more stable than the meta ones. The para-product is 1.12 kcal/mol more stable than the C6 ortho-product and 1.19 kcal/mol more stable than the C2 orthoproduct. Relative energies of the C2 and C6 ortho sites show the C6 to be

more stable than C2 site, which is counterintuitive considering orientation of the isopropyl group and its steric effects on the styrene ring. The optimized geometry showed that the isopropyl group rotated significantly to accommodate the incoming H particle only when the proton is attaching to the C6 position. The difference between the transition barriers on the left-hand and right-hand side of the reaction profile (Figure 4-6) are attributed to the presence of the isopropyl group and its rotation during the reaction. The strong binding of the H atom to the styrene ring and relatively small differences between the sites, supports the MD findings of non-preferential bonding of H to the aromatic carbons.

The C_2H ion showed similar reactivity with PS. The MD simulations of C_2H being deposited at $4eV$ showed C2, C3, and C4 position on the ring to be likely binding sites. According to the quantum chemical calculations, Figure 4-7, the most energetically favorable binding site is the para-position (C4), Table 4-6. As with the H atom the relative energies of all the bonding sites are within $10kcal/mol$ of each other, leading to an assumption of non-preferential bonding to the styrene ring. This is supported by the $10eV$ depositions, which show a more even distribution of bonding to the styrene ring. However, the lack of periodicity of the PS monomer used in gas phase calculations must also be considered. In the case of the MD simulations the movement of the backbone carbons is restricted. This leads to the C6 being less accessible, which explains the low probability of this bonding site in the MD simulations for C_2H .

For CH_2 interacting with PS three possible bonds are found to be likely according to the MD simulations. These are the direct bonding to the styrene ring, the formation of a methyl group and the incorporation of the CH_2 into the ring. According to quantum

chemical calculations the direct bonding to the ring is found to be stable for the triplet electronic configuration. On the other hand, the formation of a methyl group is found to be stable for both the triplet and singlet electronic configurations.

4.3 Summary

Based on multilevel simulation of the growth mechanism of DLC films of fluorocarbons the production of HF is found to be one of the key drivers. While HF formation is not directly observed during the simulations performed with the second generation REBO potential the relevant process of CF_2 bonding the diamond substrate is identified.

From the simulations of H , C_2H and CH_2 interactions with PS, non-preferential bonding to the styrene ring carbons is found for H , C_2H and CH_2 . However, MD simulations of depositions show that the steric hindrance of the backbone limits the bonding to the C6 position. For the PS and CH_2 interactions, the charge and spin state are found to significantly affect the bonding.

Table 4-1. Reaction predicted by classical MD simulations using the REBO potential

Reaction	Probability (%)	Reaction Site
$\cdot CF_3 + C_{Dia} \rightarrow \cdot CF_3 + C_{Dia} (No Rx)$	42.0	A,H,S
$\cdot CF_3 + C_{Dia} \rightarrow HCF_3 + C_{Dia}$	13.7	A
$\cdot CF_3 + C_{Dia} \rightarrow CF_3C_{Dia} + H$	21.7	A
$CF_3 + C_{Dia} \rightarrow CF_3 + H + C_{Dia}$	10.0	A
$\cdot CF_3 + C_{Dia} \rightarrow CF_2C_{Dia} + H + F$	5.0	A,S
$\cdot CF_3 + C_{Dia} \rightarrow CF_2 + C_{Dia} + F + H$	4.0	A,S
$\cdot CF_3 + C_{Dia} \rightarrow CF_2 + C_{Dia} + F$	2.0	S
$\cdot CF_3 + C_{Dia} \rightarrow FC_{Dia} + CF_2 + H$	1.7	S

Table 4-2. DFT-MD predicted reactions

CF_3 Radical Reactions	Probability (%)	CF_3^+ Reactions	Probability (%)
$\cdot CF_3 + C_{Dia} \rightarrow \cdot CF_3 + C_{Dia} (No Rx)$	0.0	$CF_3^+ + C_{Dia} \rightarrow CF_3 + C_{Dia}$	20
$\cdot CF_3 + C_{Dia} \rightarrow \cdot CF_3 + H + C_{Dia}$	10	$CF_3^+ + C_{Dia} \rightarrow CF_3 + H + C_{Dia}$	10
$\cdot CF_3 + C_{Dia} \rightarrow HF + F + CFC_{Dia}$	30	$CF_3^+ + C_{Dia} \rightarrow CF_3 + 2H + C_{Dia}$	10
$\cdot CF_3 + C_{Dia} \rightarrow HCF_2 + HF + C_{Dia}$	10	$CF_3^+ + C_{Dia} \rightarrow CF_2 + 2H + F + C_{Dia}$	10
$\cdot CF_3 + C_{Dia} \rightarrow CF_2 + HF + C_{Dia}$	20	$CF_3^+ + C_{Dia} \rightarrow CF_2 + H + F + C_{Dia}$	10
$\cdot CF_3 + C_{Dia} \rightarrow CF_2 + H + F + C_{Dia}$	20	$CF_3^+ + C_{Dia} \rightarrow CF_2 + HF + C_{Dia}$	10
$\cdot CF_3 + C_{Dia} \rightarrow C_2F_2 + H + F + C_{Dia}$	10	$CF_3^+ + C_{Dia} \rightarrow 2HF + H + CFC_{Dia}$	10
		$CF_3^+ + C_{Dia} \rightarrow 2HF + CF + C_{Dia}$	10
		$CF_3^+ + C_{Dia} \rightarrow 2HF + F + H + CC_{Dia}$	10

Table 4-3. Reaction enthalpies calculated with the 22 atom carbon cluster

Reaction	REBO	SIESTA	a BMK	b ZPE
1. $\cdot CF_3 + C_{22} \rightarrow HCF_3 + \cdot C_{22}$	-0.28	-0.57	-0.26	-0.20
2. $\cdot CF_3 + C_{22} \rightarrow CF_3C_{22} + H$	0.97	1.03	0.92	0.69
3. $\cdot CF_3 + C_{22} \rightarrow CF_2C_{22} + HF$	0.11	0.05	0.28	0.11
4. $\cdot CF_3 + C_{22} \rightarrow \cdot CF_2 + F + H + \cdot C_{22}$	8.41	8.54	8.43	7.98
5. $\cdot CF_3 + C_{22} \rightarrow \cdot CF_2 + HF + \cdot C_{22}$	2.58	2.26	2.60	2.41
6. $\cdot CF_3 + C_{22} \rightarrow \cdot CF_3 + H + \cdot C_{22}$	4.58	4.17	4.61	4.38
7. $CF_3^+ + C_{22} \rightarrow CF_2 + HF + C_{22}^+$	--	-1.44	-0.77	-1.05
8. $CF_3^+ + C_{22} \rightarrow \cdot CF_2^+ + HF + \cdot C_{22}$	--	4.86	4.97	4.83
9. $CF_3^+ + C_{22} \rightarrow CF_3C_{22} + H^+$	--	4.92	5.54	5.31
10. $CF_3^+ + C_{22} \rightarrow CF_2C_{22} + H^+ + F$	--	10.3	10.7	10.3
11. $CF_3^+ + C_{22} \rightarrow CF_3 + \cdot H + C_{22}^+$	--	0.57	1.25	0.92
14. $CF_3^+ + C_{22} \rightarrow \cdot CF_3 + C_{22}^+$	--	-1.53	0.03	-0.30
Mean Absolute Error (eV)	0.05	0.47	--	--

Table 4-4. MD results of radicals deposited on PS

Ion:	<i>H</i>		<i>CH₂</i>		<i>C₂H</i>	
Energy	4eV	10eV	4eV	10eV	4eV	10eV
In substrate	24.67	48.33	39.67	70.89	53.00	74.67
Bonded	15.00	33.67	24.00	58.33	30.67	58.33
Bonded to ring	12.67	24.67	17.50	42.00	19.00	35.50
C(2)	2.67	6.67	4.17	12.00	4.00	7.50
C(3)	2.67	3.67	5.67	9.17	5.33	7.83
C(4)	1.33	5.00	5.00	10.50	7.33	9.67
C(5)	2.00	4.67	2.67	6.67	2.00	7.33
C(6)	4.00	4.67	0.00	3.67	0.33	3.17

Table 4-5. Hydrogen interaction with PS monomer

	B3LYP/6-31G(d,p) kcal/mol	CCSD/6-31G(d,p) kcal/mol		B3LYP/6-31G(d,p) kcal/mol	CCSD/6-31G(d,p) kcal/mol
A	15.46	14.17	A''	15.30	14.32
B	15.95	15.43	B''	16.09	15.75
C	11.47	11.08	C''	12.17	11.92
D	11.50	11.25	D''	11.87	11.45

Table 4-6. Reaction barriers for the interaction of C₂H⁺ with the polystyrene monomer.

	B3LYP/6-31G(d,p) kcal/mol	CCSD/6-31G(d,p) kcal/mol		B3LYP/6-31G(d,p) kcal/mol	CCSD/6-31G(d,p) kcal/mol
A	12.46	14.16	A'	15.90	17.51
B	10.87	12.08	B'	11.49	13.06
C	11.13	12.56	C'	11.47	12.74
D	16.12	18.84	D'	16.63	18.56

Table 4-7. Reaction barriers for the interaction of CH₂ triplet radical with the polystyrene monomer C4 position.

	B3LYP/6-31G(d,p) kcal/mol	CCSD/6-31G(d,p) kcal/mol
A	4.84	10.52
B	26.69	29.9
C	40.83	44.19
D	40.11	40.99

Table 4-8. Reaction barriers for the interaction of CH₂ singlet radical with the polystyrene monomer C4 position

	B3LYP/6-31G(d,p) kcal/mol	CCSD/6-31G(d,p) kcal/mol
A	76.41	78.09
B	61.13	70.77
C	103.14	108.09

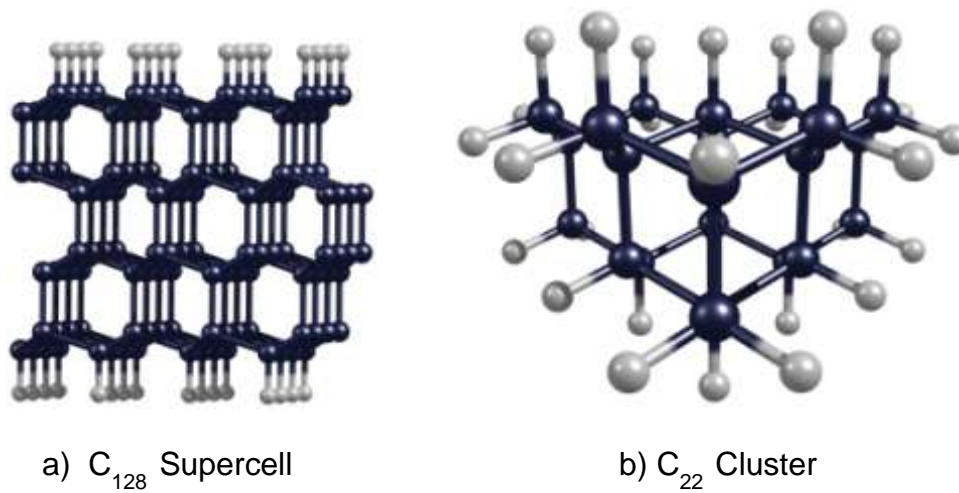


Figure 4-1. Systems used for reaction enthalpies: A) periodic slab of 128 atoms, B) carbon cluster of 22 atoms.



Figure 4-2. Site on diamond (111) surface

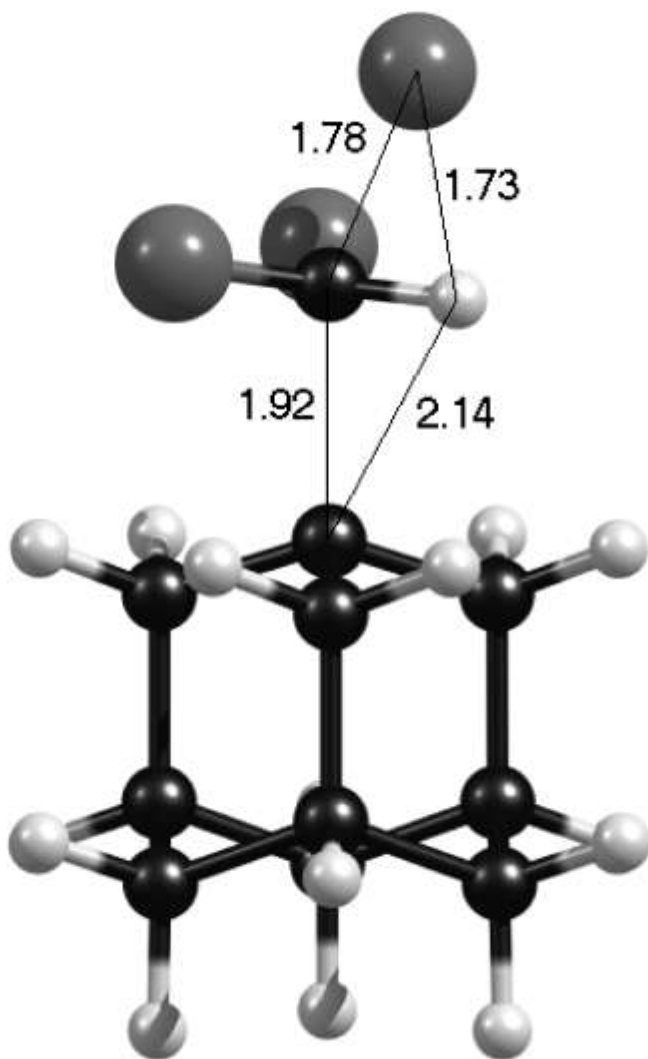


Figure 4-3. Transition state geometry of CF_2 radical on adamantane surface to produce CF_2 on the surface and an HF molecule

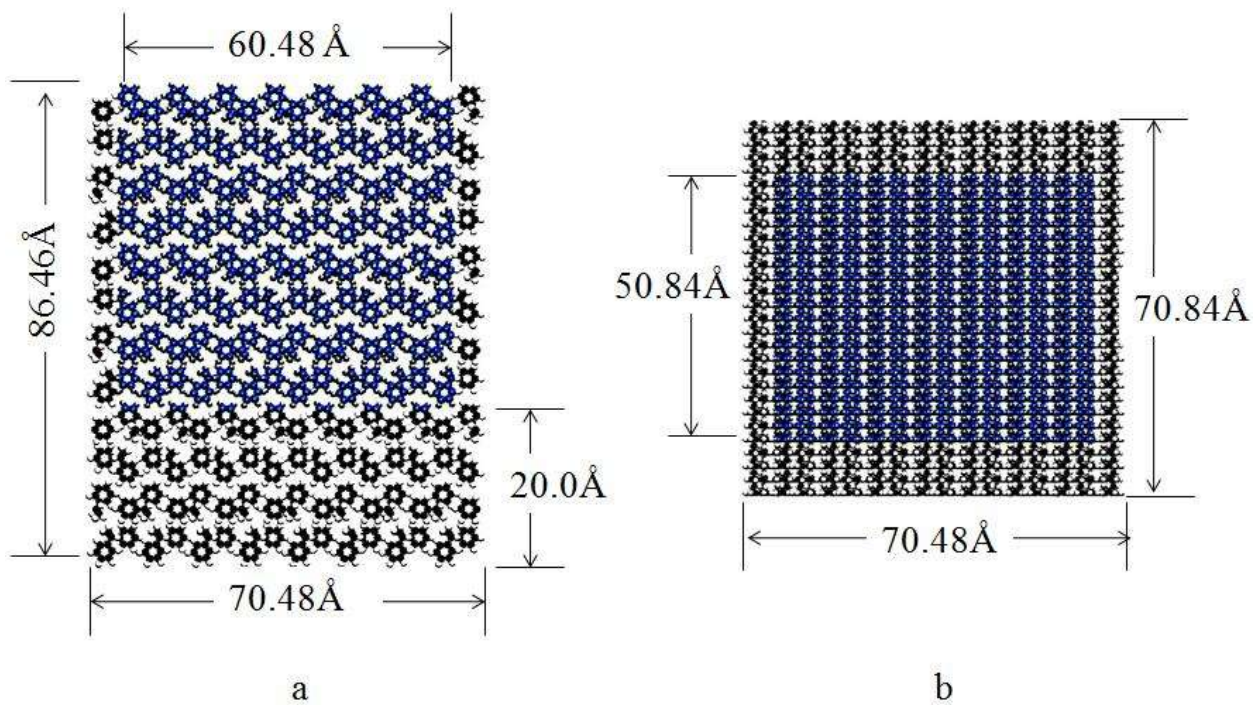


Figure 4-4. Crystalline polystyrene where the black and white atoms are thermostat region, and the blue and gray atoms are active, a) is a side view along the back bone, b) is a top view

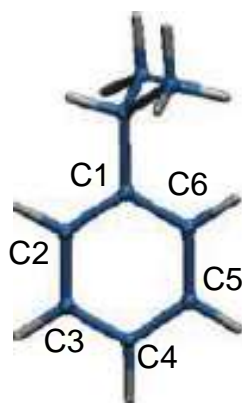


Figure 4-5. PS monomers where carbon is the darker (blue) atoms and hydrogen is the lighter (gray) atoms

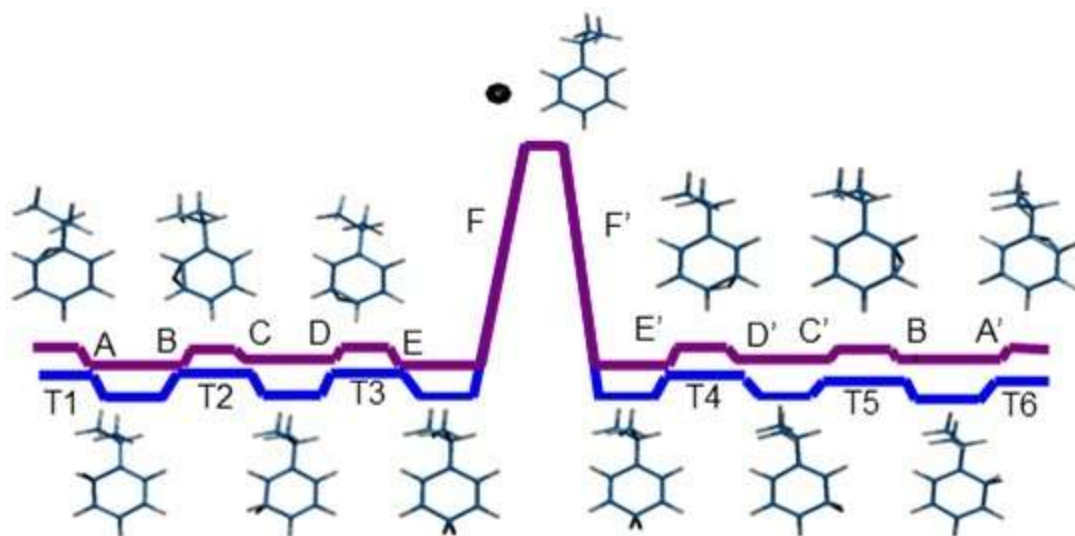


Figure 4-6. Reaction profile of the interaction of H^+ with the polystyrene monomer. C1 – (C6-C1) barrier not available because the product where the H atom is attached to the C1 carbon atom could not be localized due to steric hindrance of the C1 carbon atom by the side chain. The barriers are presented in Table 4-4

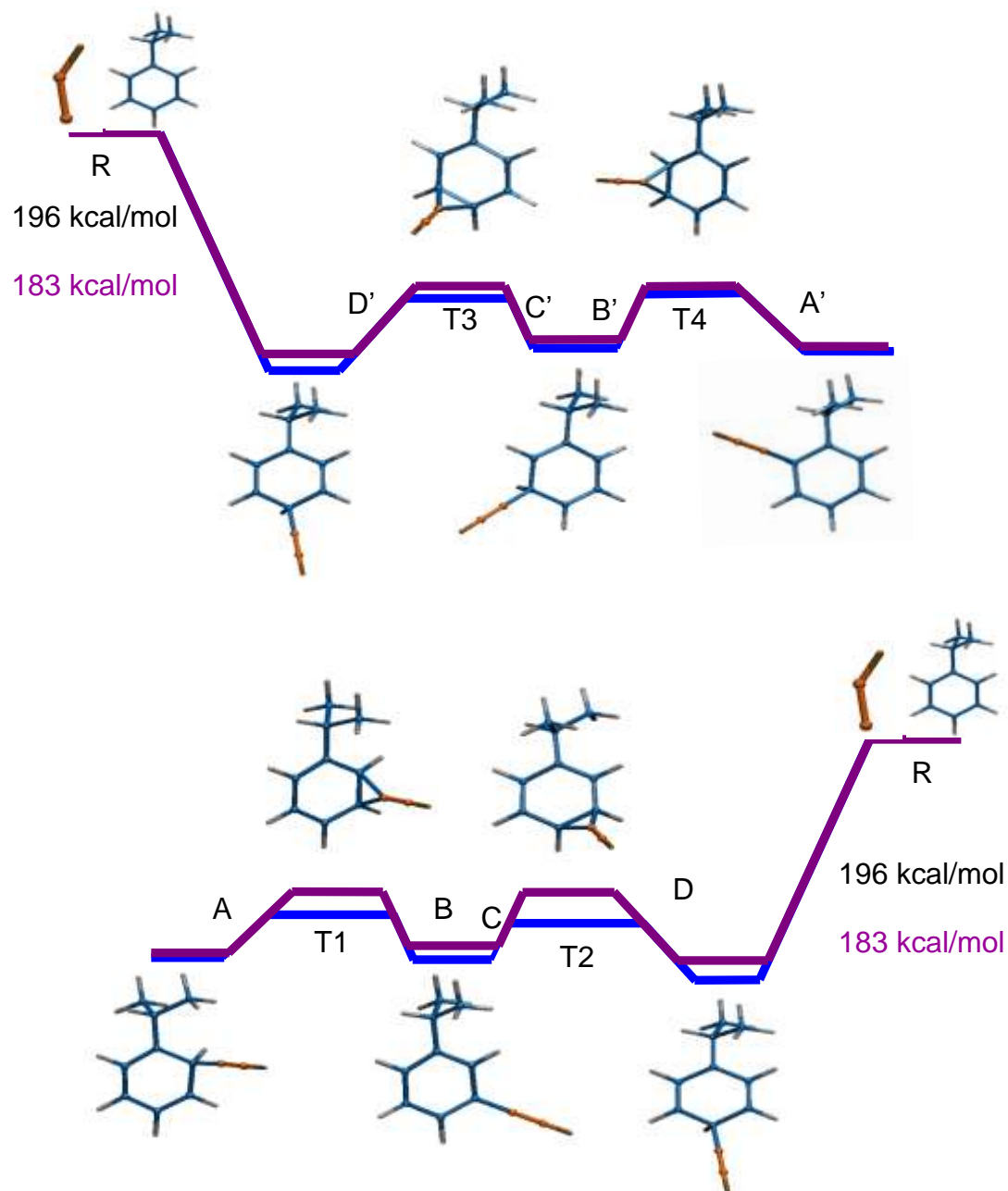


Figure 4-7. Reaction profile of the interaction of C_2H^+ with the polystyrene monomer. The barriers are presented in Table 4-6

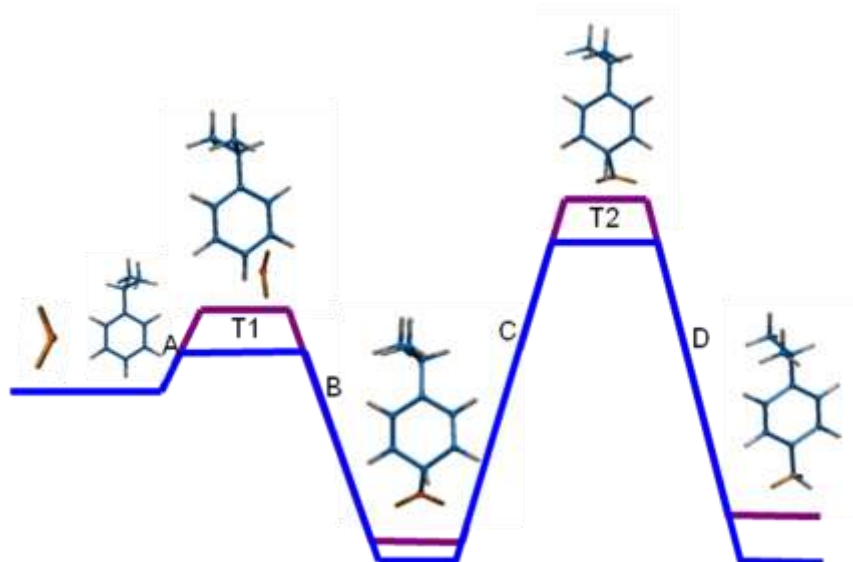


Figure 4-8. Reaction pathways for CH_2 triplet radical on C4 the barriers are presented in Table 4-7.

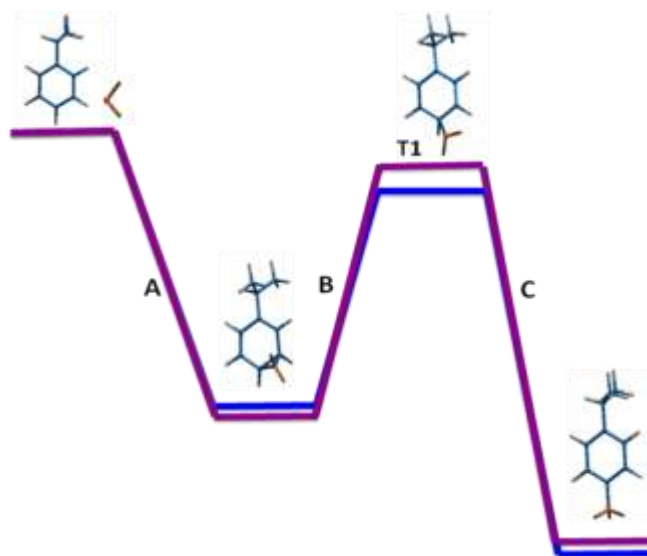


Figure 4-9. Reaction pathway of CH_2 singlet radical on C4, the barriers are presented in Table 4-8.

CHAPTER 5 SURFACE POLYMERIZATION ION BEAM ASSISTED DEPOSITION

Thiophene based molecules possess excellent properties for electronics. They are being used for photovoltaics¹²³, field effect transistors^{124, 125}, biological tags⁹⁷ and light emitting diodes¹²⁶. While thiophene oligomers and polymers have desirable electrical properties for these applications, controlling their morphology under industrial processing conditions remains a challenge¹²⁴.

Various possible alternatives to wet chemical processing for low cost production of organic electronics are illustrated in a recent Nature article¹²⁷. These include the thermal transfer of organic molecules, direct patterning of organic electronic devices, and variations on chemical vapor deposition (CVD). One attractive feature of vapor phase deposition methods is that they are a 'dry process,' which lack the use of a chemical solvent that could have detrimental effects on device performance¹⁹. A current issue with vapor phase deposition is morphology control of thicker films consisting of species with sufficient conjugation lengths, such as sexithiophene¹²⁸.

Some success in controlling morphology through the use of energetic particles has been achieved. Podesta et al. used supersonic molecular beam deposition to create ordered layered structures of α -quaterthiophene¹²⁹. However, previous efforts to use plasmas to polymerize films for organic electronics have met with little success. For instance, Paterno et al. investigated plasma polymerization of aniline via Ar , NH_2 , and I_2 ¹³⁰. While higher molecular weight species were produced, they did not consist of conjugated polyaniline, and had negligible electric conductivity. Thiophene based antistatic coatings were created by plasma polymerization¹³¹. However, conductivities in these films were also very low ($10^{-6} S/cm$). Poor conductivity is attributed to

thiophene fragmentation. Later the same group found that adding substitutional groups onto the ring reduced the fragmentation of the thiophene rings¹³².

Luke Hanley's group at the University of Illinois at Chicago has developed a novel method of producing oligothiophene thin films. This process utilizes the co-deposition of thermal neutrals and hyperthermal ions to induce polymerization of the thin film, and is referred to as surface polymerization ion assisted deposition (SPIAD)³⁰⁻³³. In particular, 100eV thiophene ions and thermal terthiophene (3T) neutrals are found to produce films consisting of polymerized oligomers, when deposited with a ratio of 1:100. Ion beams used in the SPIAD process consist of roughly 65% intact thiophene ions, as well as C_3H_3 , CHS and C_2H_2S . Ion currents of $2 - 8 \mu A/cm^2$ and neutral fluxes of $5 \times 10^{15} \text{ molecules/s} \cdot \text{cm}^2$ are used. Deposition times are 10min, resulting in fluences of $3 \times 10^{18} \text{ neutrals/cm}^2$ and $0.7 - 3 \times 10^{16} \text{ ions/cm}^2$.

The higher molecular weight species created during this process improve the stability and optical properties of the film. The photolumence spectra of a pure 3T film is compared to films created using the SPIAD process in Figure 5-1. A red shift in the spectra can be seen for SPIAD films produced with 100eV thiophene. This red shift is attributed to the presences of higher molecular weight species, which have a reduced gap due to an increase in conjugation length¹³³. These higher molecular species are seen in the mass spectra in Figure 5-2. As with other energetic particle surface interactions the polymerization mechanism could not be determined experimentally.

The photolumences data confirms the existence of conjugated thiophene oligomers in the SPIAD deposited films. However, during the mass spectra analysis large amounts of fragmentation occurs during laser abolition, making the exact nature of

the molecules difficult to deduce. In the mass spectra the species found include $[3T]CH^+$, $[3T]S^+$, $[3T]T^+$, $[3T]T_2^+$, $[3T]_2^+$, $[3T]_2CH_2^+$, $[3T]_2TC_3H_3^+$ and $[3T]_2T_2CSH^+$. However whether these molecules are conjugated or linear fragments could not be inferred from the data.

Many polymerization methods have been proposed to explain the SPIAD process¹³⁴. The polymerization process is characterized by initiation, propagation and termination. First, cation-induced polymerization of the neutrals was proposed; however, the incorporation of the thiophene molecule itself into the molecular structure suggests that it is directly involved in the process. If the kinetic energy of the hyperthermal ion is the initiator, then further reactions need to occur between the deposited molecule and the incident particle for the polymerization to take place. Otherwise, hyperthermal argon should induce polymerization as well. Given this information, thiophene may act as both an initiator and as a reactant in the polymerization process.

Another possible mechanism is reactions that may occur due to the presence of dissociated species in the system. During hyperthermal interactions with a surface, the ablation process produces protons as the polymer is oxidized. These loose protons have been proposed to also be involved in the polymerization process. Protons created during the dissociation of polymeric materials have enough kinetic energy transferred to them to allow them to leave the surface. This kinetic energy can be absorbed by the surrounding molecules, and it can cause further fragmentation or oxidation leading to further reactions within the $3T$ film. Furthermore, the reactivity of the proton itself could be involved in the polymerization of the $3T$ molecule.

5.1 Methodology

Giving the complex nature of the SPIAD process MD simulations are conducted of hyperthermal argon and thiophene interactions with a $3T$ oligomer surface. The simulations are conducted using the newly parameterized second generation REBO potential for hydrogen, carbon and sulfur. Ar is included via the LJ component of the potential only, as it is not chemically reactive. As mentioned previously, ions are not explicitly accounted for within the REBO potential formalism.

An initial thin film of $3T$ is constructed by periodic replications of crystalline α -terthiophene¹³⁵, as illustrated in Figure 5-3. Films are created in a $5nm \times 5nm$ simulation cell with periodic boundaries perpendicular to the plane of the film. Films are approximately $4nm$ thick. The substrate is represented by a layer of diamond one unit cell thick, which is hydrogen terminated to limit any substrate oligomer chemical interactions. The bottommost atomic layer of the diamond is held rigid to prevent any rippling of the substrate. Thermostats are applied to the rest of the hydrogen terminated diamond using the Langevin method⁵¹ throughout the simulation.

Parallel and perpendicular orientations of the terthiophene backbone to the substrate are considered, Figure 5-4. In particular, films are generated with the a -axis and the c -axis normal to the substrate surface. The orientation of $3T$ to the substrate is unknown for SPIAD deposited films. However, both orientations are observed in other work^{125, 136}, and are found to be correlated with conductivity of the substrate and deposition conditions¹³⁷. Thermostats are applied to the $3T$ films to achieve a temperature of $300K$. Thermostats are then lifted, and the $3T$ film is allowed to freely evolve as “active atoms.” During the relaxation process the temperature of the $3T$ film

is seen to deviate from the initial value. Therefore, thermostats are reapplied and then lifted periodically until the desired temperature of 300K is achieved.

5.2 Single trajectory deposition

To investigate the differences between hyperthermal *Ar* and thiophene interactions with a 3T surface, single trajectory depositions are conducted at 50eV and 100eV. Experimental results show a difference in yield between 100eV *Ar* and thiophene, with thiophene producing higher molecular weight species, as indicated in Figure 5-2. Experimentally, thiophene ions and 3T neutrals are deposited simultaneously. However, given an ion flux of $5 \times 10^{13} \text{ ions/s} \cdot \text{cm}^2$ and a neutral flux of $5 \times 10^{15} \text{ molecules/s} \cdot \text{cm}^2$ for the 1:100 ion to neutral ratio³¹, and the surface of the simulation cell of 25 nm^2 this corresponds to 1 neutral per 0.8ms, and 1 ion per 80ms. Therefore, single trajectories of hyperthermal ions on 3T films should provide insight into the SPIAD process.

The simulations have a duration of 40ps which is found to be the necessary time for changes in hybridization to be stabilized. The molecular mass distribution of the resulting films are analyzed by grouping carbon and sulfur atoms within the minimum REBO potential cutoff R^{min} . Molecules with a center of mass greater than 1nm from the initial height of the 3T surface are considered to be removed into the vacuum. Initial concentrations of each molecular species are subtracted from the final concentrations to determine the yield of each species. Yields are given in molecules produced per deposited ion. The total yield for each species of a given mass is shown in red, while the yield that remains in the substrate is shown in blue.

5.2.1 Argon 100eV

In order to create a comparison to thiophene depositions, argon is deposited at the same energies on the same two surface orientations as thiophene. In Figure 5-5 the resulting molecular weight distribution for 20 deposition events of argon on the parallel surface configuration is shown. The primary products are atomic hydrogen, C_2H_2 , C_2H_1S , CH and $C_{12}H_9S_3$; similar molecules with a variance in hydrogen content are also found.

The main function of the deposited argon is found to be the fracturing of the thiophene rings of $3T$, which are predicted to be consumed at an average rate of 5.5 per event. By comparing the stoichiometry of produced molecules the probable reactions can be deduced. Considering the fact that the individual rings in $3T$ are thiophenes with variation in hydrogen only, C_4H_xS where $x=2$ or 3 , the products of C_2H_2 and C_2H_1S correspond to the removal of a thiophene ring from a $3T$ molecule. However the lack of $C_8H_5S_2$ shows a low probability that once fragmentation occurs, due to an impact, any semblance of the original molecule is likely not to be retained.

Beyond the destruction, the fusing of dissociated species is predicted to occur in the production of some higher molecular weight species, including $C_{25}H_xS_6$. While their yield is found to be low, their existence is investigated due to their relation to a possible polymerization processes. Upon visual analysis of the process, it is found that the creation of $C_{11}H_9S_3$ and $C_{25}H_xS_3$ are correlated. It is seen that as the deposited argon interacts with the stack of $3T$ molecules the removal a single carbon from a $3T$ occurs. This ejected carbon atom can be absorbed by an underlying thiophene molecule, which can further interact with another thiophene molecule to create a bridge between two $3T$

molecules, Figure 5-6. This seems to be a direct result of the narrow interaction range of a deposited atom, and the stacking of the $3T$ in the parallel configuration.

In the case of perpendicular alignment of $3T$ to the substrate, the deposition produces fewer low molecular weight species, as illustrated in Figure 5-7. The yield of species with masses less than that of the thiophene ($84AMU$) is found to decrease from 16.1 for the parallel orientation to 11.6 for the perpendicular orientation. Yields of the primary products of hydrogen, C_2H_2 and C_2H_1S are reduced by 20% to 30%. Furthermore, the formation of $C_{11}H_9S_3$ and $C_{25}H_xS_3$ is not predicted, due to the different configuration of the $3T$ with respect to the incident molecule.

5.2.2 Thiophene 100eV

Sets of 20 single trajectory depositions for each surface orientation are also conducted with thiophene at 100eV. The molecular analysis results are shown in Figure 5-5 and Figure 5-7. The primary low molecular weight products are found to be similar to that of the products of the argon depositions at the same energy. In particular, the dissociated thiophene rings are predicted to form H , C_2H_2 and C_2HS . Furthermore, the addition of a hydrogen to the $3T$ molecule to form $C_{12}H_9S_3$ is predicted.

For the thiophene interacting with the parallel configured $3T$ surface the main difference predicted relative to argon is the lack of dissociated higher molecular weight products. The yields of the primary products of atomic hydrogen, C_2H_2 and C_2HS are predicted to be similar to those produced by argon deposited at the same energy, as shown in Figure 5-5. The increased yield of atomic hydrogen and C_2H_2 is found to be about 5.0 and 4.7, respectively.

The yield of atomic hydrogen and C_2H_2 molecules that contain atoms from the deposited species is found to be about 1.0 for each molecule. A yield of 0.25 of beam molecules is predicted for the C_2HS molecules. The average molecular weight of a molecule in the beam is predicted to be around $73AMU$. Therefore the production of atomic hydrogen and C_2H_2 is related to the fragmentation of the deposited thiophene, while the production of C_2HS is mostly due the fragmentation of $3T$ molecules. This is supported by the relative yield of C_2HS being similar to that of the argon deposition simulations.

For the perpendicularly aligned $3T$, the trends predicted in the argon depositions are also predicted to occur for thiophene deposition. However, yields of the primary products of atomic hydrogen, C_2H_2 and C_2HS are predicted to decrease by about 50% for all molecules. The yield of molecules with a mass less than the mass of thiophene is predicted to drop as the oligomer orientations change. In particular, the yield varies from 18 for thiophene molecules depositions on the parallel $3T$ oligomers, to 9 for thiophene depositions on the perpendicular $3T$ oligomers. On the other hand, the number average molecular weight of the molecules containing deposited species is predicted to increase from $73AMU$ to $118AMU$. This indicates an increase in interaction between the deposited species and the modified $3T$ molecules. In fact, the ratio of molecules containing deposited particles in the film and in the vacuum is predicted to be 2:1 for the perpendicular case and 4:1 for the parallel case. This is due to the dissociation products, including the deposited species, being more confined due to the nature of the perpendicular film.

5.2.3 50eV Depositions

As discussed above, there is considerable fragmentation of the deposited thiophene during the 100eV depositions. Therefore, lower energy depositions are also considered. Incident energies are reduced to 50eV and the differences in the products is investigated. For the parallel and perpendicular 3T oligomer cases, there are more similarities in the products formed at this lower kinetic energy than there are at 100eV.

For the parallel configuration yields of over 1.0 are not predicted for argon deposition, as indicated in Figure 5-8. The products produced are consistent with the scission of carbon-carbon bonds, which is previously observed to be the primary result of argon deposition at 100eV. Carbon reduced products, including C_2H_2 , $C_7H_5S_2$ and $C_{11}H_7S_3$, and carbon increased products such as $C_{13}H_9S_3$ are produced with yields of less than 0.4. For the perpendicular configuration similar results are predicted, as illustrated in Figure 5-9, with carbon dissociation playing a primary roll.

For thiophene deposited at 50eV on the parallel configuration, there is a marked difference in products when compared to the argon modification at 50eV, Figure 5-8. First, the fragmentation of the thiophene molecule is predicted to occur even at half the experimental energy. The primary products are found to be C_2H_2 , atomic hydrogen, and C_2H_1S . These primary products are predicted to contain deposited species with respective molecular yields of 0.5, 0.6 and 0.3. Additional products containing deposited species vary in molecular weight from single carbon and sulfur atoms to modified 3T, with an average molecular weight of 67AMU. Similar to the 100eV depositions, the ratio of altered molecules that are sputtered to those that remain in the substrate is found to

be 3.5:1. Furthermore, the carbon reduced species are not found in the thiophene modified films. The primary modification of intact $3T$ is the addition of hydrogen.

For the $50eV$ argon modification of the perpendicular oriented $3T$ films, an increase in C_2H_2 production is predicted, when compared to the parallel case for the same energy. However, the other $3T$ fragments are seen to be better dispersed, as illustrated in Figure 5-8. This coincides with the deposited argon impacting the end of $3T$ molecule in the perpendicular case. This produces C_2H_2 rather than a more random distribution of carbon containing compounds, which is seen in the parallel case.

In the thiophene modified films with the $3T$ orientated perpendicular to the substrate a decrease in molecular yield is predicted when compared to the parallel case. However, similar products are seen to form, as shown in Figure 5-9. As with the parallel $3T$ oligomer case, a notable product is the bonding of hydrogen to a $3T$ oligomer. This could be the initialization of a polymerization process. Furthermore, argon bombardment at $50eV$ does not produce the same $C_{12}H_9S_3$ found during the thiophene depositions.

Visual analysis of the produced films indicates that no conjugated higher molecular weight species are formed during the simulation time of $40ps$. The majority of augmented products are predicted to be linear chains of varying molecular mass.

5.2.4 Discussion

While the direct observation of the formation of conjugated products is found to not occur during the simulations, numerous facets of the interaction of oligomer films with energetic particles are revealed. For all simulations the primary low molecular weight

product is predicted to be acetylene (C_2H_2), from fracture of a deposited thiophene or fractured $3T$ ring. Additionally, hydrogen and C_2HS are produced in most simulations.

At $100eV$, both thiophene and argon are predicted to produce similar products via the dissociation of $3T$ oligomers. Hydrogen, C_2H_2 and C_2HS are produced in the most abundant quantities for both $3T$ orientations. Furthermore, $C_{12}H_9S_3$ or $[3T]H$ is also found to be a probable product of bombardment. Upon visual inspection, $[3T]H$ is seen to result from a fractured $[3T]$ bonding to an extra hydrogen from the environment, see Figure 5-11. Interestingly, $[3T]H$ is predicted to form more readily in the case of thiophene deposition at $50eV$, when compared to argon at the same incident energy. This is in part due to the increased yield of atomic hydrogen during the thiophene depositions.

In contrast, argon is found to principally change of the number of carbon atoms in the $3T$ molecule. This differs from the modification by thiophene at the same energy in that a majority of the modification did not result in changes in carbon content of the $3T$.

5.3 Ab-initio Reaction Calculations

Ab-initio level calculations, carried out by co-worker Jasmine Davenport, are used to validate the predictions of the classical MD simulations. In this work, Davenport et al. compared the enthalpies of formation of a set of 11 thiophene and hydrocarbon molecules, using six different ab initio methods. The considered set of molecules consist of small hydrocarbon molecules: C_2H and CH_2 ; as well as, thiophene, C_4H_4S , and thiophene radicals. Reactions between thiophene radicals and hydrocarbon molecules are considered, given their possible importance in the polymerization of $3T$ during the SPIAD process. The GAUSSIAN 03⁸⁷ package is used to carry out the

calculations. The methods used in comparison of enthalpies of formation are B3LYP⁸³, BMK¹¹⁰, B98¹¹⁰, G2⁸⁴ and G3⁸⁵. Jasmine found that of the hybrid functional considered, B98 gave the most comparable energies to experimental and the combinatorial methods G2 and G3.

The reaction paths and transition states are then calculated using the IRC method and the B3LYP functional with the 6-311+G(3df, 2p) basis set. In Figure 5-10 the reaction profile of a C_2H radical interacting with a thiophene molecule is shown. It can be seen that radical attachment to a thiophene structure is a barrier-less reaction with an energy minimum of around 50 *kcal/mol*. However, if the reverse of this reaction is considered a reaction barrier can be seen. The reverse is a thiophene radical with an abstracted hydrogen reacting with an acetylene molecule. This reaction is seen to have a barrier of about 20 *kcal/mol*.

5.3.1 Discussion

The barrier between the thiophene radical and acetylene indicates that one of the primary products of the MD simulations may not play an active role in polymerization processes despite the product $[C_4H_4S]C_2H$ being more stable than the reactants and the quantities of acetylene being produced during the simulation. However, considering the formation of radical thiophene is not readily observed in the MD simulations, further ab-initio calculations involving fragmented rings need to be conducted. Accordingly, an initial evaluation of the dissociation energy of a thiophene ring is conducted. Non-zero point corrected energies are used to calculate the change in enthalpy of the following reaction: $C_4H_4S \rightarrow C_2H_2 + C_2H_2S$ where the C_2H_2S is linear and symmetric about the sulfur atom. It is found to about +9eV or +208 *kcal/mol*. This is significantly higher

than the 50 *kcal/mol* found with the aromatic thiophene. However, this reaction involves the scission of two bonds in the aromatic ring and further ab-initio calculations need be completed to fully explore the fragmented thiophene reactions with possible reactants, including the primary products found in the MD simulations; atomic hydrogen, C_2H_2 and C_2HS .

5.4 Summary

MD simulations using the newly parameterized REBO CHS potential are conducted in conjunction with ab-initio calculations to investigate the nature of hyperthermal atomic and polyatomic particles with a conjugated oligomer surface. Through the use of a set of single trajectory MD simulations the primary products of hyperthermal interactions with a $3T$ surface are found to be atomic hydrogen, C_2H_2 and C_2HS . Differences are seen between argon and thiophene depositions at different energies and on $3T$ oligomers oriented with backbones parallel and perpendicular to the substrate. Ab-initio calculations are conducted in order to further illuminate the SPIAD process.

Experimentally the SPIAD process is conducted at an energy “sweet spot” where the fracturing due to depositions is balanced by recombination¹³⁴. For Luke Hanley’s setup, 100eV is found to be preferred. For our simulations of thiophene and argon at 100eV similar products are predicted for both species. While the fusion of dissociated $3T$ molecules is predicted for argon bombardment, no clear differences between argon and thiophene are predicted from the simulations. However, at the lower energy of 50eV significant differences in the produced molecules is observed. In particular, more delicate changes to the surface structure are predicted as a result of thiophene

deposition than of argon deposition. This is seen despite the fact that argon produces more variance in carbon content of the modified $3T$ molecules $C_{11}H_7S$ and $C_{13}H_9S$. While this may lead to the polymerization of the $3T$, given that broken bonds are seen to reform, one of stipulations for the polymerization of conjugate species is that retention of the base molecule¹³⁴. And argon deposition is possibly too harsh a treatment to accomplish this.

Conversely, thiophene is able to induce small changes in molecular structure of an oligomer film. This is seen through the opening of $3T$ rings upon impact without the change in molecular mass of the modified $3T$. To account for the differences in argon and thiophene treatments, the difference in mass and the polyatomic nature of the thiophene may be important factors. First, the mass ratio of thiophene (84.14 *AMU*) and argon (39.95 *AMU*) is about 2.1:1. Thus, for equivalent kinetic energies the momentum of a carbon atom in the thiophene molecule is about $\frac{1}{5}$ of that of the argon atom at the same kinetic energy. Second is the dissociation of the thiophene on impact. This is found to have an enthalpy of dissociations of about 200 *kcal/mol* or 9*eV*. Therefore, in addition to having less momentum per atom there is also the absorption of energy upon impact in the form of breaking chemical bonds that can play a role in allowing for smaller changes in the oligomer film.

Finally, the SPAID processed is found to be a complex interaction involving dissociation of the incident polyatomic molecule, multiple reactions involving ring fragmentation and likely recombination with other incident $3T$ molecules. The combination of MD simulations and ab-initio calculations has contributed to the understanding between hyperthermal polyatomic molecules and oligomer films.

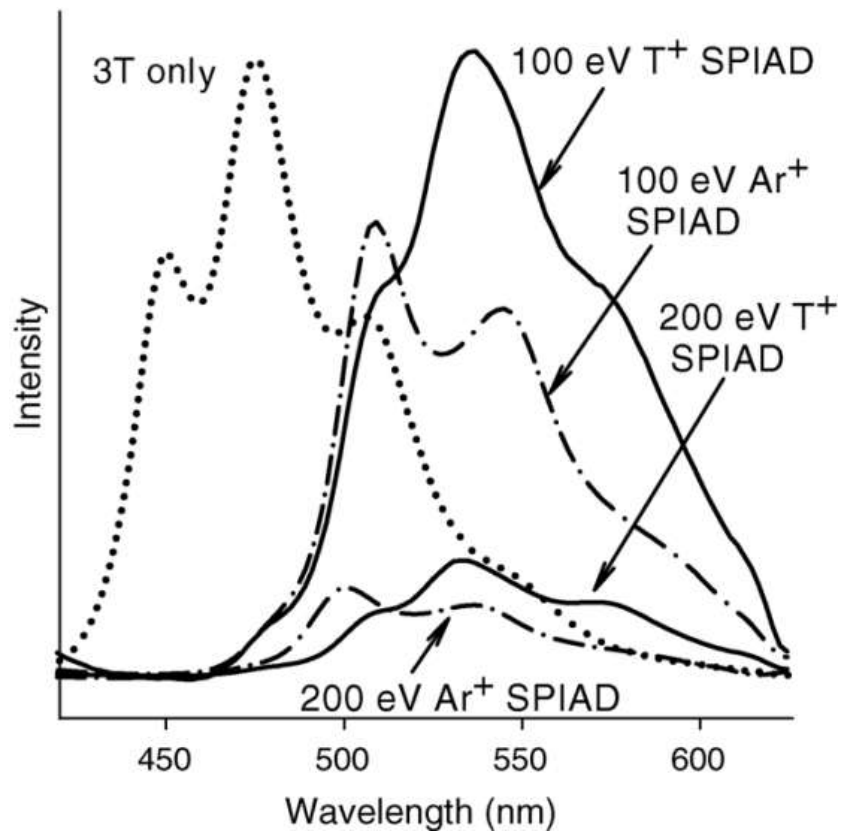


Figure 5-1. Photoluminescence spectra of 3T and SPIAD films produced with Ar⁺ and Thiophene (T⁺) at 100eV and 200eV³³

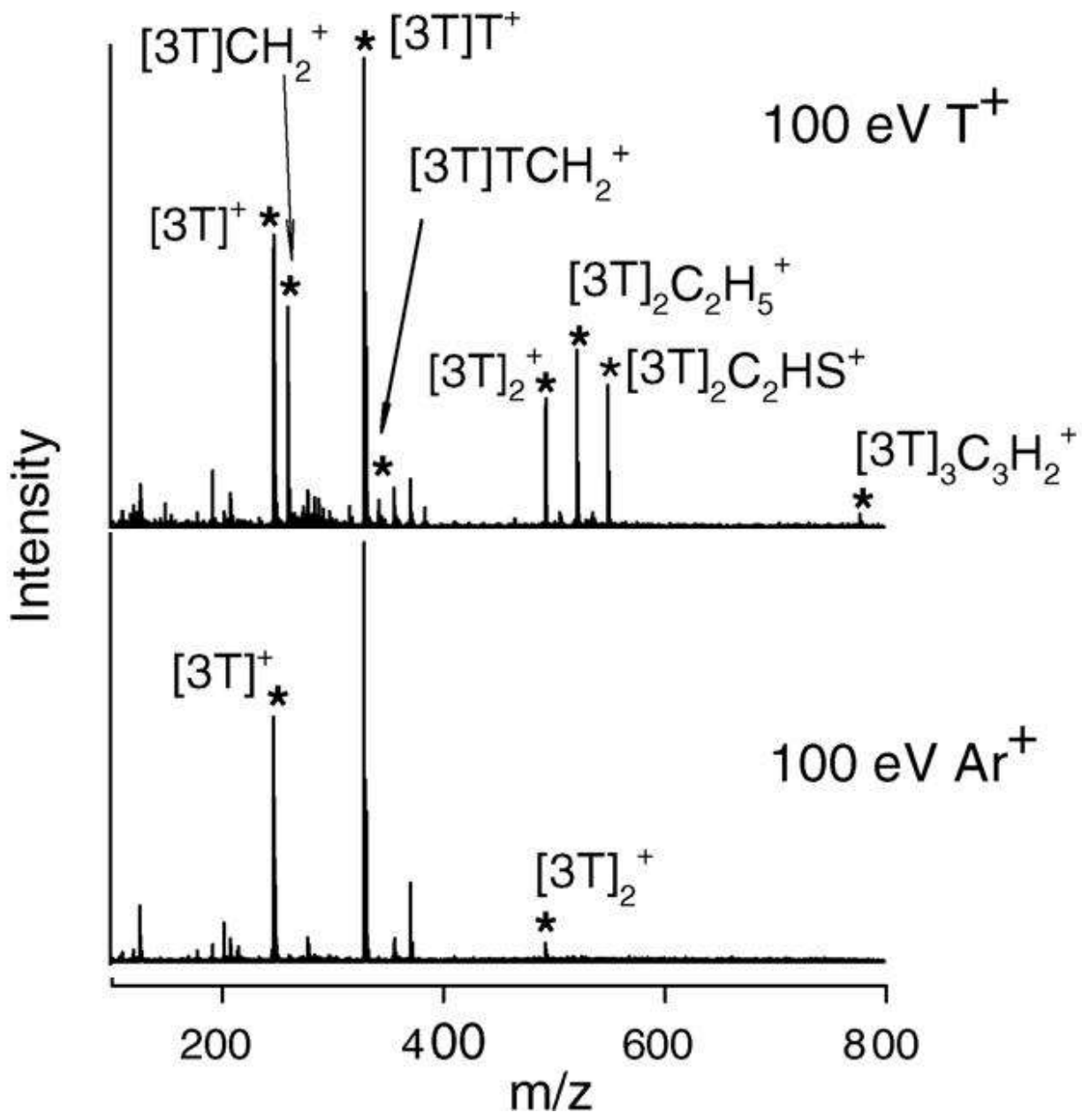


Figure 5-2. Mass spectra data³³

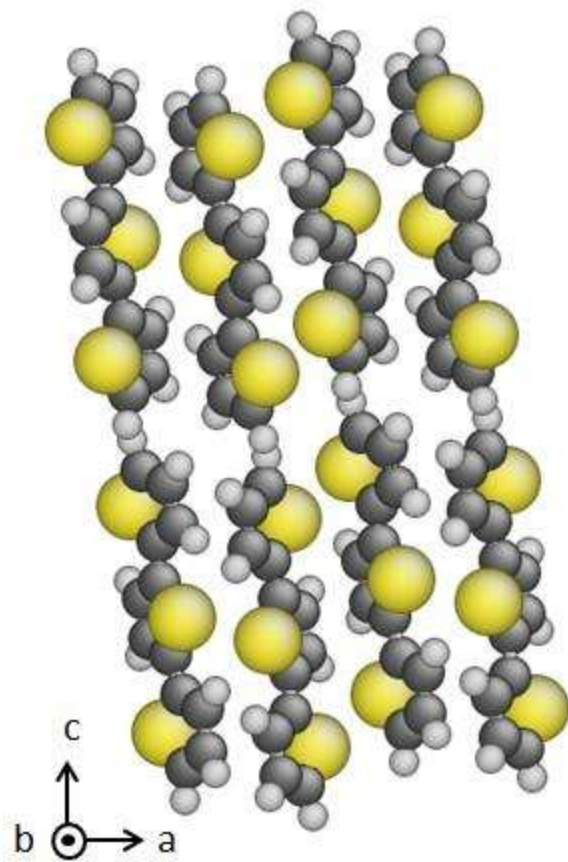
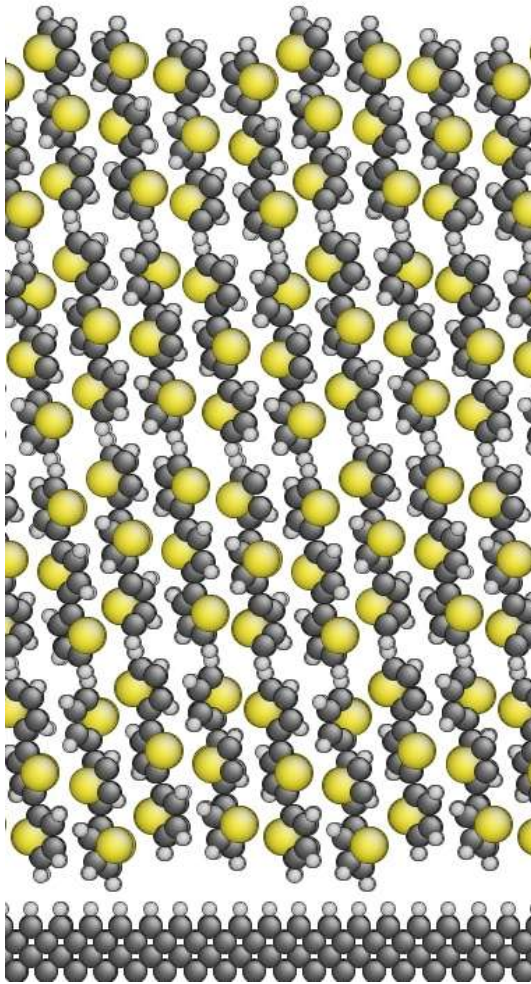
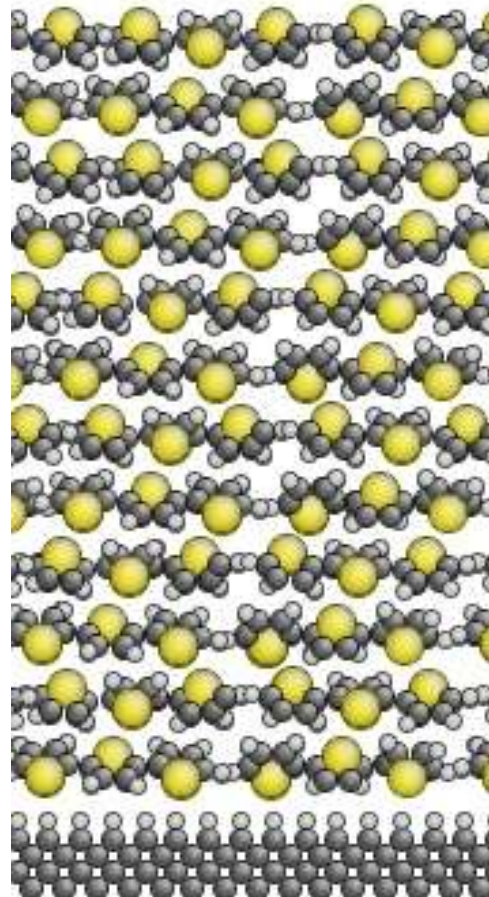


Figure 5-3. Terthiophene unit cell¹³⁵



Perpendicular



Parallel

Figure 5-4. Perpendicular and parallel configurations of the 3T films on a hydrogen terminated substrate.

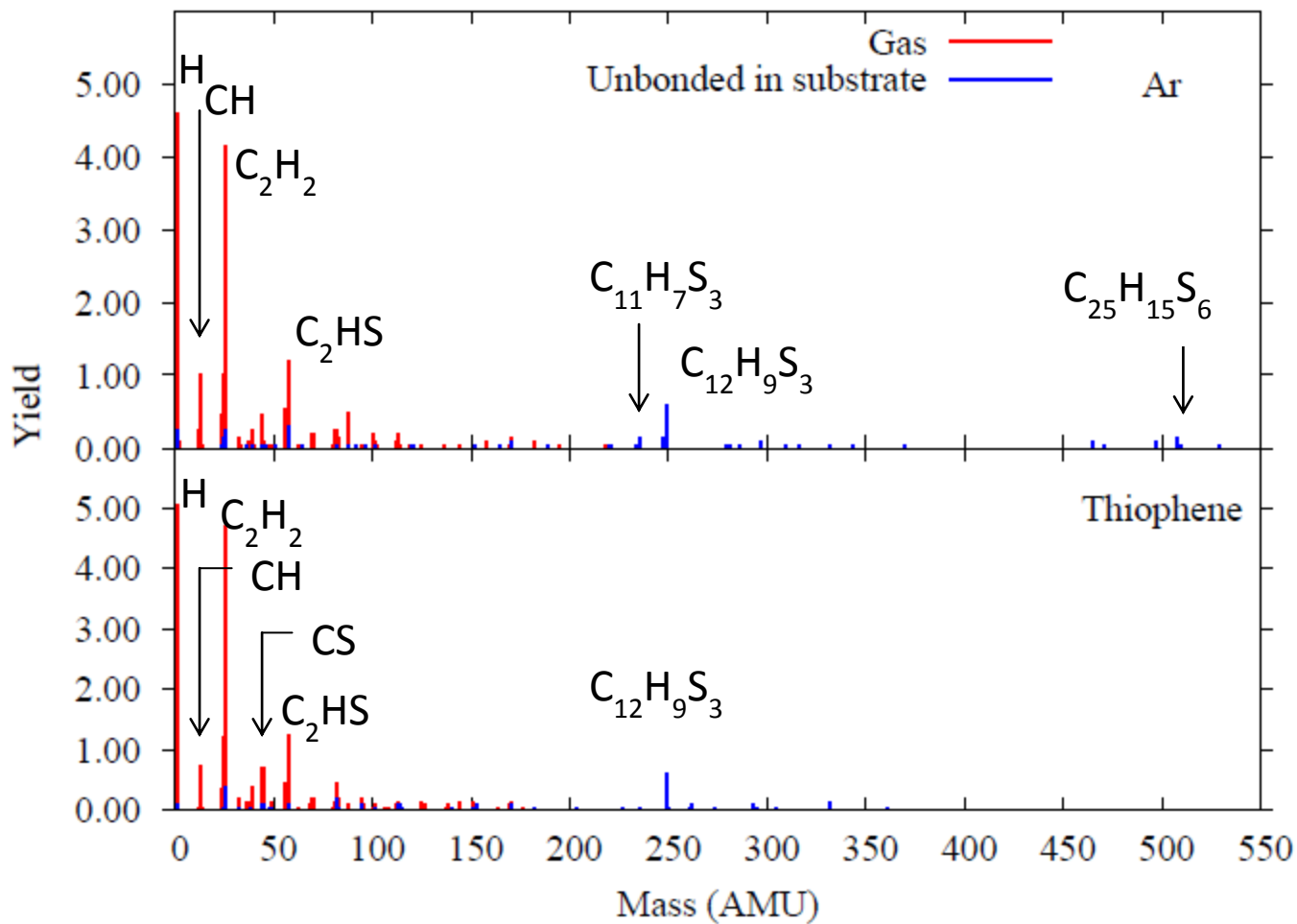


Figure 5-5. Yield at 100eV thiophene and Ar on the surface with 3T in the parallel configuration

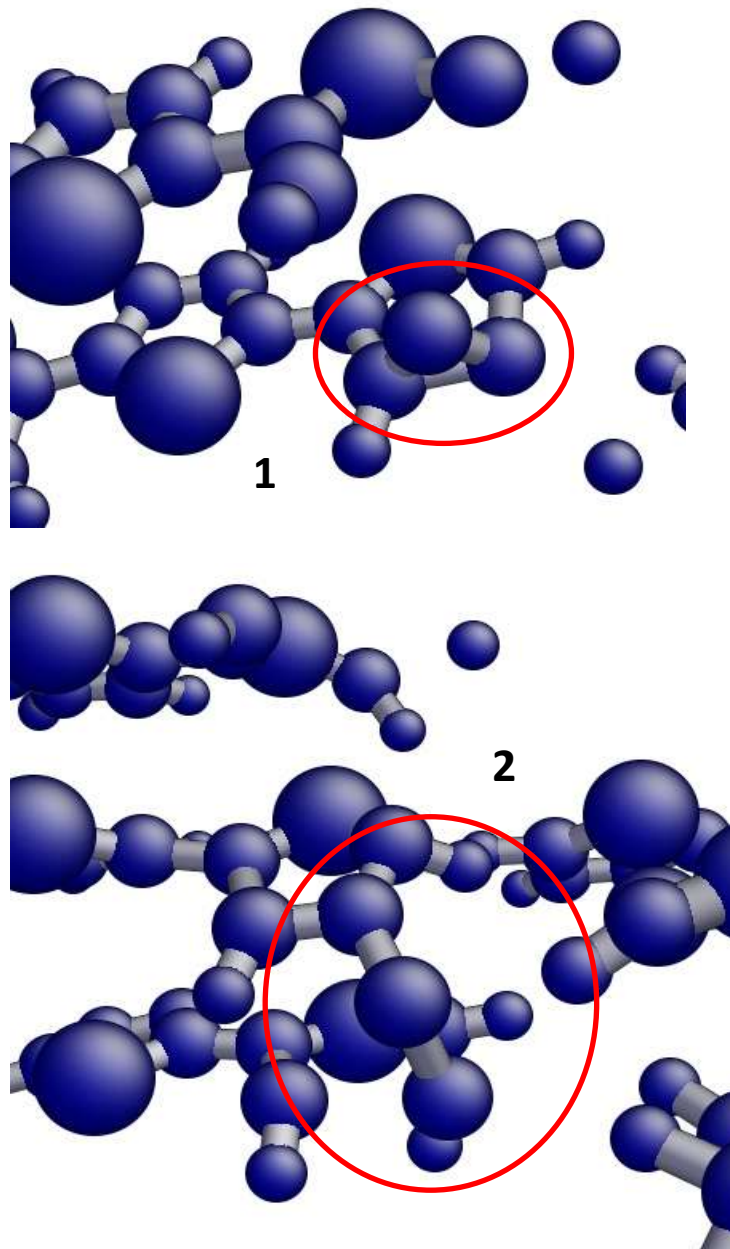


Figure 5-6. Two step process of the removal of a single atom from one 3T (1) and donating it to the set of 3T molecules below it (2)

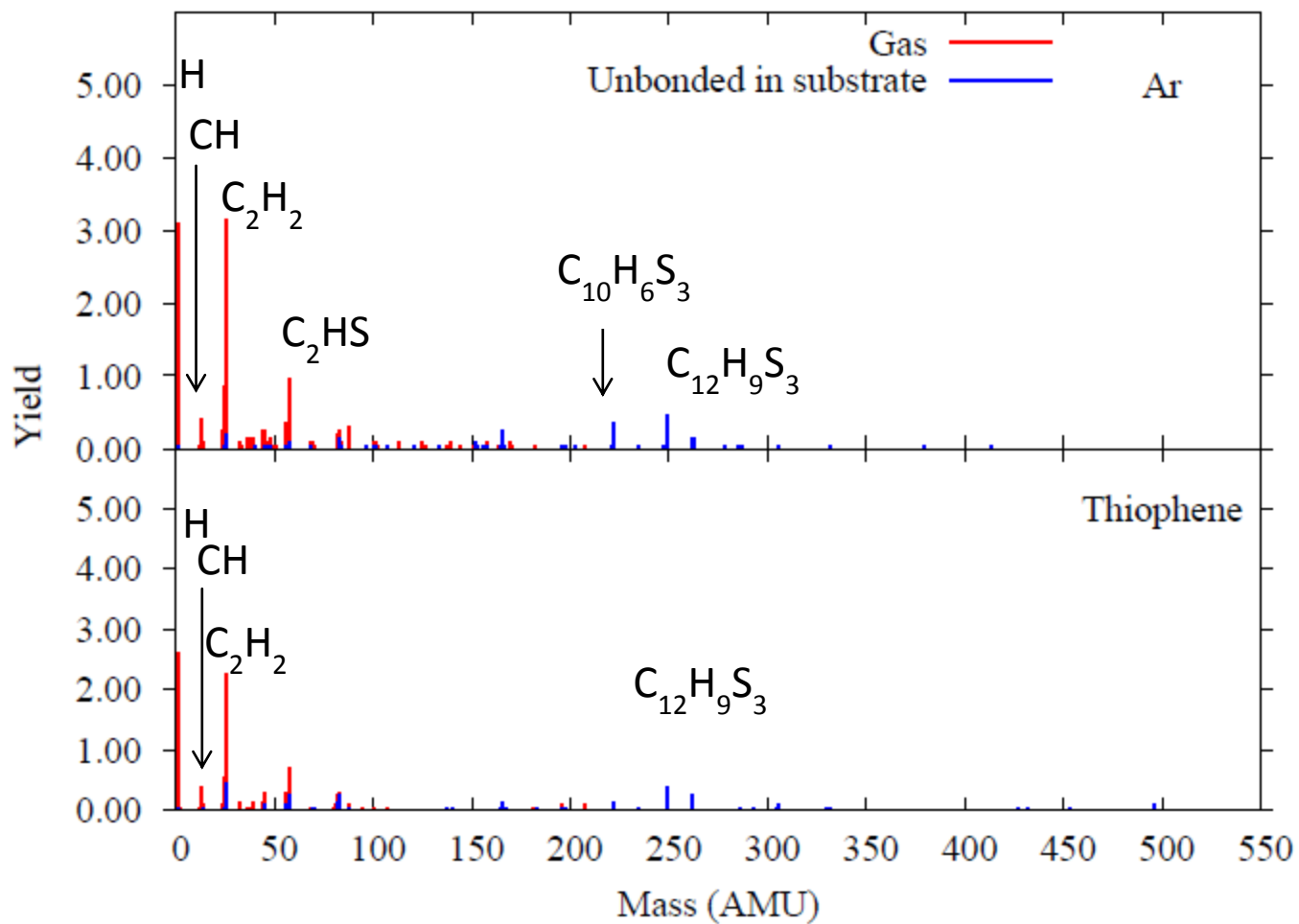


Figure 5-7. Yield at 100eV thiophene and Ar on the surface with 3T in the perpendicular configuration

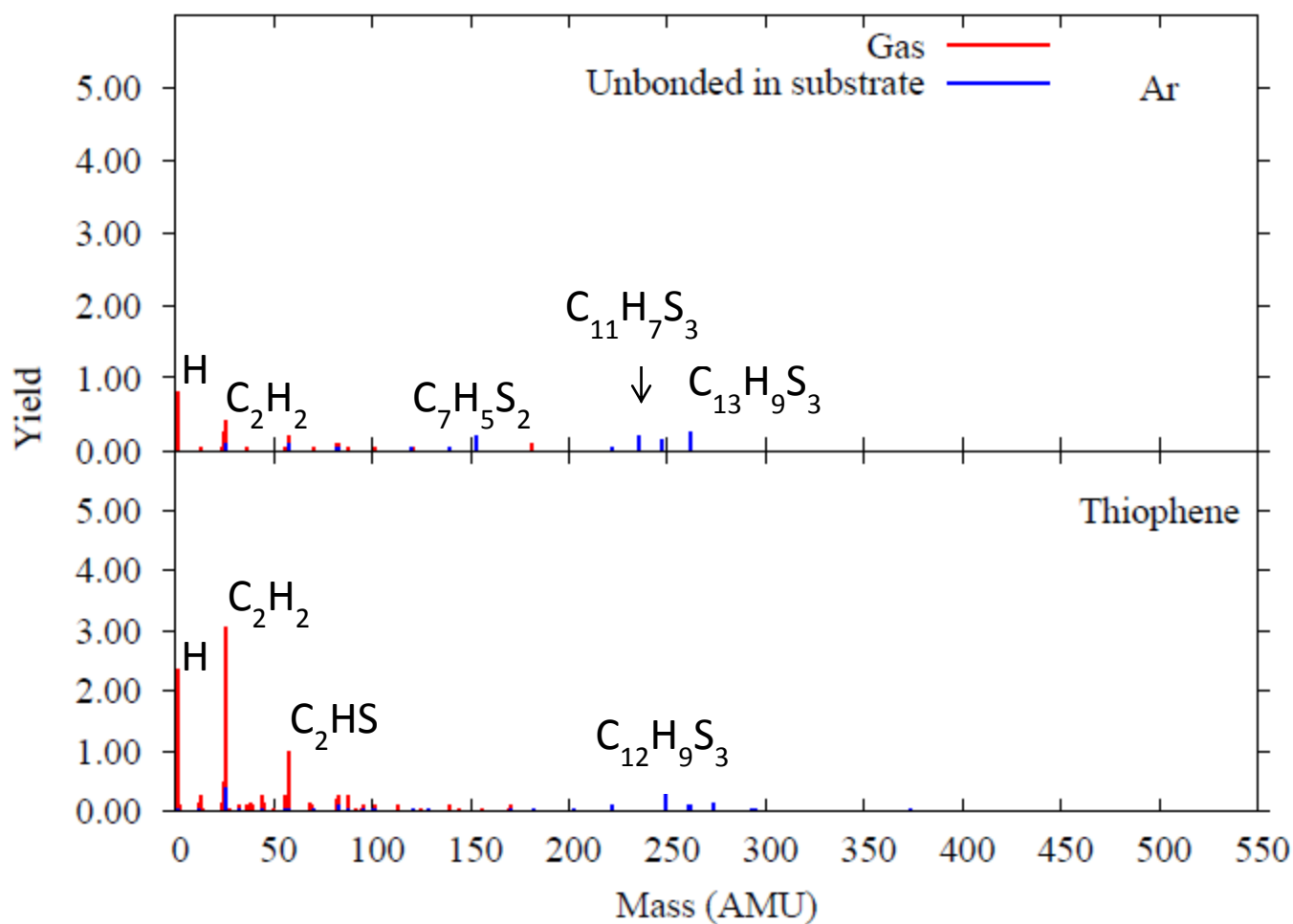


Figure 5-8. Molecular analysis of films resulting from 50eV argon and thiophene deposition on 3T in the parallel configuration

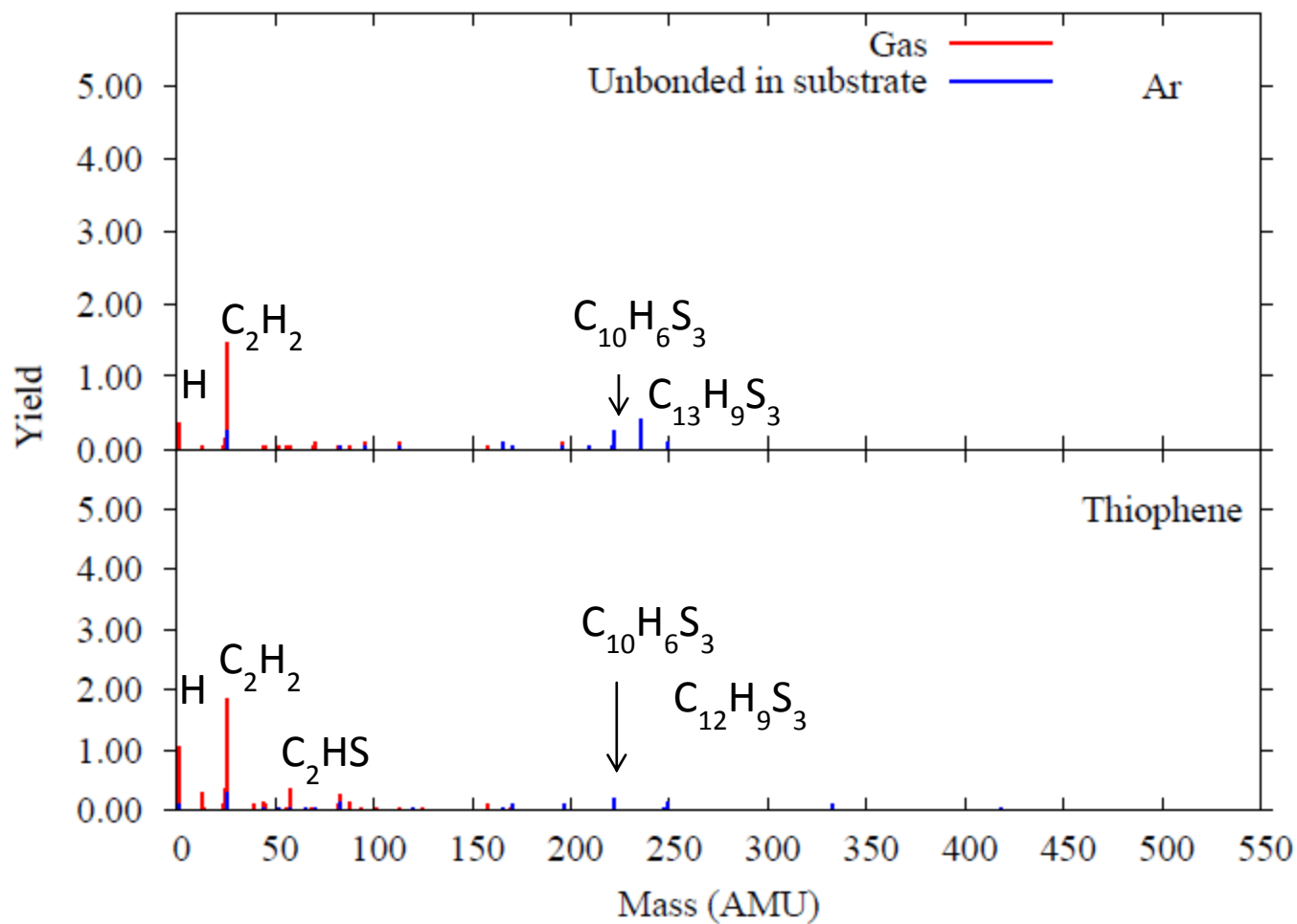


Figure 5-9. Molecular analysis of films resulting from 50eV argon and thiophene deposition on 3T in the perpendicular configuration

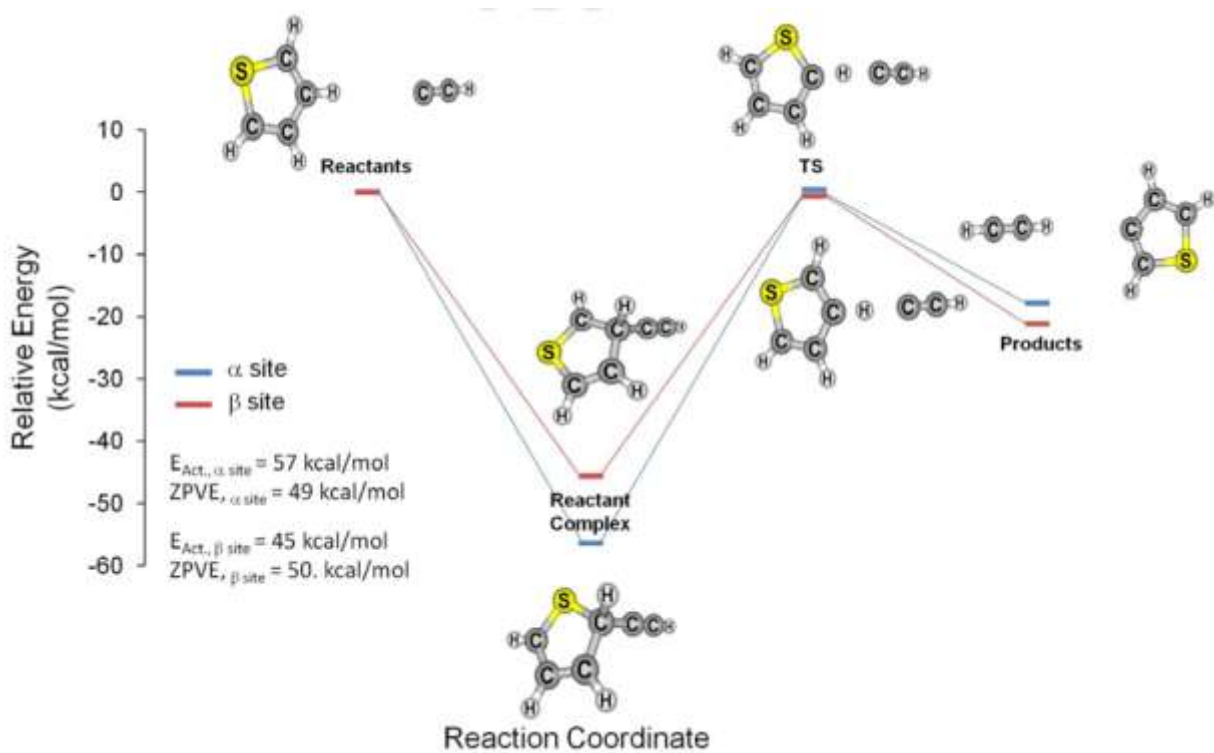


Figure 5-10. Reaction pathway of radical C_2H and C_2H_2 interacting with a thiophene molecule with calculated transition state energies of 49 kcal/mol (a site) and 50 kcal (b site).

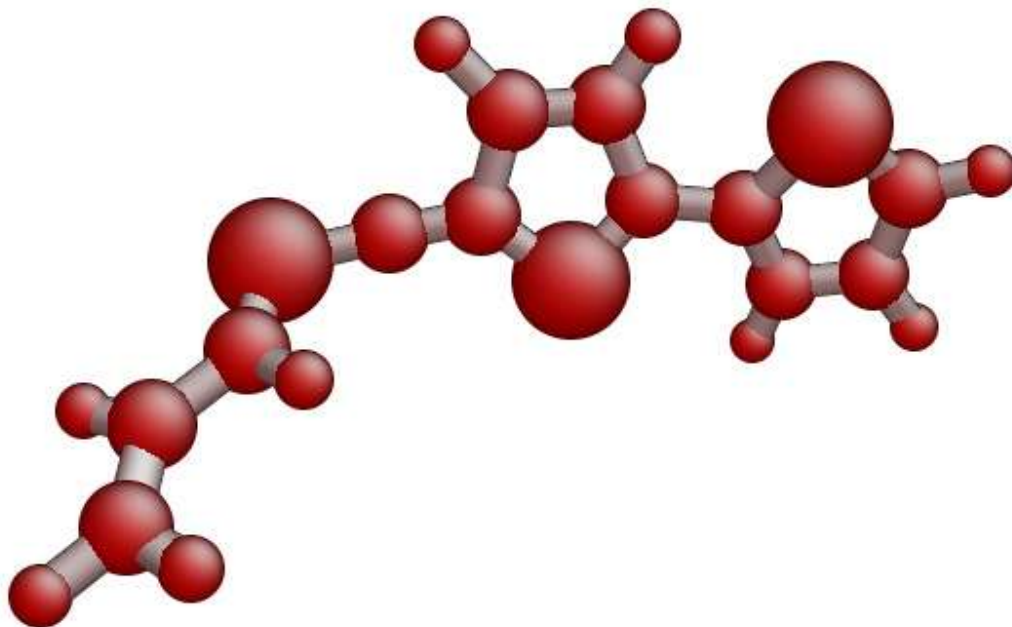


Figure 5-11. $C_{12}H_9S_3$ produced by 50eV thiophene on parallel 3T

CHAPTER 6 SURFACE MODIFICATION STUDIES

Plasma and ion beam treatments can involve numerous ionized species being impinged on a polymer surface. These particles have energies in the hyperthermal range of $1 - 500\text{eV}$ ^{20, 42}. They are produced during collisions between accelerated electrons and neutral gas species, such as argon, oxygen, carbon dioxide or water¹³⁸; however, the physicochemistry of the plasma and relative concentration of various species that are present is still an active area of research^{139, 140}. The concentration of ionized dissociative products is found to be appreciable^{4, 141}. Interestingly, treatments that increase the surface energy of a polymer in order to improve adhesion are less sensitive to the ions involved in the modification processes^{138, 142}. Other treatments, such as the creation of super hydrophobic surfaces, only occur in a narrow window of processing conditions¹⁴³.

In order to illuminate the processes in which plasma treatments modify polymer surfaces MD simulations are used to explore the effects of a reactive and non-reactive species being deposited on a polymer surface. These simulations allow for the decoupling of these species within the plasma, and the negation of environment effects. This allows for the direct analysis of modified surfaces before any subsequent reactions would occur. The archetypal species of argon and atomic oxygen are chosen to represent non-reactive and reactive species, respectfully. A representative set of polymer substrates: polyethylene (PE), polypropylene (PP) and polystyrene (PS) are considered.

6.1 Amorphous Polymer Model

In order to represent the faceted nature of an actual polymer surface, a random polymer network model is used. Polymer substrates are created by mapping monomers onto an equilibrated bead spring model¹⁴⁴. The bead spring model consists of randomly created continuous and terminating chains. Continuous chains are created through the PBC's perpendicular to the surface, and comprise 10% of the substrate model. These continuous chains are given a length less than the diagonal of the simulation cell to prevent them from migrating to the surface. Once the continuous chains are generated, random chains are added with the following constraints: new beads must be less than a bond length from all other beads in the system, except the one that it's bonded to, and bond angles, within the bulk, must be greater than 120°. The initial bead in a chain is positioned randomly, and subsequent beads are produced with a randomized translation vector. In order to facilitate the creation of a surface, chains are not created through the PBC in the xy plane. Specifically, beads within one bond length of the maximum and minimum of the simulation cell in the z direction are angled back into the cell, by adjusting the translation vector along the $z - axis$. Angles of 90° are accepted during the creation of surface beads.

The bead spring model is evolved under the constant number, volume and energy (NVE) ensemble, using the finite-extensible non-linear elastic (FENE) model in the LAMMPS package^{42, 145}. The FENE model was developed to study polymer melts, and has been shown to compare well to experimental neutron spin-echo data¹⁴⁴. The FENE model has the following energy function:

$$E = -0.5KR_o^2 \ln \left[1 - \left(\frac{r}{R_o} \right)^2 \right] + 4\epsilon \left[\left(\frac{\sigma}{r} \right)^{12} - \left(\frac{\sigma}{r} \right)^6 \right] + \epsilon. \quad (6-1)$$

The FENE bond parameters of $K = 30.0$, $R_o = 1.5$, $\varepsilon = 1.0$ and $\sigma = 1.0$, in LJ units, are used, with $\varepsilon = 2^{1/6}\sigma$. An inter-chain LJ potential is also used, with a cutoff of 1.12, and parameters $\varepsilon = 1.0$, and $\sigma = 0.9$, see Equation (2-6). A bond angle cosine potential,

$$E = K[1 + \cos(\theta)] \quad (6-2)$$

with $K = 10.0$, is used to avoid small bond angles, which are found to be problematic during atomic monomer addition. Langevin thermostats are applied to the entire system to maintain temperature.

Once an equilibrated bead spring model is achieved atomic-scale monomers are mapped onto the inter bead bonds. In order to maintain a reasonable density during bead-spring equilibration, periodic boundary conditions are enforced in all three dimensions. Therefore, chains that have migrated through the PBCs in the xy plane are cut. However, in order to avoid small molecular weight segments, cut chains with less than 10 monomers are shifted to connect with ends that are created during the creation of the surface.

Atomistic amorphous polymers are created by mapping atomic-scale monomer structures to the bonds of the reconstructed bead-spring model. To achieve this, coordinates of compressed forms of each monomer type are used as initial structures. The monomers are mapped onto each bond in the bead spring model by multiplying the fractional coordinates of a monomer by a set of orthogonal basis vectors. These basis

vectors for the initial monomer in a chain are generated using the bond vector and two other randomly generated vectors as inputs to the Gram-Schmidt procedure⁷⁴.

Tacticity of the subsequent monomer is controlled by utilizing a basis vector of the previous monomer as an input to the orthogonalization procedure, rather than a random vector. By multiplying this basis vector by one or negative one, isotactic or syndiotactic polymers can be produced, respectively. For atactic polymers, the tacticity multiple is randomly selected to be either one or negative one. For both PE and PP, the syndiotactic method is used. However, due to the phenyl ring present in PS, a random vector method for all monomers had to be used to achieve non-overlapping side groups.

In order to attain the maximum inter-atomic spacing during the creation of the atomistic model, a proximity constraint is enforced. The minimum proximity constraint is initialized as 0.8\AA . During the creation of each monomer the randomized basis vector is regenerated until this constraint is satisfied. If the threshold guesses for the creation of an initial monomer are exceeded, the entire model is deleted and restarted. During the creation of each subsequent monomer, if the threshold guess for a monomer is exceeded, then the entire chain is restarted. Furthermore, if the threshold number of restarts of either the chain or the entire model are exceeded the proximity constraint is decreased. Threshold values of 100 guesses for chain and monomer creation, and 50 restarts before the proximity constraint is decreased, are found to efficiently produce well spaced models. If a model is successfully produced, the proximity constraint is increased by 0.1\AA , and the creation of the atomic model is started over. Once an increase is followed by a decrease, the model is considered to be at its maximum

atomic spacing. Furthermore, if an inter-atomic spacing of greater than 0.1\AA is not achieved a new bead spring model is generated and equilibrated.

Once an atomic model is completed, it is evolved with limited interactions to allow for equilibrium bond lengths of the compressed monomers to be established. Limitations on the system include: fixed connectivity, and limiting inter-chain forces to LJ interactions. Langervan thermostats are also applied to the entire system, limiting the system to $100K$. Additionally, if the kinetic energy of the system surpasses 0.2 eV/atom , then the velocities of all the atoms are zeroed. After the atomic model undergoes an initial evolution, the system is equilibrated at the desired temperature.

To evaluate the amorphous nature of the constructed polymers the pair distribution function is used:

$$g(r) = \frac{1}{\langle \rho \rangle} \frac{dn(r,r+dr)}{dv(r,r+dr)} \quad (6-3)$$

Where ρ is the density of the polymer, dn is the number of atoms in the volume dv in between spherical shells with radii of r and $(r + dr)$. The pair distribution function, for the carbon atoms, is shown in Figure 6-2 for the equilibrated structures using a spherical cutoff of 8\AA and a dr of $1/100\text{\AA}$. For PE and PP the first and second neighbor peaks are for sp^3 carbons. While PS has peaks for both sp^3 and sp^2 . No long range order can be seen for any of the systems. The initial structures of PE, PP and PS are displayed in Figure 6-1, with individual chains highlighted. The surface area of each slab is $7.5\text{nm} \times 7.5\text{nm}$, with thicknesses of around 6nm . The densities are measured by using the maximum and minimum heights of the substrate's surfaces. Calculated densities are 1.01 g/cm^2 for PE, 0.91 g/cm^2 for PP and 0.94 g/cm^2 for PS. While the

exact densities of the polymers is not precisely achieved the values compare well with experimental values of 0.855 g/cm^2 for PE, $0.85 - 0.86 \text{ g/cm}^2$ for PP and $1.04 - 1.065 \text{ g/cm}^2$ for PS¹⁴⁷.

6.2 Methodology

Deposition energies of 25eV , 50eV and 100eV are chosen. Species are deposited with a flux of $5.08 \times 10^{23} \text{ molecules/s} \cdot \text{cm}^2$. While this is several orders of magnitude larger than fluxes found in ion-beam and plasma experiments, it corresponds to the minimum time necessary (3.5ps) for the fluctuations in kinetic energy due to each individual deposition event to dissipate. A total of 50 molecules are deposited on each polymer surface. This corresponds to a fluence of $8.9 \times 10^{13} \text{ molecules/cm}^2$, which is of the same magnitude as ion beam treatments for similar processes¹⁴⁸.

Depositions are conducted with the incident species placed normal to the substrate surface. The positions of the deposited species within the surface plane are randomly chosen. The temperature of the substrate is controlled by applying thermostats to the bottom 30% of the atoms. During depositions of hyperthermal atoms on polymer surfaces, significant energy is imparted onto the surface causing some mixing, and allowing for the possibility of a deposited species to come into contact with a thermostat atom. The connectivity of the deposited species is therefore monitored at the end of the simulation to determine if any species are found to be bonded to a thermostat atom. In the following work only one such instance is found, and the subsequent reaction is not counted in the provided analysis.

Molecules that are created during the deposition simulations are characterized by molecular mass. These molecules are considered sputtered from the substrate if they

contain less than 50 atoms and have a center of mass greater than $1nm$ from the initial surface maximum. Conversely, molecules with greater than 50 atoms that have a center of mass less than $1nm$ for the initial surface maximum are considered to be part of the substrate.

The change in coordination of a carbon atom in the system is used to establish the probability of different types of modifications that occur on the surface of the polymer. The total changes in carbon coordination is divided by the number of deposited species to give the yield of a particular modification. It is also considered that not all modified species remain in the substrate, and those that have been removed should not be counted as modified groups within the polymer surface. Therefore, the yield of each modification that is found to remain in the substrate is referred to as the “surface yield,” and is also displayed with the total yield of a modification. The percent of the total yield that is found to remain in the substrate is also displayed. It should also be noted that the second nearest neighbor information is not considered. Therefore, the bonds that are shown are for connectivity only and the existence of bond order is not taken into account.

6.3 Argon Deposition

Argon has been involved in plasma research since its discovery in 1928^{149, 150}. As it is an inexpensive noble gas, it remains prevalent in plasma and ion-beam use. Argon is used as a “working gas” or “feeder gas” in the RF chamber of plasma jets for surface modification of polymers¹⁵¹. Following treatment, polymers can be exposed to atmosphere, where the saturation of modified bonds can lead to functionalization¹⁵².

6.3.1 Results

First, the number of carbon and hydrogen atoms that are found to be sputtered are analyzed. In Figure 6-3, the yield of sputtered carbon and hydrogen is shown, due to argon bombardment at $25eV$, $50eV$ and $100eV$. A nonlinear response in energy is predicted for all the polymers considered, which agrees with the results of experimental studies of polymer etching using argon as a feeder gas. Egami et al. found the etching yield (EY) dependence on energy to vary based on the deposited ion¹⁵³. For argon, a square root dependence was found. Furthermore, this was also shown to be independent of polymer type. For the results of this study the square root relation does not completely hold; rather, the results indicate that steady state etching has not been achieved.

For steady state etching to occur, the ratio of $C:H$ being sputtered should be equal to that of the bulk polymer¹⁵⁴. This ratio is 1: 2 for PE and PP, and 1: 1 for PS. By measuring the total number of sputtered atoms at the end of the simulations for $100eV$ argon depositions, the ratio is found to be 1: 2.9 for PE, 1: 2.7 for PP and 1: 1.2 for PS. This indicates that steady state etching has yet to occur, even at the highest considered energy. This is reasonable for fluences on the order of $1 \times 10^{14} \text{ molecule/cm}^2$, which corresponds to low fluences used for surface modification purposes, as opposed to the higher fluences of $1 \times 10^{16} \text{ molecule/cm}^2$ - $1 \times 10^{18} \text{ molecule/cm}^2$ used for etching and film growth¹⁵².

For argon deposited at $25eV$ in these simulations, negligible sputtering and minimal surface modification is predicted for all considered polymers. For PE a yield of 0.2 corresponds to changes in carbon coordination from $2C-(C)H_2$ to $C-(C)H_2$ (Table 6-

1); this indicates that backbone scission can occur at this energy. In addition, minimal sputtering of atomic hydrogen is seen with a yield of 0.06. No yields over 0.06 are predicted for the PP surface according to the coordination and molecular analysis. However, trace amounts of sputtered methyl groups and broken backbone bonds are predicted to form. Lastly, absolutely no change in surface coordination or molecular content is predicted for PS exposed to $25eV$ argon.

In the case of $50eV$ argon on PE, backbone bond scission is predicted to be the primary process to result from the deposition through the creation of $C-(C)H_2$ from monomer carbons $2C-(C)H_2$ with a 1.18 yield, as indicated in Table 6-1. The creation of $2C-(C)H$ modifications from the monomer shows the propensity for $50eV$ argon to remove hydrogen atoms from the polymer is low for this energy, given the yield of 0.18. This is supported by the lack of molecular hydrogen in the sputtered particles, as illustrated in Figure 6-4.

Exposure of PP to $50eV$ argon results in the scission of backbone carbon bonds ($3C-(C)H \rightarrow 2C-(C)H$) with a yield of 0.6, as shown in Table 6-2. The yields of methyl groups are predicted to be approximately equal to the production of atomic and molecular hydrogen, see Figure 6-4. Of the modified species, the backbone carbons are determined to be the second most susceptible to being sputtered, after dissociated methyl groups, with 30% of the $2C-(C)H_2 \rightarrow C-(C)H_2$ forming sputtered products.

In the case of PS, the scission of the styrene ring ($2C-(C)H \rightarrow C-(C)H$) is predicted to be the most likely consequence of $50eV$ argon exposure, with a yield of 0.44 given in Table 6-3. The scission of backbone bonds ($3C-(C)H \rightarrow 2C-(C)H$) and backbone ring bonds ($3C-(C) \rightarrow C-(C)-C$) are predicted to be of similar probability with yields of 0.3.

However, the yield of dissociated styrene rings (C_6H_5) is found to be less than 0.1, as illustrated in Figure 6-4. The sputtering of modified carbon is predicted to be similarly probable for the four most probable modifications, with sputtering occurring for 20% – 30% of the produced modifications. Furthermore, trace amounts of C_2H_2 molecules are predicted to be ejected according to the molecular mass analysis given in Figure 6-4.

In summation, the primary product of the $50eV$ argon bombardment is scission of carbon-carbon bonds in the polymer surface, and the formation of atomic and molecular hydrogen. Specifically, atomic and molecular hydrogen are found to comprise 44, 28 and 53 number percent of the sputtered molecules for PE, PP and PS, respectively, as indicated in Figure 6-4. With an increase in kinetic energy from $50eV$ to $100eV$, sputtering and creation of molecular species is predicted to be 3-17 times greater for depositions at $100eV$ than at $50eV$. The atomic yield of PE, PP and PS is predicted to increase from 0.7 to 1.9, 0.6 to 8.3, and 0.62 to 10.0, respectively. Additionally, the most probable modifications for $50eV$ are found to remain the most probable for $100eV$, with increased yields.

The most probable modifications to the PE monomer due to $100eV$ argon are indicated in Table 6-1, with the most probable being $2C-(C)_2 \rightarrow C-(C)H_2$ and $2C-(C)H_2 \rightarrow 2C-(C)H$ with yields of 1.44 and 1.32 respectively. All other processes are predicted to occur with yields of 0.5 and less. Notable modifications are the formation of possible cross-links ($2C-(C)H_2 \rightarrow 3C-(C)H$) with a yield of 0.4. However, bond scission reactions are predicted to dominate with yields of 3.7, compared to bond forming process with yields of 0.42. The molecular products of bond breaking are sputtered hydrogen,

molecular hydrogen and single and double carbon containing molecules (see Figure 6-5).

In Table 6-2 the modifications of PP due to 100eV argon are shown. Specifically, the scission of carbon-carbon bonds is still the dominate process. With backbone bonds breaking with a greater yield of 1.18, than side group bonds with a yield of 0.84. Modifications resulting in the dissociation of a single methyl or hydrogen atoms from the backbone are also predicted with yields of around 0.4. The molecular analysis reveals that the majority of the sputtered species are dissociated atomic and molecular hydrogen and methyl groups, Figure 6-5.

For PS, the trends for 50eV deposition are also observed to be similar to the trends for 100eV deposition. In particular, the four most probable coordination modifications remain the same with increased yields, as shown in Table 6-3. The scission of styrene carbon bonds is the most probable modification and the formation of C_2H_2 is predicted to dominate the carbon species formed with a yield of 0.4, as illustrated in Figure 6-5. This agrees with previous studies using the second generation REBO potential⁴⁵ which predicted that C_2H_2 production occurred due to the scission of carbon-carbon bonds on the backbone and within the styrene ring. According to the coordination analysis conducted in this work, the primary production of C_2H_2 occurs due to the scission of styrene rings. In particular, the production of $C-(C)$ is almost exclusively due to the scission of styrene carbons ($2C-(C)H$), as indicated in Table 6-3. This may be due to differences in the model used for the simulation. Specifically, Vegh and Graves used vertically aligned chains, while the model used in this work is a faceted surface with the ring more exposed than the backbone.

6.2.2 Discussion

The yield of carbon atoms per *Ar* is found to vary experimentally with system setup¹⁵⁵; yet, are usually in the tens of atoms per incident species. This compares well with the simulation results, which predict a yield of 2 carbon atoms for PE, 3 carbon atoms for PP and 4.5 carbon atoms for PS, as illustrated in Figure 6-3. Experimental values of steady state etching found yields of 4 carbon atoms per *Ar* at 400eV, for a plasma polymerized hydrocarbon film on *Si*¹⁵⁶. These values should be considered lower than values obtained by steady state etching in experiments, since the *C:H* ratio is not equal to the ratio found in the bulk polymer.

For a fluence of $8.9 \times 10^{13} \text{ ions/cm}^2$ the resulting concentrations of carbon coordination types due to 100eV argon modification are shown in Figure 6-6. For PE and PP, a yield of over 1.0 per ion is found for both *C-CH₂* and *2C-CH* modifications. This corresponds to an even number of modifications involving the scission of carbon-carbon backbone bonds and carbon-hydrogen bonds within the substrate for PE. This is supported by the primary concentration of *H* and *H₂* in the molecular analysis of the sputtered species. For PP, a yield of 1.5 *C-CH₂* groups is due to a combination of dissociated backbone bonds and oxygenated methyl groups. Methyl groups are found to have an average removal yield of 0.3 per deposited ion. For PS the primary modification is to the styrene ring, where ring scission is seen to occur with a yield around 2.0, and hydrogen removal from the ring is seen to occur with a yield of 0.5. From the molecular analysis the majority of carbon containing molecules that have been sputtered are *C₂H₂*, which agrees with previously published studies using the second generation REBO potential to model *Ar* deposition on PS⁴⁵. Further, the higher

molecular weight species that are formed are consistent with the removal of styrene groups, and entire monomers. The most probable modifications at 50eV are also found to be the most probable at 100eV .

Rate increases for the two most probable modifications of PE and PP are predicted to increase by a factor of 2.0, and a factor of 4.5 and 3.5 for PS. The difference in products between 50eV and 100eV reveal the nature of the modification process of argon. In particular, deposition at both of these energies has as the primary modification the scission of carbon-carbon bonds. The creation of atomic and molecular hydrogen is predicted to occur at much lower yields than carbon-carbon bond scission for 50eV argon, while a substantial increase in hydrogen production is predicted for 100eV argon. This indicates that the oxidation of the polymer surface is a secondary interaction, while the breaking of carbon-carbon bonds is the primary interaction.

While these results illuminate the probability of various changes in bonding to occur during hyperthermal argon bombardment, they also provide probable initiation sites for functionalization. Deposition in the simulations is conducted in perfect vacuum, but actual surface modifications occur at low pressure reactors or in air where the surrounding gas phase molecules can interact with the modified surface. As with previous studies this MD study will provide the bases for future work involving quantum chemical analysis of possible reactions that can occur with the identified surface modifications.

6.2.3 Conclusions

This work identifies probable modifications of hyperthermal argon on a polymer surface on three prototypical surfaces PE, PP and PS. The magnitude of carbon and

hydrogen removal is predicted to be approximately the same as published experimental values for similar systems. The most probable modifications for PE, PP and PS are shown in Table 6-1, Table 6-2 and Table 6-3 respectively. Given the simple structure of PE it is not surprising that the most probable modifications are simply chain scission and the removal a single hydrogen atom. For PP, the most probable modifications are chain scission, the dissociation of side groups, and the removal of single hydrogen atoms from the backbone chain. In the case of PS, chain scission and ring scission are found to be almost equally probable. While these results are generally predictable based on the structure of the studied polymers, they provide a statistical basis for comparison to reactive species such as atomic oxygen.

6.3 Reactive Species

The etching of microelectronics using molecular oxygen as a feeder gas in low temperature radio frequency vacuum chambers has been a focus of study since the 1960's¹⁵⁷ and the ability of oxygen based plasmas to effectively etch surfaces is well established²¹. A detailed analysis of reactive species interactions with polymer surfaces is necessary to facilitate future development of more complex treatments. These more complex treatments including the use of multiple feeder gases and plasma jet systems that operate in air. Plasma treatments use mixtures of different feeder gases to achieve increasingly subtle changes to a surface¹⁵⁸. For example, using a combination of CO_2 and H_2O has been attempted to produce $COOH$ functional groups¹⁵⁹; however, in this work atomic oxygen was reported to degrade the polymer surface. More recent studies have found atomic oxygen ion concentrations in air jet plasmas^{141, 160}. Therefore, more detailed analysis of atomic oxygen-polymer surface interactions using computational

methods can offer further insight into the nature of reactive species, and polymer surface interactions of importance for multiple processes.

Here, simulations are conducted using the updated hydrocarbon and oxygen coordination function values for the second generation REBO potential. For comparative analysis to non-reactive species (argon deposition), depositions are conducted at incident energies of $25eV$, $50eV$ and $100eV$. The flux of $8.9 \times 10^{13} \text{ molecules/cm}^2$ and fluence of $5.08 \times 10^{23} \text{ molecules/s} \cdot \text{cm}^2$ is also equivalent to the conditions considered in the argon atom depositions.

6.3.1 Results

The reactivity of oxygen leads to a lower threshold of kinetic energy to induce modification of a polymer surface relative to non-reactive species like argon. This can be seen in the sputtering yield from the simulations, given in Figure 6-7, in that appreciable sputtering occurs at $25eV$, with hydrogen yields of 1.0 or greater. In contrast, only negligible sputtering occurs due to the deposition of argon at the same energy, Figure 6-3. This phenomenon is known as chemical sputtering²⁰. Sputtering of carbon atoms is predicted to be less energy dependent compared to argon, with the carbon atoms exhibiting a yield ranging from 0.9 to 1.9 for PS between $50eV$ and $100eV$. This is a substantially smaller increase than that predicted for argon. Furthermore, the ratio of carbon to hydrogen in Figure 6-7 is predicted to correspond well to the oxidation properties of atomic oxygen for PP, PE and PS.

By analyzing the molecular mass of the sputtered molecules the primary content is found to be atomic and molecular hydrogen as expect during oxidation of the polymer surface. The molecules produced by $50eV$ atomic oxygen are shown in Figure 6-8, and

the yield can be compared to that of argon in Figure 6-4. Yields of atomic and molecular hydrogen are predicted to be 1.4 for PE and PP, and 1.1 for PS. These yields are about 10 times that of the yield for 50eV argon. By comparing Figure 6-3 and Figure 6-7, the yields of sputtered hydrogen are seen to be similar in magnitude for 100eV depositions of oxygen and argon. However, the yield of sputtered carbon species is much less dependent on energy for oxygen than for argon. The yields of carbon at 25eV, 50eV and 100eV are 0.1, 0.44 and 0.94 for PE, 0.16, 0.98 and 1.3 for PP, and 0.48, 0.86 and 1.94 for PS. Therefore, sputtering of molecular carbon containing species due to atomic oxygen is predicted to be limited and further molecular analysis is not included, except for the case of PS.

The reflection yield (RY), or number of incident species that bounce off the surface without chemically bonding to it, is predicted to have a greater dependence on polymer composition than incident energy. For PS the RY of atomic oxygen is predicted to be zero for all cases, and it is 0.1 for PE and PP. The number percent of the formed molecular species that contain deposited oxygen atoms is found to be inversely proportional to the deposition energy. In particular, the yield of oxygen atoms in the created molecules is roughly constant for the considered polymers and energies: 0.3 to 0.4 for PE, 0.3 to 0.5 for PP, and 0.1 to 0.2 for PS.

The number of sputtered molecules increases with the kinetic energy of the deposited species. For PE and PP, the number yield of created molecules is approximately 1.0, 2.0 and 4.5 for deposition energies of 25eV, 50eV, and 100eV respectively. The total yields for PS are slightly lower at 0.8, 1.6 and 2.8 for the same respective energies.

Coordination analysis is conducted on the produced films for all carbon and oxygen atoms. The results of the changes in bonding are shown in Table 6-4 through Table 6-12 for yields greater than 0.1. For oxygen on PE the monomer carbons are modified with yields of 1.9, 3.6 and 6.6 for 25eV, 50eV and 100eV, respectively. At 25eV and 50eV chain scission is predicted to be the dominant process with yields of 0.68 and 0.7 respectively. In the case of 25eV a majority (52%) of the deposited oxygen atoms form a bond with a substrate carbon causing chain scission ($C-(O)$). This can be seen to correspond to the formation of $C-(C)H-O$ and $C-(C)H_2-O$, with yields of 0.24 and 0.28, respectively.

For depositions at 50eV the yield of bonded oxygen species is predicted to only increase 10% to a yield of 0.84. The dominate products of $2C-(C)$ and $C-(C)H_2$ form due to the oxidation of the monomer are the same as with 25eV and 100eV. For 100eV the incorporation of deposited oxygen into the substrate is predicted be the same as for 50eV. However, the most probable result of the 100eV deposition is predicted to be the oxidation of a monomer to form $2C-(C)H$ with a yield of 2.4. The second most probable modification being chain scission to produce $C-(C)H_2$. The substrate modifications due to direct bonding to oxygen are seen to be the incorporation of oxygen as a side group $2C-(C)-O$ with a yield 0.22, and chain scission $C-(C)H_2-O$ with a yield of 0.2.

For atomic oxygen modification of PP the monomer carbons $3C-(C)$, $C-(C)H_3$ and $2C-(C)H_2$ are modified with yields of 1.7, 3.2 and 6.7 for 25eV, 50eV and 100eV respectively, Table 6-7, Table 6-8 and Table 6-9. Each atom type in the PP monomer is predicted to react at approximately the same rate as the others. In the case of depositions at 25eV (shown in Table 6-7) the primarily bonding of the deposited oxygen

atom is to a single carbon, with a yield of 0.44. The deposited oxygen is seen to bond to the side group, causing the removal of a hydrogen, with a yield of 0.24. Bonding of the deposited oxygen to backbone carbons is also found to occur resulting in the scission of a carbon-carbon bond, with a yield of 0.12. As with the depositions at 25eV, at 50eV the oxidation of the polymer with little chain scission is predicted to occur. The oxidation of the methyl group to form $C-(C)H_2$ is also predicted to be the most probable reaction with a yield of 0.6. This is primarily due the bonding of oxygen to carbon in the substrate with yields of 0.3 and 0.36 for $C-(O)-C$ and $C-(O)$. Also, limited amounts of water and OH are predicted to form.

At 100eV (Table 6-9) the oxidation of the methyl group, the scission of the backbone chains and the oxidation of the backbone are the most observed reactions in the simulations with yields of 0.6, 0.34 and 0.32, respectively. The deposited oxygen is predicted to mainly form $C-(O)$ and $C-(O)-C$ bonds within the substrate, with yields of 0.32 and 0.20, respectively. Since a majority of the oxygen modification resulted in yield less than 0.1, these results are not shown in Table 6-9. The only formed species with a substantial probability is the attachment of the deposited oxygen to an oxidized methyl group with a yield of 0.18.

For 25eV, oxygen on PS scission of the styrene ring is seen to be the predominate interaction. This forms $C-(C)$, $C-(C)-O$ and $2C-(C)-O$ with yields of 0.52, 0.56, and 0.64, respectively. 100% of the deposited species are predicted to bond to the substrate with $C-(O)-C$ coordinated oxygen being the most likely. The change in coordination of $2C-(C)$ into $C-(C)$ exhibits scission of styrene rings with a yield of 0.52. In addition, the formation of $C-(O)-C$ coordinated oxygen atoms indicates that the oxygen is not forming

at the end groups in the broken ring structures. Upon visual analysis of the substrate, a wide variance of styrene oxygen bonds is predicted to occur. Rather, the deposited oxygen is found to both incorporate into the ring and form bridge sites, as illustrated in Figure 6-9.

At 50eV of incident energy, the scission and removal of hydrogen from the styrene ring is seen by the change of $2C-(C)$ to $C-(C)-C$ and $C-(C)H$ with yields of 0.46 and 0.6 respectively. Backbone carbon-carbon bonds are predicted to be dissociated by the loss of a carbon neighbor of $3C-(C)$ with a yield of 0.34. Again $C-(O)-C$ coordinated oxygen atoms are found to dominate, consisting of 76% of the deposited species. Significant amounts of $2C-(C)H$ yielding $C-(C)-O$ and $2C-(C)-O$, show that ring bridging and incorporation of deposited oxygen is taking place.

Similar concentrations of $C-(O)-C$ coordinated oxygen, and $2C-(C)-O$ and $C-(C)H-O$ coordinated styrene carbons are predicted to occur for depositions at 100eV , as indicated in Table 6-12. Increases in ring scission and removal of hydrogen from the ring are also predicted, by an increase in the modification of $2C-(C)H \rightarrow C-(C)H$ and $2C-(C)H \rightarrow C-(C)-C$ with yields of 1.6 and 0.96, respectively. As with argon deposition processes, the dominate molecular species is predicted to be C_2H_2 with a yield of 0.24.

6.3.1 Discussion

Atomic oxygen deposited at 25eV , 50eV and 100eV shows a substantial affinity to form bonds within the hydrocarbon polymers PE, PP and PS with uptakes of 80% to 100%. Sputtering of carbon containing molecules is predicted to be low for PE and PP. However, greater amounts are seen for PS due to the removal of portions of the styrene ring.

This corresponds well to experimental findings that atomic oxygen primarily degrades polymer surfaces during modification in that atomic oxygen is not found to significantly contribute to etching¹⁶¹ or functionalization¹⁵⁹. However, it should be noted that due to the short interatomic cutoff of the REBO potential, the probable formation of *OH* groups during depositions is likely underestimated.

For PE and PP, the products formed with the highest fidelity are predicted to be the scission of a backbone chain and the removal of a single hydrogen atom from the monomer while leaving the backbone bonds intact. Upon visual analysis these processes are found to be related to the initial interaction with the polymer, while the subsequent formation of carbon-oxygen bonds occur during secondary reactions. The presence of oxygen bonded to a single carbon is predicted to be the most probable configuration with deposition energies of $25eV$. However, the formation of hydroxyl groups and *C-(O)-C* bonds increases with energy.

PS reacts strongly with atomic oxygen to form bonds *C-(O)-C* within the styrene ring. The scission of the styrene ring can lead to the removal of oxygen and hydrocarbon containing compounds causing the relative sputtering of carbon containing species to be higher than for PE and PP. Similar results have been seen experimentally with the photo oxidation of PS, where ring opening and *O-(C)-O* bond formation were also seen to dominate¹⁶². The results of this work do not include the effects of UV radiation; however, the energy necessary to break styrene ring bonds is provided by the kinetic energy of the atom.

A comparison of the most probable modifications due to $100eV$ argon and oxygen depositions on PE, PP and PS are given in Table 6-13. It can be seen that for PE,

despite both atoms having the same kinetic energy the breaking of the backbone bonds due to oxygen is about half that due to argon. Furthermore, the removal of a hydrogen from the backbone is substantially higher for oxygen deposition. For PP, the abstraction of hydrogen is predicted to about twice that of argon, while the scission of backbone bonds is found to be similar. For PS, similar values are observed for carbon-carbon bond cleavage, but hydrogen abstraction from a styrene ring is predicted to be about twice as likely to occur.

6.5 Summary

Argon and atomic oxygen have been deposited on a set of prototypical polymers, and the nature over their interactions has been explored with MD simulations. The primary function of energetic particles is predicted to be the cleavage of carbon-carbon bonds for PE, PP and PS alike. *Ar* at $50eV$, produces little oxidation of the surface. However, with an increase to $100eV$ the cleavage of the carbon-carbon bonds remains the primary modification mechanism, with oxidation occurring as a secondary process.

As expected, atomic oxygen is found to remove hydrogen from the substrate and produce little etching of the surface. This is due to a combination of preferential removal of hydrogen, when compared to argon, and the bonding of oxygen within the substrate. The bond of atomic oxygen for the considered polymers is found to be complex especially in the case of PS.

In this work changes in the bonding are identified for hyperthermal augmentation of PE, PP and PS by non-reactive and reactive particles. The analysis of probable formations within the modified structures will hopefully lead to a better understanding of plasma modification of polymer surfaces.

Table 6-1. Coordination analysis of *Ar* deposition on PE

Energy	Initial coordination		Final coordination	Total yield	Surface yield	Dissociated (%)	Dissociated yield
25	2C-CH ₂	→	C-CH ₂	0.20	0.20	0	0.00
50	2C-CH ₂	→	2C-CH	0.18	0.18	0	0.00
	2C-CH ₂	→	C-CH ₂	1.18	0.92	22	0.26
100	2C-CH ₂	→	C-C-C	0.16	0.14	13	0.02
	2C-CH ₂	→	C-CH ₃	0.38	0.28	26	0.10
	2C-CH ₂	→	3C-CH	0.40	0.38	5	0.02
	2C-CH ₂	→	C-CH	0.50	0.14	72	0.36
	2C-CH ₂	→	2C-CH	1.44	1.32	8	0.12
	2C-CH ₂	→	C-CH ₂	2.48	1.62	35	0.86

Table 6-2. Coordination analysis of *Ar* deposition on PP

Energy	Initial coordination		Final coordination	Total yield	Surface yield	Dissociated (%)
25	-	→	-	-	-	-
50	C-(C)H ₃	→	C-(C)H ₂	0.16	0.16	0
	C-(C)H ₃	→	(C)H ₃	0.18	0.00	100
	2C-(C)H ₂	→	C-(C)H ₂	0.40	0.28	30
100	3C-(C)H	→	2C-(C)H	0.60	0.52	13
	2C-(C)H ₂	→	C-(C)H	0.12	0.06	50
	C-(C)H ₃	→	C-(C)H	0.14	0.06	57
	2C-(C)H ₂	→	3C-(C)H	0.14	0.08	43
	2C-(C)H ₂	→	C-(C)H ₃	0.14	0.10	29
	3C-(C)H	→	3C-(C)	0.16	0.16	0
	3C-(C)H	→	C-(C)-C	0.20	0.10	50
	C-(C)H ₃	→	2C-(C)H ₂	0.34	0.30	12
	3C-(C)H	→	C-(C)H	0.34	0.12	65
	2C-(C)H ₂	→	2C-(C)H	0.36	0.34	6
	C-(C)H ₃	→	(C)H ₃	0.40	0.00	100
	C-(C)H ₃	→	C-(C)H ₂	0.64	0.52	19
	2C-(C)H ₂	→	C-(C)H ₂	0.84	0.54	36
	3C-(C)H	→	2C-(C)H	1.18	0.88	25

Table 6-3. Coordination analysis of Ar deposition on PS

Energy	Initial coordination	Final coordination	Total yield	Surface yield	Dissociated (%)
25	-	→ -	-	-	-
50	2C-(C)H	→ 3C-(C)	0.12	0.12	0
	2C-(C)H ₂	→ C-(C)H ₂	0.16	0.12	25
	3C-(C)	→ C-(C)-C	0.26	0.20	23
	3C-(C)H	→ 2C-(C)H	0.28	0.22	21
100	2C-(C)H	→ C-(C)H	0.44	0.32	27
	2C-(C)H	→ (C)H	0.12	0.00	100
	2C-(C)H	→ C-(C)	0.12	0.04	67
	3C-(C)	→ 2C-(C)H	0.16	0.06	63
	3C-(C)H	→ C-(C)-C	0.18	0.08	56
	2C-(C)H	→ 2C-(C)H ₂	0.18	0.16	11
	2C-(C)H	→ C-(C)H ₂	0.18	0.16	11
	3C-(C)H	→ 3C-(C)	0.22	0.20	9
	2C-(C)H ₂	→ 2C-(C)H	0.24	0.18	25
	2C-(C)H	→ 3C-(C)	0.32	0.32	0
	2C-(C)H	→ C-(C)-C	0.54	0.42	22
	2C-(C)H ₂	→ C-(C)H ₂	0.58	0.32	45
	3C-(C)	→ C-(C)-C	0.58	0.36	38
	3C-(C)H	→ 2C-(C)H	1.00	0.70	30
	2C-(C)H	→ C-(C)H	1.96	0.66	66

Table 6-4. Coordination analysis of atomic oxygen deposition on PE at 25eV

Initial coordination	Final coordination	Total yield	Surface yield	Dissociated (%)
2C-(C)H ₂	→ C-(C)H ₂ -O	0.24	0.20	17
2C-(C)H ₂	→ C-(C)H-O	0.28	0.24	14
2C-(C)H ₂	→ 2C-(C)H	0.38	0.36	5
2C-(C)H ₂	→ C-(C)H ₂	0.68	0.48	29
O	→ H-(O)-H	0.02	0.00	100
O	→ O-(O)	0.02	0.02	0
O	→ C-(O)H	0.04	0.02	50
O	→ C-(O)-C	0.06	0.04	33
O	→ (O)H	0.08	0.00	100
O	→ C-(O)-O	0.10	0.06	40
O	→ C-(O)	0.52	0.44	15
O	→ O	0.16	0.00	100

Table 6-5. Coordination analysis of atomic oxygen deposition on PE at 50eV

Initial coordination	Final coordination	Total yield	Surface yield	Dissociated (%)
2C-(C)H ₂	→ O-(C)	0.12	0.02	83
2C-(C)H ₂	→ C-(C)H ₃	0.14	0.10	29
2C-(C)H ₂	→ C-(C)H ₂ -O	0.14	0.12	14
2C-(C)H ₂	→ 2C-(C)H-O	0.24	0.22	8
2C-(C)H ₂	→ C-(C)H-O	0.24	0.18	25
2C-(C)H ₂	→ C-(C)H	0.30	0.18	40
2C-(C)H ₂	→ 2C-(C)H	0.92	0.90	2
2C-(C)H ₂	→ C-(C)H ₂	1.10	0.88	20
O	→ OH	0.02	0.00	100
O	→ O-(O)H	0.04	0.02	50
O	→ H-O-H	0.06	0.00	100
O	→ C-(O)-C	0.14	0.12	14
O	→ C-(O)-O	0.16	0.10	38
O	→ C-(O)H	0.24	0.12	50
O	→ C-(O)	0.26	0.18	31
O	→ O	0.08	0.00	100

Table 6-6. Coordination analysis of atomic oxygen deposition on PE at 100eV

Initial coordination	Final coordination	Total yield	Surface yield	Dissociated (%)
2C-(C)H ₂	→ O-(C)H ₂	0.14	0.06	57
2C-(C)H ₂	→ C-(C)H-O	0.18	0.18	0
2C-(C)H ₂	→ C-(C)H ₂ -O	0.20	0.18	10
2C-(C)H ₂	→ 2C-(C)H-O	0.22	0.22	0
2C-(C)H ₂	→ C-(C)H ₃	0.40	0.36	10
2C-(C)H ₂	→ C-(C)-C	0.44	0.36	18
2C-(C)H ₂	→ C-(C)H	0.62	0.36	42
2C-(C)H ₂	→ C-(C)H ₂	1.46	0.86	41
2C-(C)H ₂	→ 2C-(C)H	2.34	2.12	9
O	→ H-(O)-H	0.04	0.00	100
O	→ (O)H	0.04	0.00	100
O	→ C-(O)-O	0.06	0.04	33
O	→ O-(O)H	0.06	0.04	33
O	→ C-(O)	0.18	0.04	78
O	→ C-(O)H	0.26	0.16	38
O	→ C-(O)-C	0.28	0.26	7
O	→ O	0.08	0.00	100

Table 6-7. Coordination analysis of atomic oxygen deposition on PP at 25eV

Initial coordination	Final coordination	Total yield	Surface yield	Dissociated (%)
3C-(C)H	→ 2C-(C)H-O	0.12	0.12	0
C-(C)H ₃	→ C-(C)H ₂	0.12	0.12	0
C-(C)H ₃	→ C-(C)H ₂ -O	0.16	0.16	0
2C-(C)H ₂	→ 2C-(C)H	0.22	0.22	0
3C-(C)H	→ 2C-(C)H	0.24	0.24	0
O	→ H-(O)-H	0.02	0.00	100
O	→ O-(O)	0.02	0.02	0
O	→ O-(O)H	0.04	0.02	50
O	→ C-(O)-C	0.06	0.06	0
O	→ (O)H	0.08	0.00	100
O	→ C-(O)H	0.10	0.10	0
O	→ C-(O)-O	0.14	0.12	14
O	→ C-(O)	0.44	0.34	23
O	→ O	0.10	0.00	100

Table 6-8. Coordination analysis of atomic oxygen deposition on PP at 50eV

Initial coordination	Final coordination	Total yield	Surface yield	Dissociated (%)
3C-(C)H	→ C-(C)H	0.12	0.04	67
C-(C)H ₃	→ O-(C)H ₂	0.12	0.04	67
3C-(C)H	→ 3C-(C)	0.14	0.14	0
2C-(C)H ₂	→ 2C-(C)H-O	0.16	0.14	13
C-(C)H ₃	→ C-(C)H ₂ -O	0.16	0.16	0
C-(C)H ₃	→ (C)H ₃	0.18	0.00	100
2C-(C)H ₂	→ C-(C)H ₂	0.18	0.18	0
3C-(C)H	→ 2C-(C)H	0.32	0.28	13
2C-(C)H ₂	→ 2C-(C)H	0.34	0.34	0
C-(C)H ₃	→ C-(C)H ₂	0.60	0.58	3
O	→ C-(O)H	0.08	0.04	50
O	→ H-(O)-H	0.10	0.00	100
O	→ (O)H	0.12	0.00	100
O	→ C-(O)-C	0.30	0.26	13
O	→ C-(O)	0.36	0.22	39
O	→ O	0.04	0.00	100

Table 6-9. Coordination analysis of atomic oxygen deposition on PP at 100eV

Initial coordination	Final coordination	Total yield	Surface yield	Dissociated (%)
C-(C)H ₃	→ (C)H ₃	0.12	0.00	100
3C-(C)H	→ 2C-(C)H ₂	0.14	0.10	29
2C-(C)H ₂	→ C-(C)H ₃	0.14	0.12	14
3C-(C)H	→ C-(C)-C	0.14	0.12	14
C-(C)H ₃	→ (C)H ₄	0.16	0.00	100
C-(C)H ₃	→ C-(C)H ₂ -O	0.18	0.18	0
C-(C)H ₃	→ C-(C)H	0.22	0.12	45
2C-(C)H ₂	→ C-(C)H	0.26	0.12	54
C-(C)H ₃	→ 2C-(C)H ₂	0.30	0.30	0
3C-(C)H	→ C-(C)H	0.30	0.12	60
2C-(C)H ₂	→ C-(C)H ₂	0.48	0.36	25
3C-(C)H	→ 3C-(C)	0.50	0.44	12
2C-(C)H ₂	→ 2C-(C)H	0.80	0.74	8
3C-(C)H	→ 2C-(C)H	1.00	0.82	18
C-(C)H ₃	→ C-(C)H ₂	1.12	1.02	9
O	→ OH	0.02	0.00	100
O	→ H-(O)-H	0.04	0.00	100
O	→ O-(O)	0.04	0.00	100
O	→ C-(O)-C	0.20	0.14	30
O	→ C-(O)	0.30	0.12	60
O	→ C-(O)H	0.32	0.20	38
O	→ O	0.08	0.00	100

Table 6-10. Coordination analysis of atomic oxygen deposition on PS at 25eV

Initial coordination	Final coordination	Total yield	Surface yield	Dissociated (%)
2C-(C)H	→ C-(C)-C	0.12	0.12	0
2C-(C)H ₂	→ C-(C)H ₂	0.16	0.12	25
3C-(C)H	→ 2C-(C)H	0.22	0.18	18
2C-(C)H	→ C-(C)H	0.52	0.38	27
2C-(C)H	→ C-(C)H-O	0.56	0.48	14
2C-(C)H	→ 2C-(C)H-O	0.64	0.60	6
O	→ C-(O)H	0.04	0.04	0
O	→ C-(O)	0.14	0.08	43
O	→ C-(O)-C	0.82	0.74	10

Table 6-11. Coordination analysis of atomic oxygen deposition on PS at 50eV

Initial coordination	Final coordination	Total yield	Surface yield	Dissociated (%)
3C-(C)	→ 3C-(C)-O	0.12	0.10	17
2C-(C)H ₂	→ 2C-(C)H	0.12	0.12	0
2C-(C)H	→ C-(C)H ₂	0.12	0.12	0
3C-(C)	→ 2C-(C)-O	0.14	0.06	57
3C-(C)H	→ 3C-(C)	0.20	0.20	0
2C-(C)H ₂	→ C-(C)H ₂	0.22	0.20	9
3C-(C)	→ C-(C)-C	0.22	0.18	18
2C-(C)H	→ C-(C)H-O	0.34	0.26	24
3C-(C)H	→ 2C-(C)H	0.34	0.32	6
2C-(C)H	→ C-(C)-C	0.46	0.44	4
2C-(C)H	→ C-(C)H	0.60	0.44	27
2C-(C)H	→ 2C-(C)H-O	0.60	0.56	7
O	→ C-(O)	0.10	0.06	40
O	→ C-(O)H	0.14	0.10	29
O	→ C-(O)-C	0.76	0.60	21

Table 6-12. Coordination analysis of atomic oxygen deposition on PS at 100eV

Initial coordination	Final coordination	Total yield	Surface yield	Dissociated (%)
2C-(C)H	→ C-C	0.12	0.02	83
2C-(C)H	→ 3C-(C)H	0.18	0.18	0
3C-(C)H	→ C-(C)-C	0.20	0.10	50
3C-(C)	→ 2C-(C)H	0.20	0.14	30
2C-(C)H	→ C-(C)H ₂	0.22	0.20	9
2C-(C)H	→ C-(C)H-O	0.28	0.28	0
3C-(C)	→ C-(C)-C	0.38	0.36	5
2C-(C)H	→ 3C-(C)	0.40	0.38	5
3C-(C)H	→ 3C-(C)	0.42	0.40	5
2C-(C)H ₂	→ C-(C)H ₂	0.50	0.26	48
2C-(C)H ₂	→ 2C-(C)H	0.54	0.54	0
2C-(C)H	→ 2C-(C)H ₂	0.64	0.64	0
2C-(C)H	→ 2C-(C)H-O	0.68	0.68	0
3C-(C)H	→ 2C-(C)H	0.82	0.70	15
2C-(C)H	→ C-(C)-C	0.96	0.94	2
2C-(C)H	→ C-(C)H	1.60	0.86	46
O	→ C-(O)	0.06	0.02	67
O	→ C-(O)H	0.10	0.10	0
O	→ C-(O)-C	0.84	0.80	5

Table 6-13. Comparison of probable modifications during argon and atomic oxygen bombardment at 100eV

Molecule	Initial coordination	Final coordination	Ar		O	
			Total yield	Surface yield	Total yield	Surface yield
PE	2C-CH ₂ →	2C-CH	1.44	1.32	2.34	2.12
	2C-CH ₂ →	C-CH ₂	2.48	1.62	1.46	0.86
PP	C-CH ₃ →	C-CH ₂	0.64	0.52	1.12	1.02
	3C-CH →	2C-CH	1.18	0.88	1.00	0.82
PS	2C-CH →	C-C-C	0.54	0.42	0.96	0.94
	3C-CH →	2C-CH	1.00	0.70	0.82	0.70
	3C-C →	C-C-C	0.58	0.36	0.38	0.36
	2C-CH →	C-CH	1.96	0.66	1.60	0.86

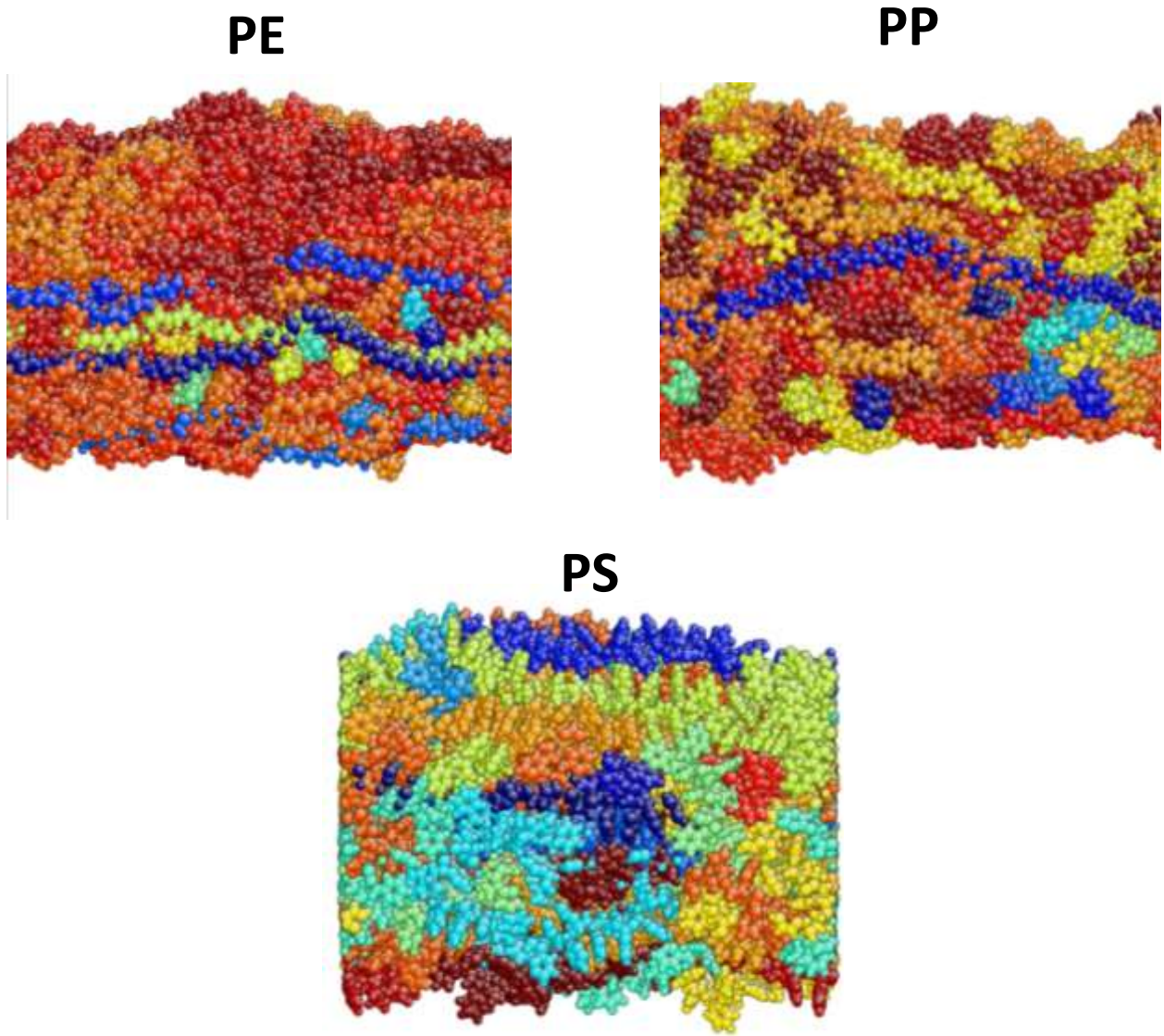


Figure 6-1. Initial PE, PP, PMMA and PS substrates with each chain color coded

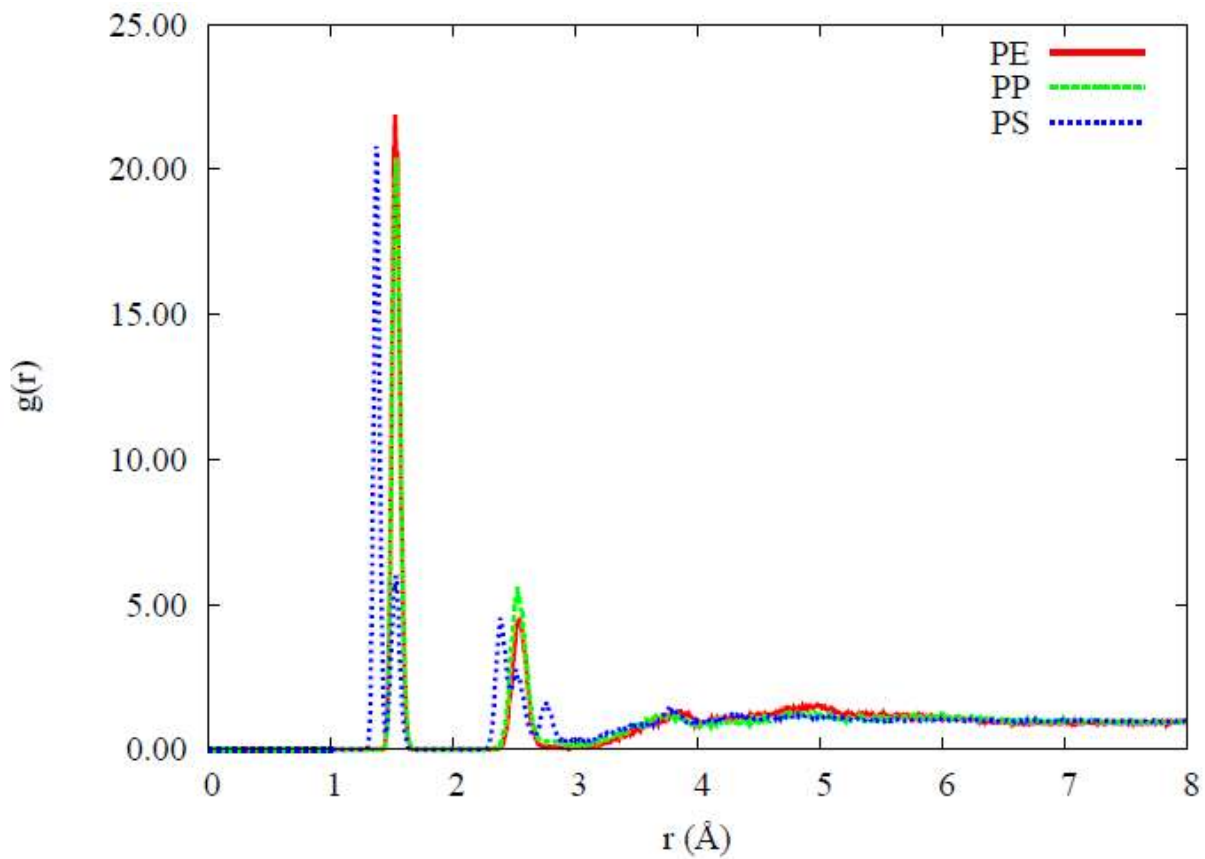


Figure 6-2. Pair distribution function for PE, PP and PS

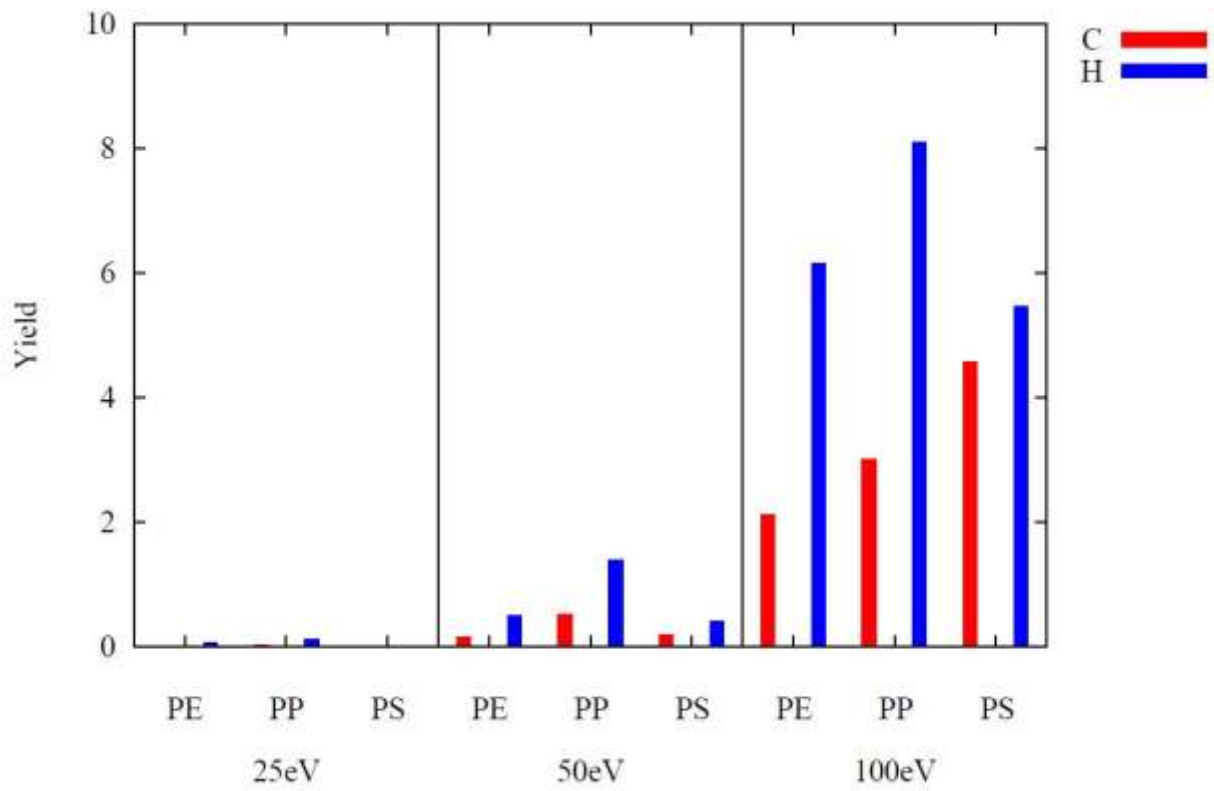


Figure 6-3. Yield of sputtered carbon and hydrogen atoms for *Ar* at 25eV, 50eV and 100eV

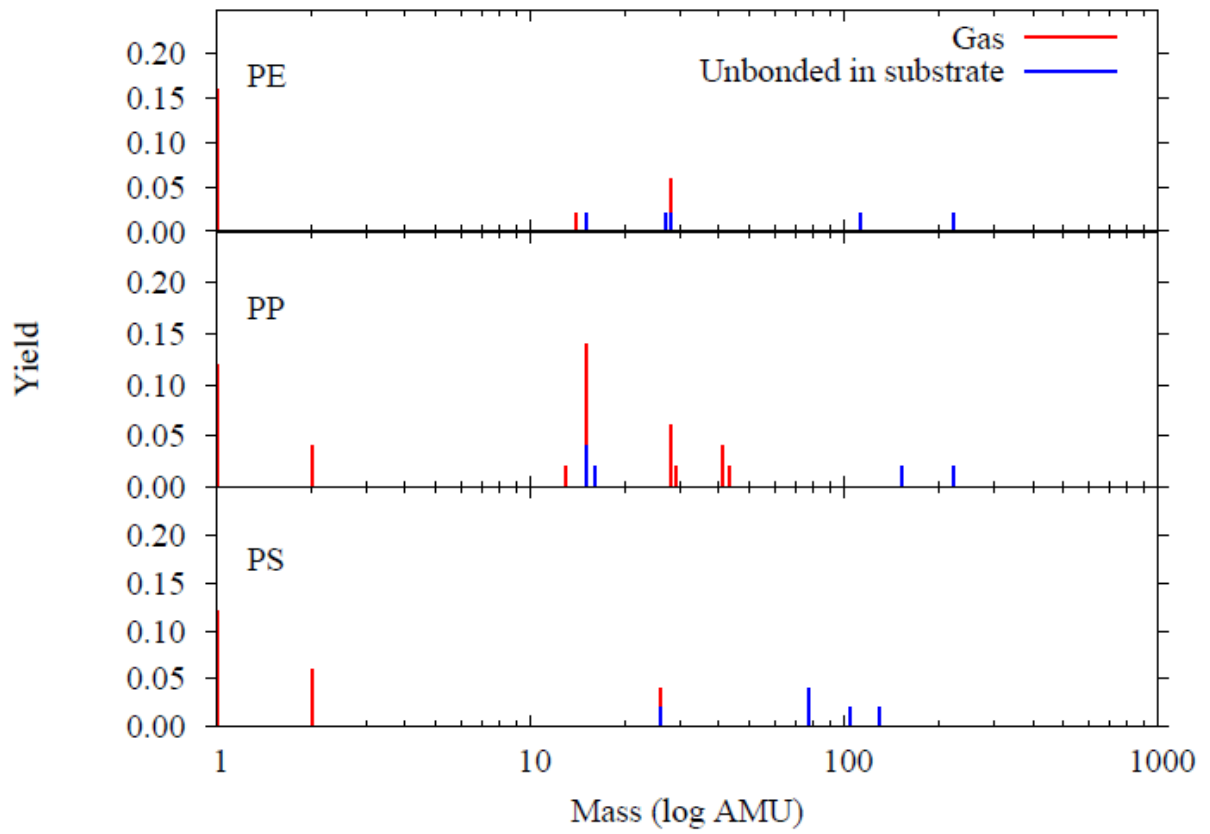


Figure 6-4. Molecular mass analysis for Ar deposited at $50eV$

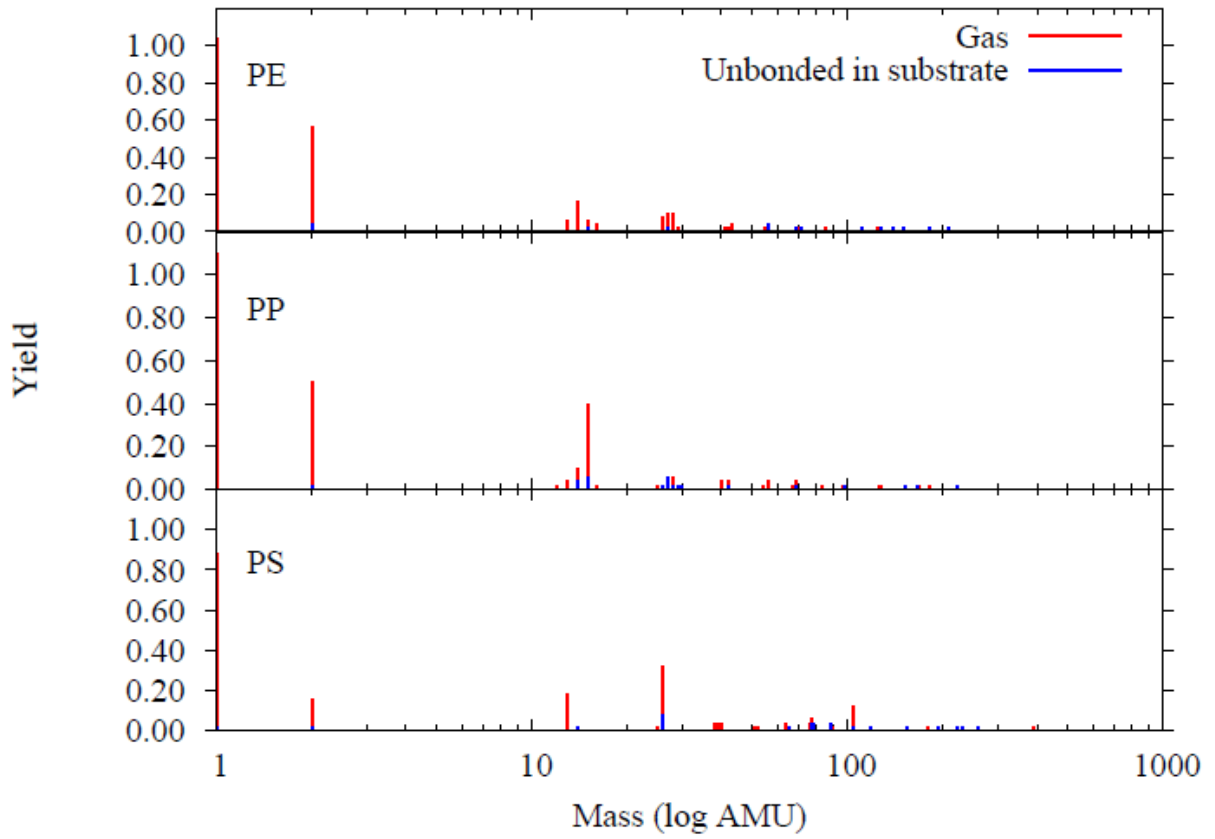


Figure 6-5. Molecular mass analysis for Ar^+ deposited at $100eV$

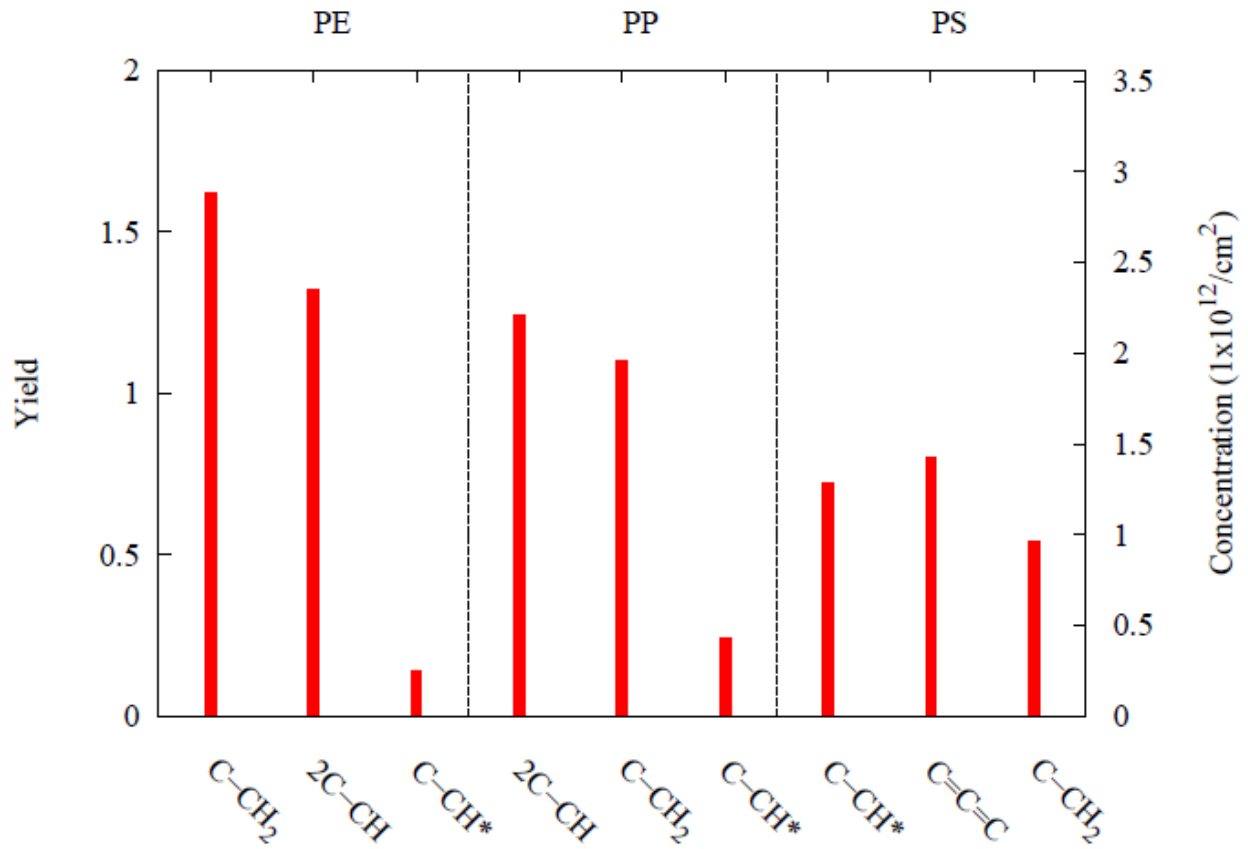


Figure 6-6. Yields and concentrations of the three most probable groups formed during 100eV Ar deposition on PE, PP and PS

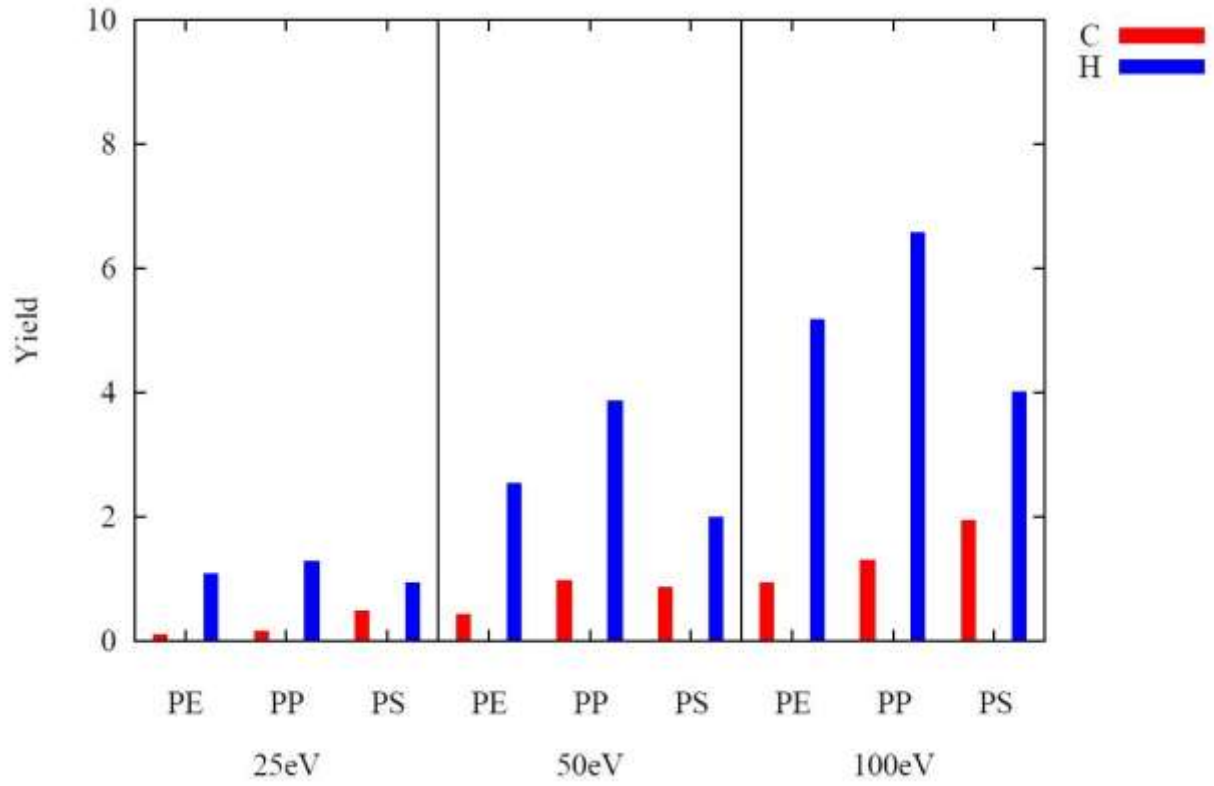


Figure 6-7. Yield of sputtered carbon and hydrogen for atomic oxygen at 25eV, 50eV and 100eV.

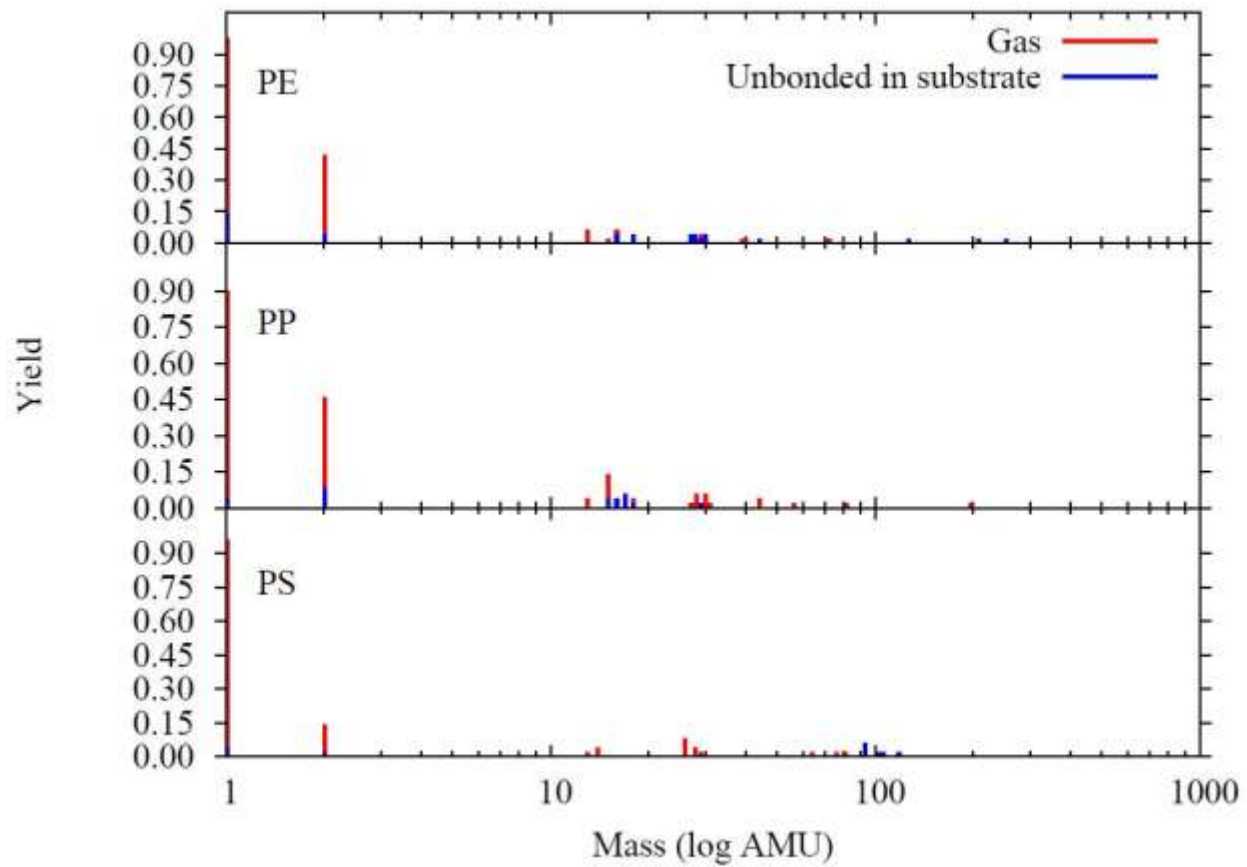


Figure 6-8. Molecular mass analysis of 50eV atomic oxygen

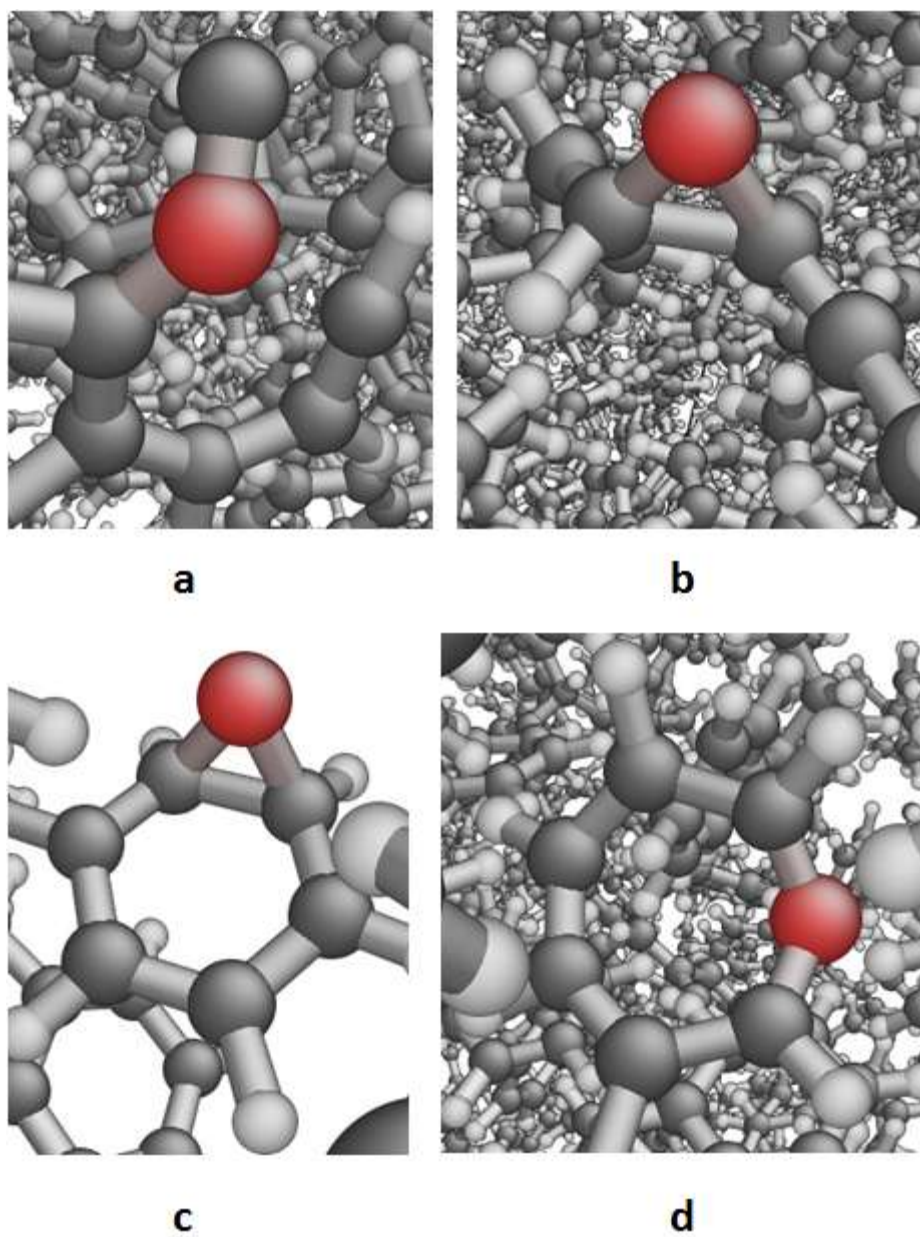


Figure 6-9. Oxygen bonding in PS for deposition energies at 25eV with C-(O)-C coordination in four possible environments: a) in broken ring, b) along broken ring, c) bridge on ring and d) in ring

CHAPTER 7 DEVELOPMENT OF HfO_2 POTENTIALS

A key aspect of today's logic and memory applications is the metal oxide semiconductor (MOS) stack. MOS technology has matured over decades of intense research making it one of the most studied systems. However, a seminal shift is occurring in this industry, with the use of SiO_2 as an insulating oxide having reached its limit. This is a result of device scaling, necessitating a detrimentally thin SiO_2 layer, which allows an unacceptable amount of leakage current through the insulating oxide¹⁶³. The adoption of a new oxide material with a higher dielectric constant or "high- κ " material, introduces interfacial issues such as defect states, which can trap electrons, as well as unwanted SiO_2 formation^{164, 165}. Despite these on-going issues hafnium dioxide has emerged as the new "high- κ " material. While there has been a recent surge in experimental and quantum computation studies of this material, there exists ample room for further exploration of hafnium dioxide.

Hafnium dioxide (HfO_2) has become the favored material for use as a dielectric layer in MOS applications; due to it meeting a number of performance metrics, including a high dielectric constant of ~ 25 , a large band gap of $5.8eV$ and conduction band offset of $1.3eV$ with respect to Si ^{164, 165}. HfO_2 is also thermodynamically stable in the presence of silicon, neither reacting or decomposing under annealing conditions^{164, 165}. With increasing temperature, HfO_2 exhibits three crystalline phases monoclinic $P21/c$, tetragonal $P42/nmc$, cubic $Fm\bar{3}m$ ¹⁶⁶. This is the same phase order as in zirconia. This is not surprising, as Zr and Hf occupy the same column of the periodic table.

7.1 Density Functional Theory Data

In the absence of a full database for the salient materials properties, electronic-structure calculations are used, at the density functional theory (DFT) level to provide the necessary materials properties to fit potential parameters. In particular, DFT is used to calculate the elastic properties for the cubic and tetragonal phases, and point defect formation energies the cubic phase.

Calculations are conducted using the VASP software^{99, 100}. The exchange and correlation terms are calculated using the generalized gradient approximation (GGA)^{102, 103} with the correction of Perdew, Burke and Ernzerhof (PBE)¹⁰⁴. The electron wavefunctions are calculated using projected augmented wave (PAW) pseudopotentials¹⁰¹. The Monkhorst-Pack method of k-point meshing is employed¹⁶⁷; for the single non-primitive unit cells used in this study. A 6x6x6 k-point mesh is found to give well converged results. The conjugant gradient method of geometry optimization is used. The valence electron orbitals for hafnium include the 5*d*, 6*s* and 5*p* orbitals, while the 2*s* and 2*p* electron orbitals are considered for oxygen. A cut-off energy of 525*eV* is used for the elastic constant calculations. Defect formation energies are calculated using 2x2x2 non-primitive unit cells.

7.2 Buckingham With Core Shell

A popular and successful empirical potential for the interatomic interactions for ionic materials is the Buckingham potential, Equation (2-7), used either with or without a shell model Equation (2-8). This potential can be seen to depend on empirical parameters (A_{ij} , ρ_{ij} , C_{ij} and k) that are fit empirically to achieve the desired set of properties. To determine the parameters, a set of properties from either experiment or first principles is specified, such as the equation of state and the elastic constants. The

set of properties predicted by the potential is then compared to the target set of properties, and a least-squared method routine is used to minimize the error of these properties in parameter space. Considering the lack of experimental data on the high temperature phases of HfO_2 , first principles methods are needed to achieve a full set of properties in order to parameterize a potential.

7.3 Empirical Potential for HfO_2

In this section, three different potentials are parameterized. One is optimized for the cubic phase (1), one for the tetragonal phase (2) and one for both tetragonal and cubic phases (3). The potentials developed for the two phases separately reproduce more quantitatively the physical properties of the individual phase. The potential that reproduces both the tetragonal and cubic phases inevitably has to make compromises in its ability to capture the materials properties of both phases.

Based on the values calculated with DFT the lattice parameters and elastic constant, parameter sets for the cubic and tetragonal phases are fitted for the Buckingham potential using the generalized lattice parameter software (GULP)¹⁶⁸. The resulting parameter sets are shown in Table 7-1, where A_{ij} , ρ_{ij} and C_{ij} are the atomic interaction parameters, r_{cut} is the distance after which no interatomic interaction is considered (cut off), k_α is the spring constant and Y_α is the shell charge.

7.4 Structure and Phase order

In order to check the phase stability each phase of HfO_2 is explored, as indicated in Figure 7-1, and the structural properties are summarized in Table 7-2. The Buckingham form is not able to describe the monoclinic phase. This is not a surprise since attempts to describe monoclinic zirconia in this manner have not been successful.

7.4.1 Elastic Properties

The two high dielectric constant phases of interest for MOS applications, the cubic and tetragonal phases, are further analyzed using DFT. The elastic coefficients for these phases are calculated by applying strains under $\pm 1\%$; the results are given in Table 7-3 together with the elastic constant calculated for the potentials.

The compliance tensor is found by calculating the inverse of the elastic coefficient tensor. Then the Reuss and Voigt approximations are used to calculate the bulk (B) and shear (G) moduli¹⁶⁹. For an isotropic solid (cubic) single crystal the bulk and shear moduli can be found to be:

$$B_o = \frac{1}{3}(C_{11} + 2C_{12}), \quad (7-1)$$

$$G_{Voigt} = \frac{C_{11} - C_{12} + 3C_{44}}{5}, \quad (7-2)$$

and

$$G_{Reuss} = \frac{5}{4(S_{11} - S_{12}) + 3S_{44}}. \quad (7-3)$$

Where the Voigt and Reuss approximations uses the elastic coefficients and compliance respectively. For tetragonal symmetry these approximations are as follows:

$$B_{Voigt} = \frac{(2C_{11} + C_{33}) + 2(C_{12} + 2C_{13})}{9} \quad (7-4)$$

and

$$B_{Reuss} = \frac{1}{(2S_{11} + C_{33}) + 2(S_{12} + 2C_{13})} \quad (7-5)$$

for the bulk modulus, and

$$G_{Voigt} = \frac{1}{15}(2C_{11} + C_{33} - C_{12} - 2C_{13}) + \frac{1}{5}(2C_{44} + C_{66}) \quad (7-6)$$

and

$$G_{Reuss} = \frac{15}{4(2S_{11} - S_{33}) - 4(S_{12} - 2S_{13}) + 3(2S_{44} + S_{66})} \quad (7-7)$$

for the shear modulus. The Hill approximation is found by averaging the Reuss and Voigt approximations¹⁶⁹ and the Poisson's ratio and Young's modulus is approximated using the Hill values¹⁷⁰:

$$\nu = \frac{\left(B_H - \frac{2}{3}G_H\right)}{2\left(B_H - \frac{1}{3}G_H\right)} \quad (7-8)$$

and

$$E = \frac{9B_H}{\left(1 + \frac{3B_H}{G_H}\right)}. \quad (7-9)$$

and the results are summarized in Table 7-4.

7.5 Point Defect Energetics

For a charge neutral system, the formation of an oxygen vacancy creates a defect site with a 2+ charge, along with two unpaired electrons:



In contrast, the formation of a hafnium vacancy leaves a defect site with a 4 – charge and four holes:

$$null \Rightarrow V_{Hf}'''' + 4h^\bullet \quad (7-11)$$

An interstitial oxygen has a charge of 2- requiring two holes to be neutral and an interstitial hafnium has a charge of 4+ requiring four electrons to be neutral.

$$null \Rightarrow O_i'' + 2h^\bullet \quad (7-12)$$

and

$$null \Rightarrow Hf_i'''' + 4e' \quad (7-13)$$

DFT is used to calculate the appropriate range of formation energies of these point defects for limiting cases of the chemical potential¹⁷¹. The formation of these defects is defined by

$$\Delta E_{form} = E_{def} - E_{perf} \pm \mu_\alpha + q\varepsilon_F \quad (7-14)$$

where E_{perf} is energy of the perfect crystal, E_{def} is the energy of the defective system, μ_α is the chemical potential of the defective species α , q is the charge of the defect and ε_F is the Fermi energy. The range of the chemical potentials is defined first by the stability of the oxide phase compared to the metallic and molecular phases of its constituents. In particular, the chemical potential of Hf in HfO_2 must be less than that of Hf in its hcp metal phase:

$$\mu_{Hf}^{HfO_2} < \mu_{Hf}^{Metal} \quad (7-15)$$

Correspondingly, the chemical potential of oxygen in hafnium oxide must be less than that of oxygen in the molecular phase for the oxide to be stable:

$$\mu_{O}^{HfO_2} < \frac{1}{2} \mu_{O_2}^{gas} \quad (7-16)$$

The second limiting factor of the species' chemical potential is the enthalpy of formation, ΔH where:

$$\Delta H_{oxide}^{HfO_2} = \mu_{Hf}^{HfO_2} - \mu_{Hf}^{Metal} + 2\mu_{O}^{HfO_2} - \mu_{O_2}^{gas} \quad (7-17)$$

If the first limit of the *Hf* chemical (Equation (7-15)) is considered, then the chemical potential of oxygen in HfO_2 is given as:

$$\frac{1}{2} \Delta H_{oxide}^{HfO_2} + \frac{1}{2} \mu_{O_2}^{gas} < \mu_{O}^{HfO_2} \quad \text{if} \quad \mu_{Hf}^{Metal} = \mu_{Hf}^{HfO_2} \quad (7-18)$$

In contrast, if the first limit of the chemical potential of oxygen is considered:

$$\Delta H_{oxide}^{HfO_2} + \mu_{Hf}^{Metal} < \mu_{Hf}^{HfO_2} \quad \text{if} \quad 2\mu_{O}^{HfO_2} = \mu_{O_2}^{gas} \quad (7-19)$$

From Equation (7-17) the enthalpy of formation is calculated to be $-10.55eV$ and $-10.45eV$ per stoichiometric unit for the tetragonal and cubic phases, respectively. In order to properly represent isolated point defects a $2 \times 2 \times 2$ super cell consisting of 96 atoms are created. Then single oxygen and hafnium vacancies and interstitial point defects were added. These systems were relaxed with a fixed volume, convergence criteria in energy of $0.1 meV$ and force of $0.02 eV/\text{\AA}$. Using Equation 7-14, the formation energies are calculated for point defects using the two chemical potential extremes, and the results are shown in Table 7-5.

The defect formation energies are also calculated using the fitted empirical potentials. Defective $4 \times 4 \times 4$ super cells are constructed and relaxed at constant volume. However, with this method the chemical potential of the constituent species is considered to be the average potential energy associated with the relative element within the oxide system. The results of these calculations are also shown in Table 7-5.

7.6 Conclusions

While the elastic and phase order properties are accurately captured in the fitting, the cubic and tetragonal phases are found to be unstable at temperatures above 0K. Therefore, the potential is not considered to be a successful way to model hafnium oxide in classical molecular dynamics simulations.

Table 7-1. Empirical potential parameters of the cubic and tetragonal phases of HfO_2 , using the Buckingham formalism with shell model

Parameters	Cubic (1)	Tetragonal (2)	Cubic/Tetragonal (3)
A_{O-O} (eV)	9547.96	9547.96	9547.96
ρ_{O-O} (Å)	0.24	0.27	0.26
C_{O-O} (eV·Å ⁶)	170.45	347.94	259.20
A_{Hf-O} (eV)	1201.34	975.19	928.75
ρ_{Hf-O} (Å)	0.39	0.38	0.39
C_{Hf-O} (eV·Å ⁶)	113.22	0.00	6.00
r_{cut} (Å)	12.00	12.00	12.00
k_{Hf}	34.21	34.21	34.21
k_O	28.80	28.80	28.80
Y_{Hf} (e)	3.95	3.95	3.95
Y_O (e)	-2.20	-2.20	-2.20

Table 7-2. Experimental and calculated lattice parameters of the monoclinic, tetragonal and cubic phases of HfO_2

		DFT (PBE)	Potentials 1 or 2	Potential 3	Expt ¹⁶⁹
Tetragonal	V (Å ³)	33.73	33.68	34.38	33.58
	a (Å)	5.08	5.08	5.11	5.09
	c (Å)	5.23	5.23	5.26	5.18
	ρ (g/cm ³)	10.36	10.38	10.17	10.41
Cubic	V (Å ³)	32.65	32.53	33.87	32.77
	a (Å)	5.07	5.07	5.14	5.08
	ρ (g/cm ³)	10.70	10.74	10.32	10.67

Table 7-3. Elastic constant tensor values for the tetragonal and cubic phases

	Coefficient (GPa)	DFT (PBE)	Potential	
			1 or 2	Potential 3
Tetragonal	C ₁₁	495.01	625.56	579.81
	C ₁₂	151.77	150.36	145.48
	C ₁₃	118.76	124.34	117.02
	C ₃₃	397.42	422.20	361.98
	C ₄₄	89.86	89.41	87.99
	C ₆₆	125.12	129.57	121.95
Cubic	C ₁₁	560.36	561.19	664.56
	C ₁₂	93.20	94.15	111.13
	C ₄₄	67.82	68.66	98.43

Table 7-4. Elastic moduli for the cubic and tetragonal phases of HfO₂

	Cubic			Tetragonal		
	DFT	Potential 1	Potential 3	DFT	Potential 2	Potential 3
G	114.32	115.14	151.18	122.81	136.05	127.39
B	248.92	249.83	295.61	245.33	269.39	246.54
v	0.30	0.30	0.28	0.29	0.28	0.28
E	297.43	299.42	387.48	315.75	349.34	326.01

Table 7-5. Defect formation energies from DFT and empirical potential calculations

	Kröger-Vink notation	Defect charge	Potentials		1&2	3
			$\mu_{\text{Hf}} = \mu^{\text{Metal}}_{\text{Hf}}$	$\mu_{\text{O}} = 1/2\mu^{\text{Molec}}_{\text{O}_2}$		
Tetragonal	V_{O}^{\times}	0	0.79	6.07	-	-
	$V_{\text{O}}^{\bullet\bullet}$	+2	-4.04	1.23	2.67	0.30
	V_{Hf}^{\times}	0	16.28	5.73	-	-
	$V_{\text{Hf}}^{\bullet\bullet\bullet\bullet}$	-4	12.00	1.45	9.65	10.74
	O_{i}^{\times}	0	7.54	2.26	-	-
	$O_{\text{i}}^{\bullet\bullet}$	-2	7.06	1.78	3.79	5.62
	$\text{Hf}_{\text{i}}^{\times}$	0	4.66	15.21	-	-
	$\text{Hf}_{\text{i}}^{\bullet\bullet\bullet\bullet}$	+4	-4.41	6.14	6.65	8.14
Cubic	V_{O}^{\times}	0	0.82	6.05	-	-
	$V_{\text{O}}^{\bullet\bullet}$	+2	-5.97	-0.17	-2.38	-1.19
	V_{Hf}^{\times}	0	15.01	4.56	-	-
	$V_{\text{Hf}}^{\bullet\bullet\bullet\bullet}$	-4	14.56	2.97	9.65	11.97
	O_{i}^{\times}	0	9.35	4.13	-	-
	$O_{\text{i}}^{\bullet\bullet}$	-2	9.32	7.89	5.84	7.05
	$\text{Hf}_{\text{i}}^{\times}$	0	3.98	14.43	-	-
	$\text{Hf}_{\text{i}}^{\bullet\bullet\bullet\bullet}$	+4	-5.41	6.17	8.49	11.32

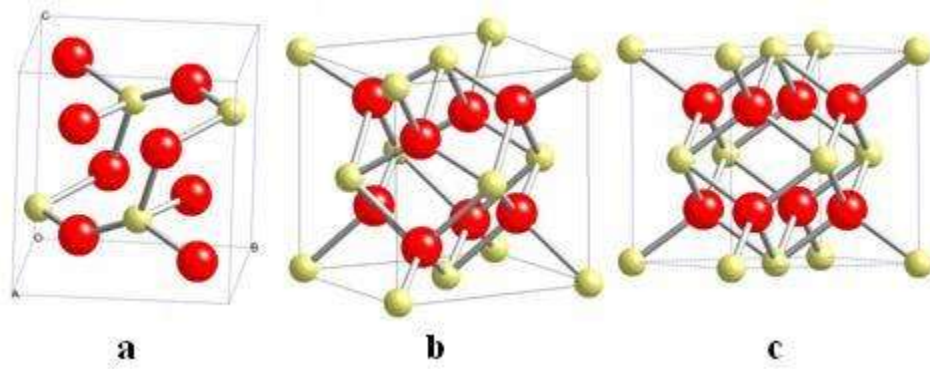


Figure 7-1. Three low pressure phases of HfO₂ (a) monoclinic, (b) tetragonal, (c) cubic where oxygen is darkly shaded and hafnium is lightly shaded

CHAPTER 8 CONCLUSIONS

The primary focus of the work described in this dissertation is to identify the interactions of hyperthermal ions with polymer surfaces. A combination of empirical potential MD simulations and quantum chemical analysis is used to classify the effects of individual ions on polymer surfaces. This method is successfully applied to illuminate fluorocarbon growth of DLC, hydrocarbon modification of PS, the modification of terthiophene during the SPIAD process, and the effects of non-reactive and reactive species on PE, PP and PS.

In order to study these processes the second generation REBO potential is modified to include sulfur hydro-carbon interactions, and improve the oxygen hydrocarbon interactions. In particular, the oxygen hydrocarbon second generation REBO potential is improved by refitting the coordination function. The refit primarily involved fitting to dissociation and atomization energies of an expanded dataset of small molecules that capture all possible coordination. The refit of the coordination function improved the average error in dissociation energy from 23% to 16% for the dataset; however, the average error in atomization energy for a test set is increased from 3% to 4.2%.

The sulfur interactions are included in a similar manner as oxygen. The pair terms are fit to molecular bond stretching and solid strain curves. The angular function is fit to bond bending curves, and given a dependence on the considered atom types. As with the oxygen coordination function, the sulfur coordination function is fit to a dataset of small molecule dissociation and atomization energies. The average error in dissociation energies is predicted to be 14%, and the average error in atomization energy to be 3%.

The multilevel simulation study of fluorocarbon growth of DLC carbon revealed that the creation of HF may be a key driving force allowing the process to occur at lower temperatures than hydrocarbon growth. The second generation REBO potential is used as an initial guide to probable reactions. DFT-MD simulations offer complementary analysis. Subsequent reactions are further analyzed with quantum chemical methods.

Hydrocarbon interactions with PS are investigated with computational simulations. It is found that the cations H and C_2H have barrier less interactions with the styrene ring of PS. This results correspond well to MD simulations using the second generation REBO potential, which finds non preferential bond to occur. The reaction path and subsequent barriers of the CH_2 radical bonding to the styrene ring is found to depend on the spin state. However, the final product, a methyl group, is found to be stable for both states. The reaction is also observed during the MD simulations.

The difference in the nature of argon and polyatomic thiophene depositions is explored during the SPIAD modification of terthiophene. MD simulations using the newly parameterized REBO potential for sulfur hydrocarbon interactions are conducted in conjunction with ab-initio calculations. The thiophene is seen to induce fracture of terthiophene rings while retaining the chemical structure of terthiophene. Conversely, argon is found to alter the number of carbons within the terthiophene during modification.

Thiophene is also predicted to produce more reactive species than argon. Reactive hydrocarbon species interacting with a thiophene radical are modeled with quantum chemical methods. These calculations find that thiophene radical readily reacts with small hydrocarbon molecules. Finally, the SPAID process is found to a

complex interaction involving dissociation of the incident polyatomic molecule, multiple reactions involving ring fragmentation, and likely recombination with other incident 3T molecules.

In order to compare the effect of non-reactive and reactive species on polymer surfaces, argon and atomic oxygen are deposited on PE, PP and PS. The primary modifications of each species is identified. Argon is found to break carbon-carbon bonds, and remove hydrogen as a secondary process. Atomic oxygen is found to remove hydrogen from the polymer, and form chemical bonds within the polymer. The scission of carbon-carbon bonds is also found to occur with less frequency for oxygen deposition than argon deposition.

Lastly, this work illuminates the nature of the of the hyperthermal ion with polymer surfaces. To this end, empirical potentials are developed and implement in order to identify relevant processes. These processes are further analyzed with quantum chemical methods. This work will thus foster further development of plasma and ion-beam methods to modify polymer surfaces.

REFERENCE LIST

- 1 J. P. Hirvonen, Jervis, T.R. and Nastasi, M., *Excimer laser surface modification : Process and properties* (United States. Dept. of Defense, Washington, D.C, 1992).
- 2 H. O. Pierson, (William Andrew Publishing/Noyes, 1999).
- 3 J. M. a. J. H. Michael Nastasi, *Ion-Solid Interactions : Fundamentals and Applications* (Press Syndicate of the University of Cambridge, New York, 1996).
- 4 F. F. Chen, Chang, Jane P., *Lecture Notes on Principles of Plasma Processing* (Kluwer Academic/ Plenum Publishers, New York, 2003).
- 5 R. D'Agostino, P. Favia, C. Oehr, and M. R. Wertheimer, *Plasma Process. Polym.* **3**, 9 (2006).
- 6 A. Chapiro, *Nucl. Instrum. Methods Phys. Res. Sect. B-Beam Interact. Mater. Atoms* **32**, 111 (1988).
- 7 D. Hegemann, U. Schütz, and C. Oehr, in *Plasma Process. Polym.* (Wiley-VCH Verlag GmbH & Co. KGaA, 2005), p. 23.
- 8 A. Martínez-García, A. Segura-Domingo, A. Sánchez-Reche, and S. Gisbert-Soler, *Treatment of Flexible Polyethylene with Low-Pressure Plasma to Improve its Painting Properties* (Wiley-VCH Verlag GmbH & Co. KGaA, 2005).
- 9 A. B. Ortiz-Magán, M. M. Pastor-Blas, and J. M. Martín-Martínez, *Different Performance of Ar, O2 and CO2 RF Plasmas in the Adhesion of Thermoplastic Rubber to Polyurethane Adhesive* (Wiley-VCH Verlag GmbH & Co. KGaA, 2005).
- 10 S. T. a. G. C. Charef Harrats, *Micro- and Nanostructured Multiphase Polymer Blend Systems* (CRC Press Taylor & Francis Group, Boca Raton, 2006).
- 11 M. Stamm, *Polymer Surfaces and Interfaces* (Springer, Verlag Berlin Heidelberg, 2008).
- 12 J. Friedrich, G. Kühn, and R. Mix, *Polymer Surface Modification with Monofunctional Groups of Different Type and Density* (Wiley-VCH Verlag GmbH & Co. KGaA, 2005).
- 13 S. Kodama and H. Sekiguchi, *Introduction of Acidic Functional Groups onto the Surface of Activated Carbons by Atmospheric-Pressure Nonthermal Plasma* (Wiley-VCH Verlag GmbH & Co. KGaA, 2005).

- 14 F. Rossi, R. De Mitri, S. Bobin, and R. Eloy, *Plasma Sterilisation: Mechanisms Overview and Influence of Discharge Parameters* (Wiley-VCH Verlag GmbH & Co. KGaA, 2005).
- 15 L. Detomaso, R. Gristina, G. S. Senesi, L. C. Lopez, P. Favia, and R. d'Agostino, *Plasma-Deposited Acrylic Acid Coatings on Flat and Nanostructured Substrates for Cell-Culture Experiments* (Wiley-VCH Verlag GmbH & Co. KGaA, 2005).
- 16 M. Smith, *Practical Applications of Plasma Surface Modification* (AtlliedSignal inc., Las Vegas, 1993).
- 17 K. S. Siow, L. Britcher, S. Kumar, and H. J. Griesser, *Plasma Process. Polym.* **3**, 392 (2006).
- 18 D. R. McKenzie, K. Newton-McGee, P. Ruch, M. M. Bilek, and B. K. Gan, *Surf. Coat. Technol.* **186**, 239 (2004).
- 19 B. J. Schwartz, *Annu. Rev. Phys. Chem.* **54**, 141 (2003).
- 20 R. P. Hippler, Sigismund; Schmidt, Martin; Schoenbach, Karl H., *Low Temperature Plasma Physics: Fundamental Aspects and Applications* (Wiley-VCH Berlin, 2001).
- 21 *Handbook of Plasma Processing Technology Fundamentals, Etching, Deposition, and Surface Interactions* (Noyes Publications, New Jersey, 1990).
- 22 Manos, in *Plasma Etching* edited by D. M. M. a. D. L. Flamm (Academic Press, Inc., San Diego, 1989).
- 23 K. Kurihara, A. Egami, and M. Nakamura, *Journal of Vacuum Science & Technology A: Vacuum, Surfaces, and Films* **24**, 286 (2006).
- 24 R. S. Butter, D. R. Waterman, A. H. Lettington, R. T. Ramos, and E. J. Fordham, *Thin Solid Films* **311**, 107 (1997).
- 25 H. Biederman, *Plasma Polymer Films* (Imperial College Press, 2004).
- 26 K. Endo, K. Shinoda, and T. Tatsumi, *J. Appl. Phys.* **86**, 2739 (1999).
- 27 D. Haefliger, M. Nordström, P. A. Rasmussen, and A. Boisen, *Microelectronic Engineering* **78-79**, 88 (2005).
- 28 F. Hentschel, I. Schmidt, and C. Benndorf, *Thin Solid Films* **291**, 196 (1996).
- 29 A. M. Ektessabi and K. Yamaguchi, *Thin Solid Films* **377**, 793 (2000).

- 30 S. Tepavcevic, Y. Choi, and L. Hanley, *J. Am. Chem. Soc.* **125**, 2396 (2003).
- 31 Y. S. Choi, S. Tepavcevic, Z. Xu, and L. Hanley, *Chem. Mat.* **16**, 1924 (2004).
- 32 J. Jang, in *Emissive Materials: Nanomaterials* (Springer-Verlag Berlin, Berlin, 2006), Vol. 199, p. 189.
- 33 Y. Choi, A. Zachary, S. Tepavcevic, C. P. Wu, and L. Hanley, *Int. J. Mass Spectrom.* **241**, 139 (2005).
- 34 S. A. Miller, H. Luo, S. J. Pachuta, and R. G. Cooks, *Science* **275**, 1447 (1997).
- 35 V. Grill, J. Shen, C. Evans, and R. G. Cooks, *Rev. Sci. Instrum.* **72**, 3149 (2001).
- 36 B. J. Garrison, P. B. S. Kodali, and D. Srivastava, *Chem. Rev.* **96**, 1327 (1996).
- 37 D. W. Brenner, *Phys. Rev. B* **42**, 9458 (1990).
- 38 D. W. Brenner, O. A. Shenderova, J. A. Harrison, S. J. Stuart, B. Ni, and S. B. Sinnott, *J. Phys.-Condes. Matter* **14**, 783 (2002).
- 39 Q. Lu, M. Arroyo, and R. Huang, *J. Phys. D-Appl. Phys.* **42**, 6 (2009).
- 40 L. Joly-Pottuz, E. W. Bucholz, N. Matsumoto, S. R. Phillpot, S. B. Sinnott, N. Ohmae, and J. M. Martin, *Tribol. Lett.* **37**, 75.
- 41 S. J. Heo, I. Jang, P. R. Barry, S. R. Phillpot, S. S. Perry, W. G. Sawyer, and S. B. Sinnott, *J. Appl. Phys.* **103**, 6 (2008).
- 42 L. Hanley and S. B. Sinnott, *Surf. Sci.* **500**, 500 (2002).
- 43 I. K. Jang and S. B. Sinnott, *J. Phys. Chem. B* **108**, 18993 (2004).
- 44 Y. T. Su, T. R. Shan, and S. B. Sinnott, *Nucl. Instrum. Methods Phys. Res. Sect. B-Beam Interact. Mater. Atoms* **267**, 2525 (2009).
- 45 J. J. Vegh and D. B. Graves, *Plasma Process. Polym.* **6**, 320 (2009).
- 46 W. D. Hsu, I. Jang, and S. B. Sinnott, *Chem. Mat.* **18**, 914 (2006).
- 47 *Polymer Surfaces and Interfaces: Characterization, Modification and Applications* (VSP BV, AH Zeist, 1997).
- 48 M. P. Allen and D. J. Tildesley, *Computer Simulation of Liquids* (Clarendon Press, Oxford, 1989).

- 49 C. W. Gear, *Math. Comput.* **21**, 146 (1967).
- 50 C. W. Gear, *Numerical initial value problems in ordinary differential equations* (Prentice-Hall automatic computation series, Englewood Cliffs, 1971).
- 51 S. A. Adelman and J. D. Doll, *The Journal of Chemical Physics* **64**, 2375 (1976).
- 52 H. B. Callen and T. A. Welton, *Phys. Rev.* **83**, 34 (1951).
- 53 L. Verlet, *Phys. Rev.* **159**, 98 (1967).
- 54 G. V. Lewis and C. R. A. Catlow, *Journal of Physics C-Solid State Physics* **18**, 1149 (1985).
- 55 J. Tersoff, *Phys. Rev. B* **38**, 9902 (1988).
- 56 G. C. Abell, *Phys. Rev. B* **31**, 6184 (1985).
- 57 J. Tersoff, *Phys. Rev. B* **37**, 6991 (1988).
- 58 J. A. Harrison, C. T. White, R. J. Colton, and D. W. Brenner, *Phys. Rev. B* **46**, 9700 (1992).
- 59 D. W. Brenner, J. A. Harrison, C. T. White, and R. J. Colton, *Thin Solid Films* **206**, 220 (1991).
- 60 O. A. Shenderova, V. V. Zhirnov, and D. W. Brenner, *Crit. Rev. Solid State Mat. Sci.* **27**, 227 (2002).
- 61 K. M. Liew, C. H. Wong, X. Q. He, M. J. Tan, and S. A. Meguid, *Phys. Rev. B* **69**, 8 (2004).
- 62 B. Ni, S. B. Sinnott, P. T. Mikulski, and J. A. Harrison, *Phys. Rev. Lett.* **88**, 4 (2002).
- 63 C. W. Padgett and D. W. Brenner, *Nano Lett.* **4**, 1051 (2004).
- 64 W. D. Hsu, I. Jang, and S. B. Sinnott, *J. Vac. Sci. Technol. A* **25**, 1084 (2007).
- 65 W. D. Hsu, S. Tepavcevic, L. Hanley, and S. B. Sinnott, *J. Phys. Chem. C* **111**, 4199 (2007).
- 66 S. K. Pregler, B. W. Jeong, and S. B. Sinnott, *Compos. Sci. Technol.* **68**, 2049 (2008).
- 67 S. J. Stuart, A. B. Tutein, and J. A. Harrison, *J. Chem. Phys.* **112**, 6472 (2000).

- 68 K. D. Krantzman, Z. Postawa, B. J. Garrison, N. Winograd, S. J. Stuart, and J. A. Harrison, Nucl. Instrum. Methods Phys. Res. Sect. B-Beam Interact. Mater. Atoms **180**, 159 (2001).
- 69 L. Pastewka, P. Pou, R. Perez, P. Gumbsch, and M. Moseler, Phys. Rev. B **78**, 4 (2008).
- 70 M. I. Baskes, J. E. Angelo, and C. L. Bisson, Model. Simul. Mater. Sci. Eng. **2**, 505 (1994).
- 71 J. H. Los, L. M. Ghiringhelli, E. J. Meijer, and A. Fasolino, Phys. Rev. B **72**, 14 (2005).
- 72 P. M. Morse, Physical Review **34**, 57 (1929).
- 73 A. Delcorte, P. Bertrand, and B. J. Garrison, J. Phys. Chem. B **105**, 9474 (2001).
- 74 D. J. Griffiths, *Introduction to Quantum Mechanics* (Prentice-Hall, Inc., Upper Saddle River, 1995).
- 75 C. J. Cramer, *Essentials of Computational Chemistry. Theories and Models* (John Wiley & Sons Ltd, West Sussex, 2004).
- 76 N. W. A. a. N. D. Mermin, *Solid State Physics* (Harcourt College Publishers, New York, 1976).
- 77 C. C. J. Roothaan, Reviews of Modern Physics **23**, 69 (1951).
- 78 D. R. Hartree, Proceedings of the Cambridge Philosophical Society **24**, 111 (1928).
- 79 L. H. Thomas, Proceedings of the Cambridge Philosophical Society **23**, 542 (1927).
- 80 E. Fermi, Rend. Acad. Maz. Lancei **6**, 602 (1927).
- 81 P. Hohenberg and W. Kohn, Phys. Rev. B **136**, B864 (1964).
- 82 W. Kohn and L. J. Sham, Phys. Rev. **140**, 1133 (1965).
- 83 A. D. Becke, Physical Review A **38**, 3098 (1988).
- 84 L. A. Curtiss, K. Raghavachari, G. W. Trucks, and J. A. Pople, J. Chem. Phys. **94**, 7221 (1991).

- 85 L. A. Curtiss, K. Raghavachari, P. C. Redfern, V. Rassolov, and J. A. Pople, J. Chem. Phys. **109**, 7764 (1998).
- 86 B. Ni, K. H. Lee, and S. B. Sinnott, J. Phys.-Condes. Matter **16**, 7261 (2004).
- 87 M. J. Frisch, et al., 2003).
- 88 (The MathWorks Inc., Natick, MA, 2008).
- 89 C. Kumar and A. Nijasure, Resonance **2**, 55 (1997).
- 90 B. Adhikari, D. De, and S. Maiti, Prog. Polym. Sci. **25**, 909 (2000).
- 91 B. Adhikari and S. Majumdar, Prog. Polym. Sci. **29**, 699 (2004).
- 92 U. Lange, N. V. Roznyatouskaya, and V. M. Mirsky, Anal. Chim. Acta **614**, 1 (2008).
- 93 Y. P. Wu, S. B. Fang, Y. Y. Jiang, and R. Holze, J. Power Sources **108**, 245 (2002).
- 94 X. L. Ji, K. T. Lee, and L. F. Nazar, Nat. Mater. **8**, 500 (2009).
- 95 J. Roncali, Chem. Rev. **92**, 711 (1992).
- 96 R. D. McCullough, Adv. Mater. **10**, 93 (1998).
- 97 G. Barbarella, M. Melucci, and G. Sotgiu, Adv. Mater. **17**, 1581 (2005).
- 98 T. Liang, S. R. Phillpot, and S. B. Sinnott, Phys. Rev. B **79**, 14 (2009).
- 99 G. Kresse and J. Furthmüller, Computational Materials Science **6**, 15 (1996).
- 100 G. Kresse and J. Furthmüller, Physical Review B **54**, 11169 (1996).
- 101 G. Kresse and D. Joubert, Physical Review B **59**, 1758 (1999).
- 102 A. D. Becke, Physical Review A **38**, 3098 (1988).
- 103 J. P. Perdew, J. A. Chevary, S. H. Vosko, K. A. Jackson, M. R. Pederson, D. J. Singh, and C. Fiolhais, Phys. Rev. B **46**, 6671 (1992).
- 104 J. P. Perdew, K. Burke, and M. Ernzerhof, Physical Review Letters **77**, 3865 (1996).
- 105 S. Oae, *Organic Chemistry of Sulfur* (Plenum Press, New York, 1977).

- 106 B. Devine, I. Jang, T. Kemper, D. Lee, J. D. Gale, N. Iordanova, and S. B. Sinnott, *J. Phys. Chem. C* **114**, 12535.
- 107 E. Artacho, et al., *Journal of Physics: Condensed Matter* **20**, 064208 (2008).
- 108 A. D. Becke, *J. Chem. Phys.* **98**, 5648 (1993).
- 109 H. L. Schmider and A. D. Becke, *J. Chem. Phys.* **108**, 9624 (1998).
- 110 A. D. Boese and J. M. L. Martin, *J. Chem. Phys.* **121**, 3405 (2004).
- 111 A. G. Baboul, L. A. Curtiss, P. C. Redfern, and K. Raghavachari, *J. Chem. Phys.* **110**, 7650 (1999).
- 112 W. G. Hoover, *Physical Review A* **31**, 1695 (1985).
- 113 S. Nose, *J. Chem. Phys.* **81**, 511 (1984).
- 114 S. Nose, *Molecular Physics* **52**, 255 (1984).
- 115 G. W. T. M. J. Frisch, H. B. Schlegel, G. E. Scuseria, M. A. Robb, J. R. Cheeseman, J. A. Montgomery, Jr., T. Vreven, K. N. Kudin, J. C. Burant, J. M. Millam, S. S. Iyengar, J. Tomasi, V. Barone, B. Mennucci, M. Cossi, G. Scalmani, N. Rega, G. A. Petersson, H. Nakatsuji, M. Hada, M. Ehara, K. Toyota, R. Fukuda, J. Hasegawa, M. Ishida, T. Nakajima, Y. Honda, O. Kitao, H. Nakai, M. Klene, X. Li, J. E. Knox, H. P. Hratchian, J. B. Cross, V. Bakken, C. Adamo, J. Jaramillo, R. Gomperts, R. E. Stratmann, O. Yazyev, A. J. Austin, R. Cammi, C. Pomelli, J. W. Ochterski, P. Y. Ayala, K. Morokuma, G. A. Voth, P. Salvador, J. J. Dannenberg, V. G. Zakrzewski, S. Dapprich, A. D. Daniels, M. C. Strain, O. Farkas, D. K. Malick, A. D. Rabuck, K. Raghavachari, J. B. Foresman, J. V. Ortiz, Q. Cui, A. G. Baboul, S. Clifford, J. Cioslowski, B. B. Stefanov, G. Liu, A. Liashenko, P. Piskorz, I. Komaromi, R. L. Martin, D. J. Fox, T. Keith, M. A. Al-Laham, C. Y. Peng, A. Nanayakkara, M. Challacombe, P. M. W. Gill, B. Johnson, W. Chen, M. W. Wong, C. Gonzalez, and J. A. Pople,, (Gaussian, Inc., Wallingford CT., 2004).
- 116 R. C. Brown, C. J. Cramer, and J. T. Roberts, *J. Phys. Chem. B* **101**, 9574 (1997).
- 117 C. Y. Peng and H. B. Schlegel, *Isr. J. Chem.* **33**, 449 (1993).
- 118 Ditchfie.R, W. J. Hehre, and J. A. Pople, *J. Chem. Phys.* **54**, 724 (1971).
- 119 K. Fukui, *Accounts Chem. Res.* **14**, 363 (1981).

- 120 J. Čížek, *On the Use of the Cluster Expansion and the Technique of Diagrams in Calculations of Correlation Effects in Atoms and Molecules* (John Wiley & Sons, Inc., New York, 19629).
- 121 G. D. Purvis and R. J. Bartlett, *J. Chem. Phys.* **76**, 1910 (1982).
- 122 M. Morton, J. Barron, T. Kemper, S. Sinnott, and N. Iordanova, *J. Phys. Chem. A* **115**, 4976.
- 123 H. Spanggaard and F. C. Krebs, *Sol. Energy Mater. Sol. Cells* **83**, 125 (2004).
- 124 A. R. Murphy and J. M. J. Frechet, *Chem. Rev.* **107**, 1066 (2007).
- 125 C. D. Dimitrakopoulos and P. R. L. Malenfant, *Adv. Mater.* **14**, 99 (2002).
- 126 I. F. Perepichka, D. F. Perepichka, H. Meng, and F. Wudl, *Adv. Mater.* **17**, 2281 (2005).
- 127 S. R. Forrest, *Nature* **428**, 911 (2004).
- 128 D. Fichou and C. Ziegler, in *Handbook of Oligo- and Polythiophenes* (Wiley-VCH Verlag GmbH, 2007), p. 183.
- 129 A. Podesta, T. Toccoli, P. Milani, A. Boschetti, and S. Innotta, *Surf. Sci.* **464**, L673 (2000).
- 130 L. G. Paterno, S. Manolache, and F. Denes, *Synth. Met.* **130**, 85 (2002).
- 131 L. M. H. Groenewoud, G. H. M. Engbers, J. G. A. Terlingen, H. Wormeester, and J. Feijen, *Langmuir* **16**, 6278 (2000).
- 132 L. M. H. Groenewoud, G. H. M. Engbers, and J. Feijen, *Langmuir* **19**, 1368 (2003).
- 133 D. L. Irving, B. D. Devine, and S. B. Sinnott, *J. Lumines.* **126**, 278 (2007).
- 134 S. Tepavcevic, University of Illinois at Chicago, 2006.
- 135 F. Vanbolhuis, H. Wynberg, E. E. Havinga, E. W. Meijer, and E. G. J. Staring, *Synth. Met.* **30**, 381 (1989).
- 136 F. Garnier, A. Yassar, R. Hajlaoui, G. Horowitz, F. Deloffre, B. Servet, S. Ries, and P. Alnot, *J. Am. Chem. Soc.* **115**, 8716 (1993).
- 137 M. Haran, J. E. Goose, N. P. Clote, and P. Clancy, *Langmuir* **23**, 4897 (2007).

- 138 R. d'Agostino, P. Favia, C. Oehr, and M. R. Wertheimer, *Plasma processes and polymers* (WILEY-VCH Verlag GmbH & Co. KGaA, Freiburg, 2005).
- 139 T. Vrlinic, C. Mille, D. Debarnot, and F. Poncin-Epaillard, *Vacuum* **83**, 792 (2009).
- 140 D.-X. Liu, M.-Z. Rong, X.-H. Wang, F. Iza, M. G. Kong, and P. Bruggeman, *Plasma Process. Polym.* **7**, 846.
- 141 E. Stoffels, Y. Sakiyama, and D. B. Graves, *Plasma Science, IEEE Transactions on* **36**, 1441 (2008).
- 142 F. D. Egitto and L. J. Matienzo, *IBM J. Res. Dev.* **38**, 423 (1994).
- 143 P. Favia, G. Cicala, A. Milella, F. Palumbo, R. Rossini, and R. d'Agostino, *Surf. Coat. Technol.* **169**, 609 (2003).
- 144 K. Kremer and G. S. Grest, *J. Chem. Phys.* **92**, 5057 (1990).
- 145 S. Plimpton, *J. Comput. Phys.* **117**, 1 (1995).
- 146 E. L. T. Samuel M. Allen, *the Structure of Materials* (John Wiley & Sons, Inc., New York, 1999).
- 147 J. Brandrup, E. H. Immergut, E. A. Grulke, A. Abe, and D. R. Bloch, (John Wiley & Sons).
- 148 G. Suchaneck, M. Guenther, G. Gerlach, K. Sahre, K. J. Eichhorn, B. Wolf, A. Deyneka, and L. Jastrabik, *Ion-Induced Chemical and Structural Modification of Polymer Surfaces* (Wiley-VCH Verlag GmbH & Co. KGaA, 2005).
- 149 G. W. Fox, *Phys. Rev.* **37**, 815 (1931).
- 150 L. Tonks and I. Langmuir, *Phys. Rev.* **33**, 195 (1929).
- 151 A. Vogelsang, A. Ohl, H. Steffen, R. Foest, K. Schroder, and K. D. Weltmann, *Plasma Process. Polym.* **7**, 16.
- 152 J. Zekonyte, J. Erichsen, V. Zaporojtchenko, and F. Faupel, *Surf. Sci.* **532**, 1040 (2003).
- 153 K. Kurihara, A. Egami, and M. Nakamura, *J. Appl. Phys.* **98**, 5 (2005).
- 154 J. J. Vegh, et al., *J. Appl. Phys.* **104**, 9 (2008).
- 155 J. A. G. Baggerman, R. J. Visser, and E. J. H. Collart, *J. Appl. Phys.* **75**, 758 (1994).

- 156 C. Hopf, M. Schluter, T. Schwarz-Selinger, U. von Toussaint, and W. Jacob, *New J. Phys.* **10**, 27 (2008).
- 157 T. H. Lin, M. Belser, and Y. H. Tzeng, *IEEE Trans. Plasma Sci.* **16**, 631 (1988).
- 158 J. Friedrich, G. Kühn, and R. Mix, in *Plasma Process. Polym.* (Wiley-VCH Verlag GmbH & Co. KGaA, 2005), p. 1.
- 159 N. Medard, J. C. Soutif, and F. Poncin-Epaillard, *Langmuir* **18**, 2246 (2002).
- 160 D. Ellerweg, J. Benedikt, A. von Keudell, N. Knake, and V. Schulz-von der Gathen, *New J. Phys.* **12**, 12.
- 161 E. J. H. Collart, J. A. G. Baggerman, and R. J. Visser, *J. Appl. Phys.* **78**, 47 (1995).
- 162 A. G. Shard and J. P. S. Badyal, *Macromolecules* **25**, 2053 (1992).
- 163 G. Timp, et al., in *Electron Devices Meeting, 1999. IEDM Technical Digest. International*, 1999), p. 55.
- 164 J. Robertson, *Reports on Progress in Physics*, 327 (2006).
- 165 G. D. Wilk, R. M. Wallace, and J. M. Anthony, *J. Appl. Phys.* **89**, 5243 (2001).
- 166 J. Wang, H. P. Li, and R. Stevens, *J. Mater. Sci.* **27**, 5397 (1992).
- 167 H. J. Monkhorst and J. D. Pack, *Physical Review B* **13**, 5188 (1976).
- 168 J. D. Gale, *J. Chem. Soc.-Faraday Trans.* **93**, 629 (1997).
- 169 R. HILL, *Proc. Phys. Soc. London* **65**, 350 (1951).
- 170 C. A. Ponce, R. A. Casali, and M. A. Caravaca, *Journal of Physics-Condensed Matter* **20** (2008).
- 171 A. F. Kohan, G. Ceder, D. Morgan, and C. G. Van de Walle, *Physical Review B* **61**, 15019 (2000).

BIOGRAPHICAL SKETCH

Travis Kemper was born in California in 1981. He attended UCSC from 2000 to 2004, and received a Bachelor of Science in applied physics. From 2005 to 2006 he worked as a Junior Specialist for Dr. Ali Shakouri in the Electrical Engineering Department at UCSC. After this, he traveled the world for one year before starting a PhD program in the Materials Science and Engineering Department at the University of Florida in 2007. He received a Master of Science in 2010 and his PhD in 2011.